LAKEHEAD UNIVERSITY

Simultaneous Vibration Suppression and Energy Harvesting with a Non-traditional Vibration Absorber

By

Miao Yuan

A THESIS

SUBMITTED TO THE FAULTY OF GRADUATE STUDIES

IN PARTIAL FULFILMENT OF THE REQUIREMENT FOR THE

DEGREE OF MASTER OF SCIENCE

MECHANICAL ENGINEERING

THUNDER BAY, ONTARIO

August 2017

ABSTRACT

The dynamic vibration absorber, or tuned mass damper, has been one of the most commonly used passive vibration control devices over the past hundred years. With an optimally designed vibration absorber, significant vibration suppression can be achieved to maintain structure health and integrity. On the other hand, researchers are seeking effective energy harvesting techniques to harvest energy from ambient vibration for purposes such as powering sensor networks and microsystems. This has brought light to the investigation of simultaneous vibration suppression and energy harvesting. This research is thus motivated to develop an apparatus with a non-traditional vibration absorber in order to achieve vibration control and energy harvesting simultaneously.

For a traditional vibration absorber installed to a single-degree-of-freedom primary system, the absorber damper is connected between the primary mass and the absorber mass. The tuning strategies of such a traditional absorber have been thoroughly studied and energy harvesting techniques have also been applied to the combined system. This research studies a non-traditional vibration absorber whose absorber damper is connected directly between the absorber mass and the base. An apparatus is developed in which an electromagnetic damper used as both the absorber damper and energy harvester is placed between the absorber mass and the base. The principle of the electromagnetic damping is discussed, and the optimum parameters of the non-traditional vibration absorber are studied with respect to different performance indexes under various types of excitation. Analytical derivation, numerical simulation and experiment results are presented in the investigation of each of the tuning strategies. The study has indicated that despite the inevitable trade-off between vibration suppression and energy harvesting, the proposed apparatus is capable of achieving the dual goal with a satisfying performance.

ACKNOWLEDGMENTS

First, I would like to express my sincere gratitude to my supervisor Dr. Kefu Liu and co-supervior Dr. Ayan Sadhu who have provided me with valuable guidance during the course of this research. Their academic passion and rigorousness have always been an inspiration to me. They have supported me in all aspects including thesis research and writing, career suggestion and my life in general.

I would also like to thank all my fellow graduate students: John(Yu) Zhang, Xiaolin Li, Peter Friesen, Ahmad Khanjer, and undergraduate students: Denis Betancourt, Alex Kunji, and Gaganpreet Sall, for their assistance in machining and experiment.

I would also like to thank my parents: Bingyun Yuan and Wenhui Li and all my friends for their love, care, and patience throughout my life.

Table of Contents

List of Figures

List of Tables

Chapter 1 Introduction

The motivation of this research is to investigate the behaviour of a non-traditional vibration absorber coupled with an electromagnetic damper which is used to achieve simultaneous vibration suppression and energy harvesting. This chapter provides an extensive literature review on vibration absorbers, energy harvesting techniques, as well as the topic of simultaneous vibration control and energy harvesting, which leads to the motivation and novelty of this work.

1.1 Literature review

1.1.1 Dynamic vibration absorber/tuned mass damper

Machines or structures in real life are often subjected to vibrations, e.g. rotary machines with unbalanced mass, high-rise buildings under wind excitation and earthquakes. Vibrations are usually undesired because they can induce noises, discomfort for riding experiences, and even damage to structural components which may lead to disastrous result. Researchers and engineers have dedicated enormous researches and investigations to the elimination of unwanted vibration with various techniques and devices. The damped vibration absorber (DVA), or tuned mass damper (TMD), is one of the commonly-used passive control devices for structural vibration suppression. Figure 1.1 (a) shows the model of the traditional vibration absorber. The primary system to be controlled is simplified as a single-degree-of-freedom (SDOF) system. By attaching a mass-spring-damper system to the SDOF primary structure, the vibration of the primary system can be significantly reduced over a wide frequency band. This has been widely applied to fields like mechanical engineering and civil engineering. For example, the TMD installed in the Taipei 101 building has been successfully serving its purpose of vibration mitigation to protect the building from typhoons and earthquakes since 2004.

The key aspects of designing a TMD are associated with the determination of two important variables: a) the frequency tuning ratio (β), which is related to the absorber stiffness (k_a) and defined as the ratio of the natural frequency of the TMD to that of the primary structure; and b) the damping ratio (ζ), which is related to the absorber damping coefficient (c_a) and can be defined as the ratio of the absorber damping coefficient to either the critical damping coefficient for the TMD or the product of critical damping coefficient and the reciprocal of the frequency tuning ratio. Various researches have been conducted to find the optimum values of these parameters. The first analytical theory, known as the classical "fixed-points" theory, was proposed by Hartog (1940) to tackle the optimum solution of a damped TMD attached to an undamped primary system. Based on the optimality he proposed, he found the optimum frequency tuning ratio while failing to obtain the optimum damping ratio. In continuation of this work, Brock (1946) derived the analytical expression of the optimum damping ratio for both optimum as well as constant tuning. This research was then extended to various excitation conditions (Warburton, 1982). The transient responses of the system have also been studied with derived optimum parameters (Yamaguchi, 1988). While the above work investigated an undamped primary system, the inherent damping of the primary system was later also taken into consideration, requiring computationally intensive numerical optimization (Rana & Song, 1998).

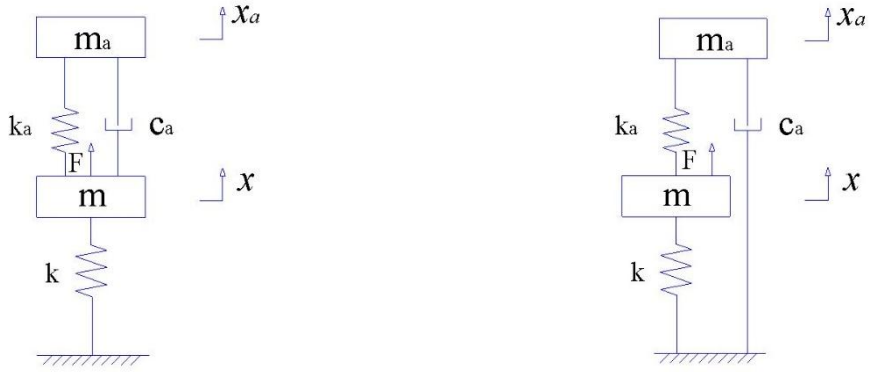

(a) Model A (b) Model B

Figure 1.1 Two configurations of TMD.

The above mentioned works are dedicated to the examination of the traditional TMD shown in Figure 1.1 (a), often referred as “model A”. The formulae for optimum parameters are listed in Table 1.1. As the damper is connected between the primary mass and the absorber mass, this can be challenging when the damper requires a certain stroke space and there is limited space for TMD. Figure 1.1 (b) shows a variant design of TMD, also known as “model B”, where the damper is connected between the absorber mass and the ground directly. For an undamped primary structure attached with a model B TMD and subjected to a harmonic force excitation, the optimum parameters of the model defined in absolute displacement coordinates were derived using the classical “fixed-points” theory by Ren (2001). The results were verified by K. Liu and Liu (2005) later using a slightly different approach. Their results show that model B can achieve greater vibration reduction for the primary system than model A. The optimum parameters of model B were also found by minimize the normalized velocity magnitude by Chueng and Wong (2009).

Despite the demonstrated effectiveness using the “fixed-points” theory, it has been found that the non-traditional TMD following the classical design methodology does not lead to the global minimum resonant amplitude for an SDOF system under harmonic force excitation (Chueng &

Wong, 2011a; Xiang & Nishitani, 2014). Chueng and Wong (2011a) derived the H_∞ optimum parameters of the non-traditional TMD for an SDOF system which resulted in lower maximum amplitude response than the previously found results. The same authors (2011b) also derived the H_2 optimum parameters to minimize the total vibration energy of an SDOF system under random excitation and made a comparison with the traditional TMD. Xiang and Nishitani (2014) proposed a different optimum design method from the standpoint of obtaining a wider suppression bandwidth. When the damping of the primary structure is considered, different methods are required to find the optimum tuning parameters. K. Liu and Coppola (2010) presented an approximate closed-form solution for the optimum tuning parameters that was validated using two different numerical methods: the Chebyshev's equi-oscillation theorem (Pennestri, 1998) and sequential simplex method (Belegundu & Chandrupatla, 1999). Anh and Nguyen (2014) proposed a dual equivalent linearization technique to derive the approximate analytical solutions for the H_∞ optimum parameters for this variant TMD attached to a damped structure subjected to force excitation.

For model B attached to an undamped primary system under a harmonic ground excitation, Wong and Chueng (2008) investigated the optimum parameters using the "fixed-points" theory, with the performance index defined as the maximum magnitude of the frequency response function (FRF) that is the ratio of the primary structure's absolute displacement to the ground displacement. Xiang and Nishitani (2015) used the displacement coordinates relative to the ground motion to define the model. In their work, the FRF was defined as the ratio of the relative displacement magnitude of the primary mass to the relative static deflection of the primary spring due to the inertia force. Using the maximum magnitude of the FRF as the performance index, the optimum parameters were derived. In addition, Xiang and Nishitani (2015) also adopted the stability maximization criterion (SMC) to allow the free vibration of the primary

structure to decay optimally and demonstrated the effectiveness of the SMC-based TMD both numerically and experimentally.

Table 1.1. Optimum parameters for model A

	Authors	Performance Index	β_{opt}	ζ_{opt}
Undamped	Hartog (1940) Brock (1946)	$\lvert X_{1-abs} / X_{1-st} \rvert$ in harmonic force excitation	$\frac{1}{\sqrt{1+\mu}}$	$\sqrt{\frac{3\mu}{8(1+\mu)}}$
	Warburton (1982)	$\lvert X_{1-abs} / X_{1-st} \rvert$ in harmonic base excitation	$\frac{1}{\sqrt{1+\mu}}\sqrt{\frac{2-\mu}{2}}$	$\sqrt{\frac{3\mu}{4(1+\mu)(2-\mu)}}$
	Warburton (1982)	$E[X_1^2]/(S_f\omega_1/k_1^2)$ in random force excitation	$\frac{1}{\sqrt{1+\mu}}\sqrt{\frac{2+\mu}{2}}$	$\sqrt{\frac{\mu(4+3\mu)}{8(1+\mu)(2+\mu)}}$
	Warburton (1982)	$E[X_1^2]/(2\pi S_f\omega_1/k_1^2)$ in random force excitation	$\frac{\sqrt{\mu}}{2}$	$\frac{1}{\sqrt{1+\mu}}$
	Yamaguchi (1988)	$-\max_i(\mathrm{Re}[\lambda_i])$ in transient vibration	$\frac{1}{1+\mu}$	$\sqrt{\frac{\mu}{1+\mu}}$
Damped	Rana and Song (1998)	Numerical optimization required		

Table 1.2. Optimum parameters for model B.

	Authors	Performance Index	β_{opt}	ζ_{opt}
Undamped	Ren (2001)	$\lvert X_{1-abs} / X_{1-st} \rvert$ in harmonic force excitation	$\frac{1}{\sqrt{1-\mu}}$	$\sqrt{\frac{3\mu}{4(2-\mu)}}$
	K. Liu and Liu (2005)	$\lvert X_{1-abs} / X_{1-st} \rvert$ in harmonic force excitation	$\frac{1}{\sqrt{1-\mu}}$	$\sqrt{\frac{3\mu}{4(1-\mu)(2-\mu)}}$
	Chueng and Wong (2009)	$\lvert V_{1-abs} / V_{1-st} \rvert$ in harmonic force excitation	$\sqrt{\frac{1-\sqrt{1-2\mu}}{\mu\sqrt{1-2\mu}}}$	$\sqrt{\frac{A\sqrt{1-2\mu}+B}{8\mu^2\sqrt{1-2\mu}(-7\mu^2-2\mu+4+(3\mu^2-2\mu-4)\sqrt{1-2\mu})}}$ $A=16-48\mu-12\mu^2+84\mu^3+3\mu^4-15\mu^5$ $A=-16+64\mu-28\mu^2-112\mu^3+61\mu^4+38\mu^5$
	Wong and Chueng (2008)	$\lvert V_{1-abs} / V_{1-st} \rvert$ in harmonic base excitation	$\frac{1}{\sqrt{1-\mu}}$	$\sqrt{\frac{\mu(3-\mu)}{8}}$
	Chueng and Wong (2011b)	$E[\lvert X_{1-abs} / X_{1-st} \rvert^2]$ in random force excitation	Value as large as possible	$\sqrt{\frac{\beta^4+(2-\mu)\beta^2+1}{4\beta^2}}$
	Xiang and Nishitani (2015)	$-\max_i(\mathrm{Re}[\lambda_i])$ in transient vibration	$\frac{1-\sqrt{1-4\mu}}{2\mu}$	$\sqrt{\frac{1-\sqrt{1-4\mu}}{2}}$
Damped	K. Liu and Coppola (2010)	$\lvert X_{1-abs} / X_{1-st} \rvert$ in harmonic force excitation	$\sqrt{\frac{1-4\zeta_p^2}{1-\mu}}$	Closed-form solution not available
	Anh and Nguyen (2014)	$\lvert X_{1-abs} / X_{1-st} \rvert$ in harmonic force excitation	$\frac{1}{\sqrt{1-\mu}\left(\sqrt{1+\frac{\pi^2}{(\pi^2-2)^2}\zeta_p^2}+\frac{\pi}{\pi^2-2}\zeta_p\right)}$	Closed-form solution not available
Undamped or damped	Xiang and Nishitani (2014)	Suppression bandwidths in harmonic base excitation	$\frac{1}{\sqrt{\mu}}$	Closed-form solution not available

1.1.2 Simultaneous vibration suppression and energy harvesting

The idea of energy harvesting using ambient vibration has been vastly explored with a significant impact on the development of wireless sensor networks (Lynch & Loh, 2006), low-power actuators (Paradiso & Starner, 2005), microsystems (Beeby, Tudor, & White, 2006), etc. One of the most commonly used vibration-based energy harvesting techniques is the piezoelectricity. Studies on the fundamental properties and modelling of piezoelectric material are presented in several literatures (Feenstra, Granstrom, & Sodano, 2008; Ng & Liao, 2005; Shahruz, 2008; Sodano, Park, & Inman, 2004; Stephen, 2006). A significant amount of researches has been also dedicated to the performance of piezoelectric devices under different external excitations and the optimization of the harvested power with respect to electro-mechanical components of the device as well as the control strategy (Chtiba, Choura, Nayfeh, & El-Borigu, 2010; Sodano, Inman, & Park, 2005; Stephen, 2006; Yoon, 2008). Similarly, a great amount of research has been conducted for another popular harvesting method of using electromagnetic devices (Beeby, Torah, & Tudor, 2007; Cepnik, Radler, Rosenbaum, Strohla, & Wallrabe, 2011; Deng & Wang, 2010; Elvina & Elvinb, 2011; Harne, 2012; Kremer & Liu, 2014; Mann & Sims, 2010; Masoumi & Wang, 2016; Shen, Zhu, & Xu, 2012; Sneller & Mann, 2010). For both the above energy harvesting approaches, they are commonly implemented as mass-spring-damper devices. Considering the interaction between the energy harvesting unit and the primary structure, researchers have been developing devices capable of both attenuating the structural vibration while converting the absorbed energy into electrical power (Tang & Zuo, 2012a, 2012b; Wang & Inman, 2012; Zuo & Cui, 2013).

The idea of simultaneous vibration suppression and energy harvesting has promising applications in many engineering fields. For example, piezoelectric materials can be used to form composite sandwich structures for the purpose of self-controlling and self-powering unmanned aerial vehicles (Wang & Inman, 2013). Researchers have explored inerter-based vibration suppression

devices that harvest energy using electro-magnetic tuned inerter damper (Gonzalez-Buelga, Clare, Neild, Jiang, & Inman, 2015a). Tuned mass damper is another widely investigated device where researchers combine its ability for vibration control with energy harvesting by introducing piezoelectricity or electro-magnetic coupling (Gonzalez-Buelga et al., 2014; Gonzalez-Buelga, Clare, Neild, Burrow, & Inman, 2015b; Y. Liu, Chi-Chang, Jason, & Zuo, 2016). Studies on energy harvesting-enabled tuned mass damper inerter (TMDI) can also be found in literature where both a TMD and an inerter are employed (Salvi & Giaralis, 2016). It should be noted that all the aforementioned configurations employed model A. Gonzalez-Buelga et al. (2014) investigated an optimized tuned mass damper/harvester device where the energy-dissipating damper of the TMD is replaced with an electro-magnetic device to transform mechanical vibration into electrical energy. The absorber system is attached to the primary structure with the absorber damper connected between the primary mass and the absorber mass, which is the model A configuration. The paper considered both direct excitation and base excitation and the results for using both adaptive and semi-active control laws were presented.

1.2 Objectives and contributions

From the previous literature review, it is noted that there has not been any report on simultaneous vibration suppression and energy harvesting based on the model B TMD. This study is motivated to address this need. An apparatus of the model B TMD is first developed which consists of a primary structure subjected to base excitation and a tunable vibration absorber. The tunable vibration absorber is composed of a cantilever beam and an electromagnetic device. Two magnets are used as the absorber mass and subjected to the effect of the electromagnetic device which serves as both the damper and the energy harvester. The vibration absorber is tunable in such a way that the frequency tuning is achieved by adjusting the length of the cantilever beam and the damping tuning is obtained by varying the load resistance of the energy harvesting

circuit. This allows for the achievement of different tuning conditions and thus the effectiveness of different tuning strategies can be validated experimentally.

The objectives of this study are as follows: (1) to develop a tunable model B TMD; (2) to study, design and build an electromagnetic device used as the absorber damper and energy harvester; (3) to investigate different tuning strategies of the developed model B TMD, and (4) to explore the ability of simultaneous vibration suppression and energy harvesting with the developed apparatus. One manuscript that is based on Chapter 2 and 3 has been submitted to Journal of Intelligent Material Systems and Structures and another manuscript that is based on Chapter 7 has been submitted to Journal of Vibration and Control.

1.3 Thesis outline

In the following chapter, the developed apparatus will be introduced and the principles of the electromagnetic device will be explained. With these backgrounds, the remainder of this thesis investigates the model B TMD installed to a SDOF system in three different perspectives, in Chapter 3, 4 and 5 respectively, where the optimum tuning condition will be explored with regard to vibration suppression and energy harvesting. Chapter 6 introduces a situation when the non-traditional absorber is employed in a multi-degree-of-freedom (MDOF) system and provides some discussion which intrigues thoughts for future work. In Chapter 7, a discussion on the condition assessment of a vibration absorber is also provided. At the end, the conclusions are drawn to summarize the work.

Chapter 2 Apparatus and Modelling

In this chapter, the developed apparatus of a model B TMD is introduced, followed by the explanation of the principles of the employed electromagnetic device. This lays a foundation for the remaining investigation of this thesis.

2.1 Developed apparatus

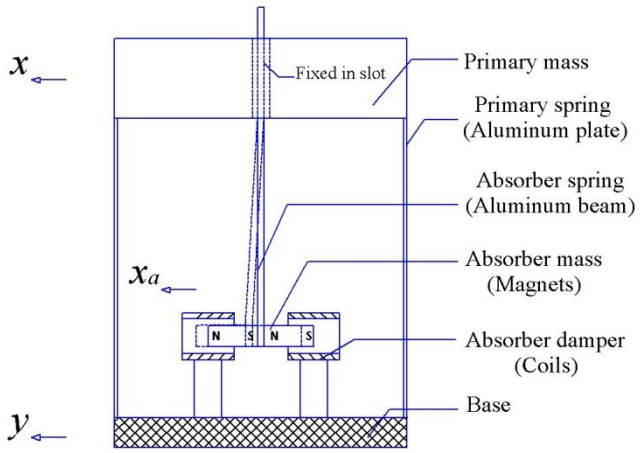

(a)

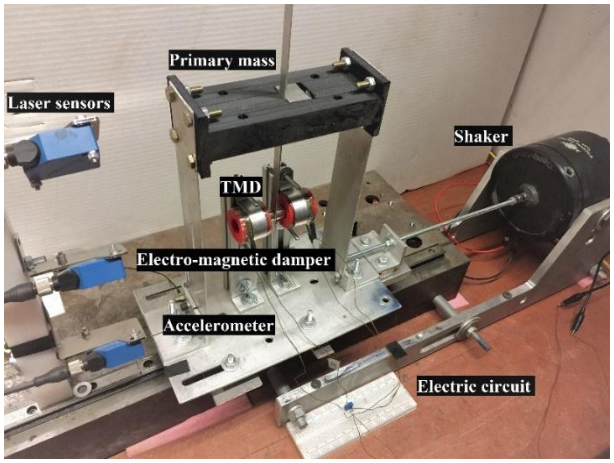

(b)

Figure 2.1. (a) Schematic of the developed apparatus; (b) photo of the experiment set-up.

The apparatus developed for this work is shown in Figure 2.1. On the top is the schematic of the system while the bottom figure is a photo of the experiment set-up. The primary system consists of an Acrylonitrile Butadiene Styrene (ABS) filament platform supported by two aluminum plates. The lower ends of the plates are clamped to a base that is fastened to a slipping table. The TMD consists of an aluminum cantilever beam and two permanent magnets. One end of the beam is clamped in a slot built in the primary mass platform. The beam's length can be adjusted by sliding it in the slot. The two magnets are attached at the free end of the beam by their attracting magnetic force. The properties of the beam and the magnets can be found in Table 2.1. A pair of coils are fastened directly to the base. The magnets are situated inside the coils such that they form two electromagnetic dampers. An electric circuit is formed by connecting the coils in series with a variable resistor that serves as a load. Comparing Figure 2.1 (a) with Figure 1.1 (b), it can be seen that the developed apparatus represents a model B TMD: the absorber mass is subjected to the force from the absorber spring which connects the absorber mass to the primary mass, and the force from the absorber damper (coils) which is fixed to the base.

Table 2.1. Parameters of the absorber system.

Aluminum beam		Oscillating magnet ×2	
Width (mm)	11.12	Length (mm)	25.4
Thickness (mm)	1.5	Diameter (mm)	12.7
Length range (mm)	100-150	Material Type	NdFeB (N40)
		Mass (kg)	0.024×2

Figure 2.1 (b) is a photo of the experiment set-up. The base is driven by a B&K type 2809 shaker through a stinger. The shaker is driven by a B&K type 2718 power amplifier whose current can be monitored. An accelerometer is attached to the base to monitor the base acceleration. Three Wenglor CP24MHT80 reflex lasers (RF) are used to measure the displacements of the primary mass, absorber mass, and the base, respectively. Figure 2.2 is a schematic of the experimental

system. The computer used in this study is equipped with a dSPACE dS1104 data acquisition board that collects all the sensor signals and outputs the excitation signal to the power amplifier. A Simulink model is developed and connected to the dSPACE Control Desktop software to control the experiment.

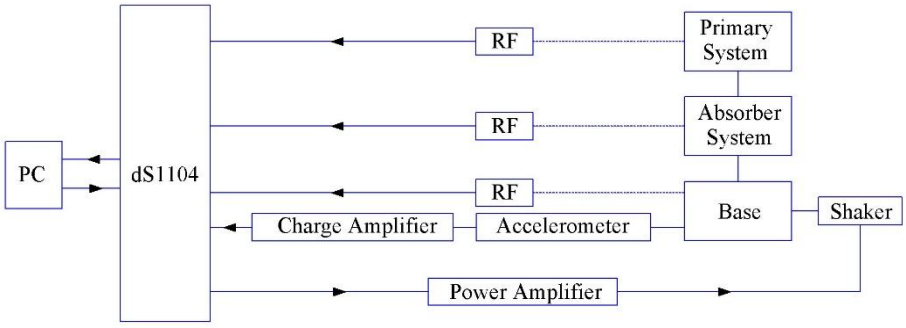

Figure 2.2. Schematic of the experiment system.

This research is focused on studying this developed apparatus both analytically and experimentally. Before mathematic models of the apparatus are introduced, the principles of the electromagnetic dampers are to be discussed.

2.2 Electromagnetic damper

2.2.1 System modelling

In order to investigate different tuning strategies for the model B TMD, it would require the absorber system to be tunable both on the frequency tuning ratio (absorber stiffness) and the damping ratio (absorber damping coefficient).The proposed apparatus allows to adjust the absorber stiffness by varying the beam length, and the electromagnetic damper employed in this study offers a convenient way to adjust the damping level by varying the load resistance.

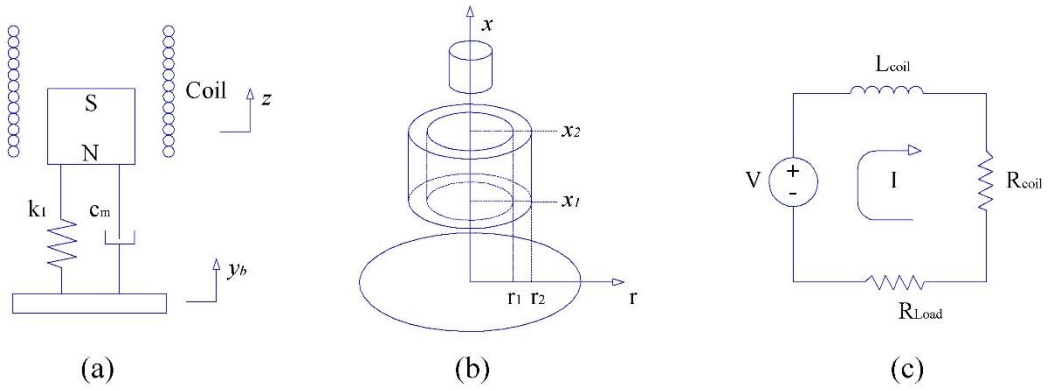

Figure 2.3. Modelling of the electromagnetic damper: (a) equivalent SDOF system; (b) coil and oscillating magnet diagram; (c) electric circuit diagram.

To study the principles of the electromagnetic damper, the system is first considered as an SDOF structure with the magnet oscillating in the coil as shown in Figure 2.3 (a). The equation of motion is given as,

$$m_1\ddot{z} + c_m\dot{z} + k_1 z + F_e = -m_1\ddot{y}_b \tag{2.1}$$

where y_b is the base motion, z is the displacement relative to the base, m_1 is the mass of the magnet, c_m is the mechanical damping coefficient, k_1 is the stiffness of the spring, F_e is the electro-magnetic force induced by the interaction of the moving magnet and the coil.

When the magnet is oscillating along the coil's axis, Faraday's law of induction predicts that an electric potential will be generated across the coil's lead. For a single loop coil, the so-called electromotive force (EMF) is given by,

$$V_s = \oint_{loop} (\boldsymbol{v} \times \boldsymbol{B}) \bullet d\boldsymbol{L} \tag{2.2}$$

where $d\boldsymbol{L}$ is the differential length of the loop, $\boldsymbol{v}$ is the velocity of the magnet and $\boldsymbol{B}$ represents the magnetic flux density generated by the magnet. The above equation can be expanded by expressing the vectors in terms of components,

$$V_s = \oint_{loop} (-\dot{z}\boldsymbol{e}_a) \times (B_a(y,r)\boldsymbol{e}_a + B_r(y,r)\boldsymbol{e}_r) \bullet dl\boldsymbol{e}_l \tag{2.3}$$

where $\boldsymbol{e}_a$ is the unit axial vector, $\boldsymbol{e}_r$ is the unit radial vector, $\boldsymbol{e}_l = \frac{d\boldsymbol{L}}{dl}$ is the unit vector pointing along the tangential direction of the wire, $B_a(y,r)$ is the axial magnetic flux density and $B_r(y,r)$ is the radial magnetic flux density in which *y* is the axial distance between the center of the magnet and the loop and *r* represents the radial coordinate. After performing vector operations, Eq. (2.3) is reduced to,

$$V_s = -\dot{z}\oint_{loop} B_r(y,r)dl = \Theta_s \dot{z} \tag{2.4}$$

where $\Theta_s = -\oint_{loop} B_r(y,r)dl$ is defined as the transduction factor for a single loop coil.

Now consider a magnet moving along the coil axis as shown in Figure 2.4. r_{mag} is the radius of the magnet, l_{mag} is the length of the one magnet, A_{coil} is the cross-sectional area of the coil, h_{coil} is the height of the coil and $r_{1,2}$ is the inner/outer radius of the coil. The total transduction factor for one coil located at a distance *S* is given by,

$$\Theta_{coil}(S) = -\frac{l_{wire}}{A_{coil}} \int_{r_1}^{r_2} \int_{y_1}^{y_2} B_r(y,r)dydr \tag{2.5}$$

where,

$$y_1 = S - \frac{h_{coil}}{2}, y_2 = S + \frac{h_{coil}}{2} \tag{2.6}$$

l_{wire} is the total length of the wire of the coil. The total transduction factor for two identical coils connected in series is $\Theta(S) = 2\Theta_{coil}(S)$.

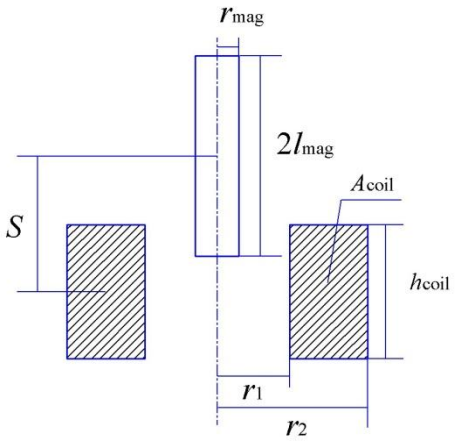

Figure 2.4. Magnet moving in a coil.

A closed circuit is formed by connecting a load resistor to the coils as shown in Figure 2.3 (c). Applying Kirchhoff's law to the circuit yields

$$2L_{coil}\frac{di}{dt}+(2R_{coil}+R_{load})i=\Theta\dot{z} \tag{2.7}$$

where L_{coil} and R_{coil} are the inductance and resistance of one coil, respectively, i is the induced current and R_{load} is the load resistance. For the coils used in this study, the inductance of the coil is found to be $2L_{coil}=2.0\ \text{mH}$ through measurement. With a maximum driving frequency of 20 Hz, the maximum reactance due to the inductance is $Z=2\pi(2\times 20)=251.33\ \text{m}\Omega$ which accounts for approximately 5% of the total resistance in the coils. Thus, the coil inductance is neglected in this study to avoid unnecessary analytical complexity. Eq. (2.7) now yields,

$$i=\frac{\Theta}{2R_{coil}+R_{load}}\dot{z} \tag{2.8}$$

Comparing Eq. (2.1), the electro-magnetic (Lorentz) force F_e induced by the current has the form (Elvina & Elvinb, 2011) $F_e=\Theta i$ which yields,

$$F_e = \frac{\Theta^2}{2R_{coil} + R_{load}} \dot{z} \tag{2.9}$$

The electrical damping coefficient is defined as:

$$c_e = \frac{\Theta^2}{2R_{coil} + R_{load}} \tag{2.10}$$

Eq. (2.10) shows that the electrical damping coefficient decreases with increase of the load resistance and is proportional to the squared value of the transduction factor.

Table 2.2. Parameters of the coils.

Coil ×2			
Inner radius r_1 (mm)	12.175	Turns N	320
Outer radius r_2 (mm)	18.525	Wire length l_{wire} (m)	29.8
Height h_{coil} (mm)	31.75	Resistance R_{coil} (Ω)	2.4

The properties of the coils are listed in Table 2.2. Following the method used by Kremer and Liu (2014), a finite element analysis software Finite Element Method Magnetics (FEMM) is used to calculate the magnetic flux density of the magnet. Using an axisymmetric model, the radial flux density is found and shown in Figure 2.5 (a). As shown, the radial flux density reaches the maximum magnitude at the ends of the magnets and decreases along the positive radial direction.

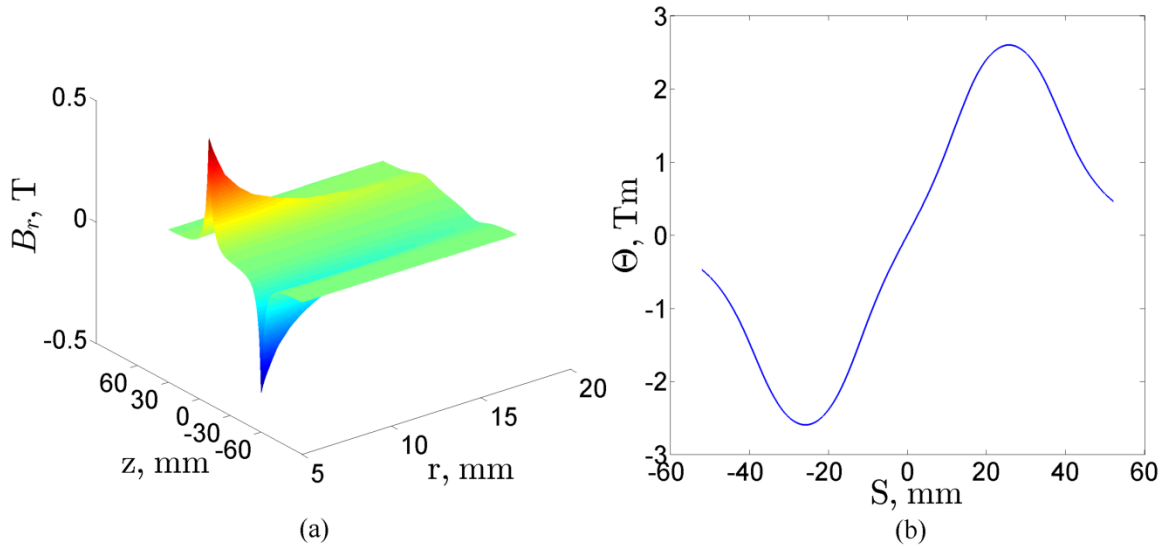

Figure 2.5. (a) Radial magnetic flux density of the oscillating magnet; (b) total transduction factor for two coils.

For each coil location S, which is defined as the distance between the center of the magnet and the center of the coil, the double integral in Eq. (2.5) is numerically computed using the trapezoidal method and the relationship between the total transduction factor $\Theta(S)$ and S is found and shown in Figure 2.5 (b). The maximum value of the transduction factor $\Theta_{max} = 2.596$ Tm corresponds to two locations $S = \pm 25.4$ mm, indicating that the maximum electrical damping can be achieved by placing one of the magnet ends at the center of the coil.

2.2.2 Experimental results

The damping effect of the electro-magnetic damper is first experimentally investigated before a detailed discussion on the model B TMD. The test is conducted on the standalone TMD system, including the oscillating magnets, the cantilever beam, the damper and the electric circuit. The system is fastened to a stationary base with a laser sensor capturing the displacement of the absorber mass (i.e. magnets). As listed in Table 2.1, the absorber mass is found to be 0.048 kg. The length of the cantilever beam is set to be 116 mm. The natural frequency of the TMD system

is found out to be $f_a = 14$ Hz through free vibration tests. Thus, the absorber stiffness is calculated as $k_a = 371.94$ N/m. By tapping the absorber mass gently, free vibration responses are generated. From the response data, the ratio of mechanical damping is found to be $\zeta_m = 0.002$. Thus the inherent mechanical damping coefficient is $c_m = 0.0357$ Ns/m.

In order to find out the electrical damping coefficients under different load resistances, the resistance of the load resistor R_{load} is varied from 0 to $200\ \Omega$. Multiple sets of free vibration tests are conducted to calculate damping ratios. The electrical damping coefficients are determined by subtracting the mechanical damping coefficient from the total damping coefficients. Figure 2.6 compares the identified electrical damping coefficients with the ones calculated using Eq. (2.10).

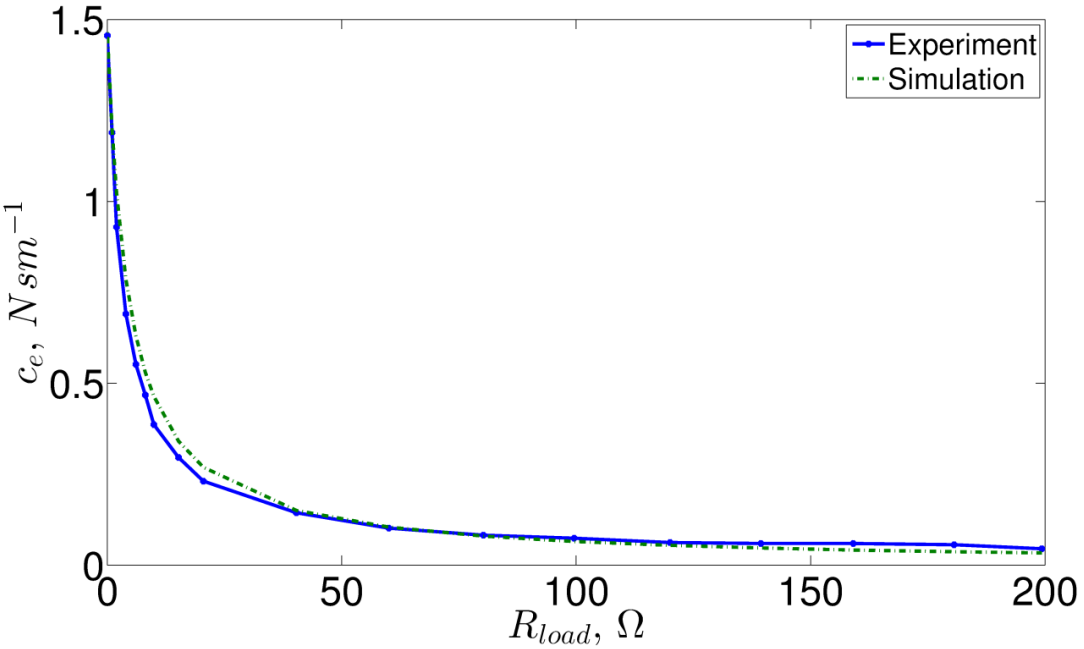

Figure 2.6. Electrical damping coefficients under different load resistances.

The identified values agree well with the analytical ones. The maximum electrical damping coefficient achieved by the damper is found to be $(c_e)_{\max} = 1.4156$ Ns/m when $R_{load} = 0\,\Omega$. In this case, this maximum value corresponds to a damping ratio of approximately 17%. During the experiment, it is observed that the absorber mass oscillates only 3 cycles when the electric circuit is directly closed. As the load resistance grows from zero to $40\,\Omega$, the damping coefficient decreases significantly to 0.1437 Ns/m. When the load resistance is increased further, the damping coefficient experiences a steady decay to 0.0447 Ns/m that corresponds to a damping ratio of 0.5%.

Chapter 3 Harmonically-excited Responses

The first tuning strategy is discussed in this chapter using the classical "fixed-points" theory. The detailed derivation of the optimum parameters for the model B TMD subjected to a ground motion in terms of relative displacements is presented first. With the employed electromagnetic damper, the efficiency on vibration control and energy harvesting is also discussed.

3.1 Derivation of optimum parameters

Consider a model B TMD shown in Figure 1.1 (b). In order to apply the "fixed-points" theory, the mechanical damping of the primary system is ignored. This is reasonable since the inherent primary damping is usually small and negligible comparing to the electrical absorber damping discussed in the previous chapter. When the system is subjected to a ground motion, the equations of motion can be given as,

$$m\ddot{x} + (k + k_a)x - k_a x_a = -m\ddot{y} \tag{3.1}$$

$$m_a\ddot{x}_a + c_a\dot{x}_a + k_a x_a - k_a x = -m_a\ddot{y} \tag{3.2}$$

where m and m_a are the primary mass and the absorber mass, respectively, k and k_a are the primary spring stiffness and the absorber spring stiffness, respectively, c_a is the damping coefficient of the absorber damper, x and x_a are the displacement of the primary mass relative to the base and the displacement of the absorber mass relative to the base, respectively and y is the base displacement. In order to find the steady state responses, assume a harmonic ground motion, i.e. $y = Ye^{j\omega t}$ where Y is the amplitude and ω the excitation frequency. The steady-state responses of the primary mass and absorber mass can be assumed to be:

$$x = Xe^{j\omega t}, x_a = X_a e^{j\omega t} \tag{3.3}$$

Substituting $y = Ye^{j\omega t}$ and Eq. (3.3) into Eqs. (3.1) and (3.2) results in:

$$\begin{bmatrix} -m\omega^2 + (k + k_a) & -k_a \\ -k_a & jc_a\omega - m_a\omega^2 + k_a \end{bmatrix} \begin{bmatrix} X \\ X_a \end{bmatrix} = \begin{bmatrix} m\omega^2 Y \\ m_a\omega^2 Y \end{bmatrix} \tag{3.4}$$

After some manipulation, the amplitude of the steady-state response of the primary mass is obtained as:

$$|X| = \omega^2 Y \sqrt{\frac{(c_a m\omega)^2 + (-mm_a\omega^2 + k_a m + k_a m_a)^2}{(-c_a m\omega^3 + c_a k\omega + c_a k_a \omega)^2 + (mm_a\omega^4 - km_a\omega^2 - k_a m\omega^2 - k_a m_a\omega^2 + kk_a)^2}} \tag{3.5}$$

The performance index is defined as the displacement transmissibility ratio given as:

$$G = \frac{|X|}{X_{st}} = \sqrt{\frac{(2\zeta r)^2 + [(\mu + 1)\beta^2 - r^2]^2}{(2\zeta r)^2(1 + \mu\beta^2 - r^2)^2 + [(1 - r^2)(\beta^2 - r^2) - \mu\beta^2 r^2]^2}} \tag{3.6}$$

with the following normalized variables

$$X_{st} = \frac{m\omega^2 Y}{k},\ \omega_p = \sqrt{\frac{k}{m}},\ \omega_a = \sqrt{\frac{k_a}{m_a}},\ \beta = \frac{\omega_a}{\omega_p},\ \mu = \frac{m_a}{m_p},\ \zeta = \frac{c_a}{2m_a\omega_p},\ r = \frac{\omega}{\omega_p} \tag{3.7}$$

X_{st} is defined as the static deflection of the primary mass due to an inertia force $m\omega^2 Y$, ω_p is the natural frequency of the primary system, ω_a is the natural frequency of the absorber system, β is called the frequency tuning ratio, μ is the mass ratio, ζ is the damping ratio and *r* is the exciting frequency ratio.

When the curves of *G* vs. *r* for different damping ratios are plotted, two fixed points (named as *P* and *Q* for convenience) can be observed. According to the optimality proposed by Hartog (1940), the optimum tuning happens when those two points have equal height and the curve passes through them horizontally. A detailed derivation on the optimum parameters β and ζ with regard to mass ratio μ is provided below.

To find the abscissas of points *P* and *Q*, Eq. (3.6) is expressed in the form,

$$G = \sqrt{\frac{A\zeta^2 + B}{C\zeta^2 + D}} \tag{3.8}$$

where,

$$\begin{aligned} A &= (2r)^2 \\ B &= [(\mu+1)\beta^2 - r^2]^2 \\ C &= (2r)^2(1+\mu\beta^2 - r^2)^2 \\ D &= [(1-r^2)(\beta^2 - r^2) - \mu\beta^2 r^2]^2 \end{aligned} \tag{3.9}$$

As *G* is independent of ζ at *P* and *Q*, we have $\frac{A}{B} = \frac{C}{D}$ which yields,

$$\frac{1}{1+\mu\beta^2 - r^2} = \pm\frac{(\mu+1)\beta^2 - r^2}{(1-r^2)(\beta^2 - r^2) - \mu\beta^2 r^2} \tag{3.10}$$

Negative sign should be chosen for the term on the right-hand side of the above equation as a plus sign would result in an expression of $-\beta\mu^2 = 0$. The solutions for Eq. (3.10) are,

$$r_{1,2} = \sqrt{\frac{(3\mu+2)\beta^2 + 2 \mp \sqrt{(\mu+2)^2\beta^4 + 4(\mu-2)\beta^2 + 4}}{4}} \tag{3.11}$$

The ordinates of points *P* and *Q* can be found by letting $\zeta \to \infty$ in Eq.(3.6):

$$G = \sqrt{\frac{1}{(1+\mu\beta^2 - r^2)^2}} \tag{3.12}$$

The optimum value for β is obtained by setting $G(r_1) = G(r_2)$,

$$\frac{1}{(1+\mu\beta^2 - r_1^2)^2} = -\frac{1}{(1+\mu\beta^2 - r_2^2)^2} \tag{3.13}$$

which yields the optimum frequency tuning ratio,

$$\beta_{opt} = \sqrt{\frac{2}{2-\mu}} \tag{3.14}$$

The abscissas and coordinates of points *P* and *Q* can be found by substituting β_{opt} in Eqs. (3.11) and (3.12),

$$r_{1,2} = \sqrt{\frac{2+\mu \mp \sqrt{2\mu}}{2-\mu}},\ G(r_1) = G(r_2) = \frac{2-\mu}{\sqrt{2\mu}} \tag{3.15}$$

Now Brock's approach (1946) is used to find the optimum damping ratios. In order for the curve of *G vs. r* to pass horizontally through point *P*, one first requires that it passes through a point P' of abscissa $r^2 = r_1^2 + \delta$ and the ordinate $G = \dfrac{2-\mu}{\sqrt{2\mu}}$, and then let ζ approaches to zero as a limit. From Eq. (3.6), one can have:

$$\zeta^2 = \frac{[(\mu+1)\beta^2 - r^2]^2 - G^2[(1-r^2)(\beta^2 - r^2) - \mu\beta^2 r^2]^2}{4r^2[G^2(1+\mu\beta^2 - r^2)^2 - 1]} \tag{3.16}$$

Substituting $r^2 = r_1^2 + \delta$ and $G = \dfrac{2-\mu}{\sqrt{2\mu}}$ into the above equation, the following can be derived:

$$\zeta^2 = \frac{A_0 + A_1\delta + A_2\delta^2 + A_3\delta^3 + \cdots}{B_0 + B_1\delta + B_2\delta^2 + B_3\delta^3 + \cdots} \tag{3.17}$$

Since Eq. (3.17) assumes the indeterminate form $\dfrac{0}{0}$ if $\delta = 0$ as the curve of *G* vs. *r* for all values of ζ passes through *P*, it is easy to see that $A_0 = B_0 = 0$. As δ is a very small number, one can neglect the higher order terms which results in,

$$\zeta^2 = \frac{A_1}{B_1} \tag{3.18}$$

Using the approximations: $r^4 = r_1^4 + 2r_1^2\delta, r^6 = r_1^6 + 3r_1^3\delta, r^8 = r_1^8 + 6r_1^4\delta$, the following can be obtained:

$$\begin{aligned} A_1 &= -4G^2 r_1^6 + 6G^2[1+(1+\mu)\beta^2]r_1^4 + 2\{1-2G^2\beta^2 - G^2[1+(1+\mu)\beta^2]^2\}r_1^2 \\ &\quad +2\beta^2\{G^2[1+(1+\mu)\beta^2] - (1+\mu)\} \\ B_1 &= 12G^2 r_1^4 - 16G^2(1+\mu\beta^2)r_1^2 + 4G^2(1+\mu\beta^2)^2 - 4 \end{aligned} \tag{3.19}$$

Now substituting r_1^2 of Eq. (3.15) and β^* of Eq. (3.14) into $G(r_1, \beta)$, the above equations yield,

$$\zeta_1^2 = \frac{\mu}{4(\mu-2)} \frac{\mu - 6 - 2\sqrt{2\mu}}{\mu + 2 - 2\sqrt{2\mu}} \tag{3.20}$$

Using similar procedure with r_2^2,

$$\zeta_2^2 = \frac{\mu}{4(\mu-2)} \frac{\mu - 6 + 2\sqrt{2\mu}}{\mu + 2 + 2\sqrt{2\mu}} \tag{3.21}$$

As suggested by Brock (1946), a convenient average value,

$$\zeta_{opt} = \sqrt{\frac{\zeta_1^2 + \zeta_2^2}{2}} = \frac{1}{2}\sqrt{\frac{\mu(\mu^2 - 8\mu - 12)}{(\mu-2)(\mu^2+2\mu+4)}} \tag{3.22}$$

can be used as the optimum damping ratio. The results obtained here are the same as those in literature (Xiang & Nishitani, 2015) where a differently defined damping ratio was used.

Figure 3.1 shows *G* vs. *r* for a system with the parameters of *m*=1.0 kg, *k*=8900 N/m and under different damping ratio. The frequency tuning ratio is set to the optimum value of $\beta_{opt} = 1.0398$.

The optimum damping ratio is calculated to be $\zeta_{opt} = 0.246$. The existence of two invariant points can be observed from Figure 3.1. Also, when the system is optimally tuned, the two fixed points have equal height and the curve of G vs. r passes through them almost horizontally (since the optimum damping ratio is not a global optimization solution).

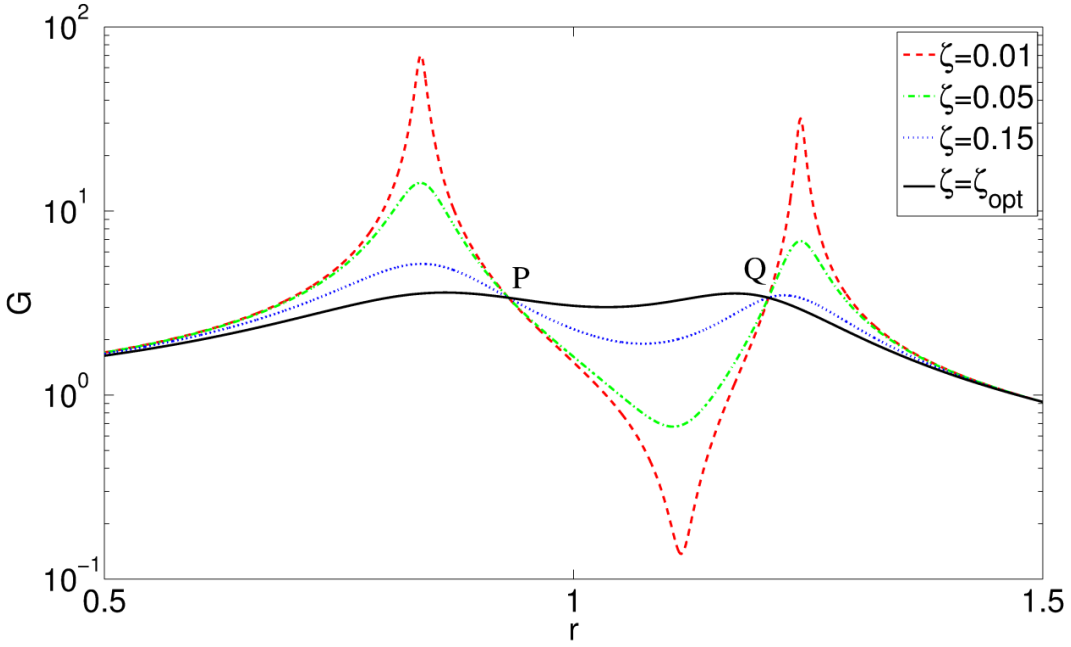

Figure 3.1. Displacement transmissibility ratio when $\mu = 0.15$ and β_{opt}=1.0398.

The constant tuning case is now also investigated. When $\beta_{opt} = 1$, as can be seen from Figure 3.2, the ordinate of point Q is greater than that of point P. The optimum damping ratio is considered to be the value for which the G vs. r curve passes horizontally through point Q.

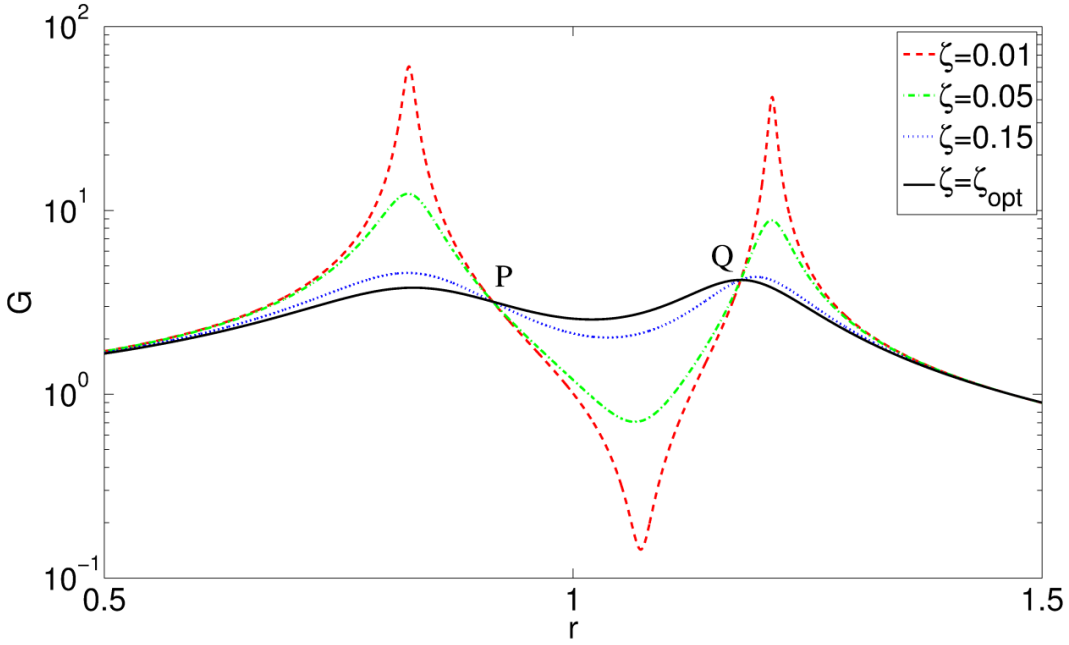

Figure 3.2. Displacement transmissibility ratio when $\mu = 0.15$ and β_{opt}.=1.0.

Substituting $\beta_{opt} = 1$ into Eq. (3.11) yields the abscissas of points *P* and *Q*,

$$r_{1,2} = \sqrt{\frac{3\mu + 4 \mp \sqrt{\mu^2 + 8\mu}}{4}} \tag{3.23}$$

For point *Q*, the ordinate is found to be:

$$G_2 = \sqrt{\frac{1}{(1 + \mu\beta^2 - r_2^2)^2}} = \sqrt{\frac{16}{(\mu - \sqrt{\mu^2 + 8\mu})^2}} \tag{3.24}$$

Following the similar procedure, Eq. (3.19) is now,

$$\begin{aligned} A_1 &= -4G^2 r_2^6 + 6G^2(2+\mu) r_2^4 + 2\{1 - 2G^2 - G^2(2+\mu)^2\} r_2^2 \\ &\quad + 2[G^2(2+\mu) - (1+\mu)] \\ B_1 &= 12G^2 r_2^4 - 16G^2(1+\mu) r_2^2 + 4G^2(1+\mu)^2 - 4 \end{aligned} \tag{3.25}$$

The optimum damping ratio is of the form,

$$\zeta_{opt} = \sqrt{\frac{A_1}{B_1}} = \sqrt{\frac{\mu}{8}\frac{\mu+12-\sqrt{\mu(\mu+8)}}{3\mu+4+\sqrt{\mu(\mu+8)}}} \tag{3.26}$$

after substituting r_2 of Eq. (3.23) and G_2 of Eq. (3.24). The optimum damping ratio shown in Figure 3.2 is calculated to be $\zeta_{opt} = 0.1931$.

3.2 Energy harvesting using the model B TMD

In this section, the effectiveness of using a model B TMD for energy harvesting is investigated. Consider the system described in Section 3.1. When the structure is subjected to harmonic ground excitation, the instantaneous input power can be defined as,

$$p_{in}(t) = -m\ddot{y}(t)[\dot{y}(t)+\dot{x}(t)] - m_a\ddot{y}(t)[\dot{y}(t)+\dot{x}_a(t)] \tag{3.27}$$

Substituting the assumption of $y(t) = Ye^{j\omega t}$, $x(t) = Xe^{j\omega t}$, $x_a(t) = X_a e^{j\omega t}$ into Eq. (3.27), the instantaneous input power can be written in the form of $p_{in}(t) = P_{in}e^{2j\omega t}$ and the amplitude of the input power P_{in} is found to be,

$$P_{in} = \omega^3 Y^2 \sqrt{\frac{\omega^2 c_a^2[mm_a\omega^2 - (m+m_a)(k+k_a)]^2 + (mkk_a - mm_a k\omega^2 + m_a kk_a)^2}{[kk_a - \omega^2(m_a k - m_a k_a - mk_a + mm_a\omega^2)]^2 + \omega^2 c_a^2(k_a + k - m\omega^2)^2}} \tag{3.28}$$

For the electro-magnetic damper, the instantaneous dissipated power is defined by,

$$p_e(t) = c_e\dot{x}_a^2(t) = c_a\dot{x}_a^2(t) = \frac{\Theta^2}{2R_{coil}+R_{load}}\dot{x}_a^2(t) \tag{3.29}$$

In the above equation, for the sake of simplicity, the mechanical damping of the absorber system c_m is neglected. The amplitude of the dissipated power by the electro-magnetic damper is found to be:

$$P_e = c_a \omega^6 Y^2 \frac{(mk_a + m_a k + m_a k_a - m m_a \omega^2)^2}{[k k_a - \omega^2 (m_a k - m_a k_a - m k_a + m m_a \omega^2)]^2 + \omega^2 c_a^2 (k_a + k - m\omega^2)^2} \tag{3.30}$$

To study the damper's effectiveness in vibration suppression, the dissipated power ratio, which is the ratio of the dissipated power amplitude to the input power amplitude, is defined as,

$$M_1 = \frac{P_e}{P_{in}} \tag{3.31}$$

A portion of the power dissipated by the electro-magnetic damper is harvested by the load resistor. The instantaneous harvested power is defined as $p_{load}(t) = i^2(t) R_{load}$. Recalling Eq. (2.8), this equation can be written as,

$$p_{load}(t) = \frac{\Theta^2 R_{load}}{(2R_{coil} + R_{load})^2} \dot{x}_a(t)^2 \tag{3.32}$$

Comparing Eqs. (3.29) and (3.32) yields,

$$f(R_{load}) = \frac{p_{load}(t)}{p_e(t)} = \frac{R_{load}}{2R_{coil} + R_{load}} \tag{3.33}$$

This term represents the percentage of power available for harvesting from the dissipated power by the electrical damping. It can be known that increase of load resistance results increase in the harvested power. This is contradictory to the previous results that a smaller load resistance is associated with higher damping ratio and better vibration suppression. It will be of interest to examine what influence the load resistance has on the harvested power with respect to the input power. The harvested power ratio, which is the ratio of the harvested power amplitude to the input power amplitude, is thus defined as,

$$M_2 = \frac{P_{load}}{P_{in}} \tag{3.34}$$

where P_{load} is the amplitude of harvested power.

Numerical investigation is performed to study Eqs. (3.31) and (3.34). The parameter values used in simulation are given as m = 0.34 kg, $m_a = 0.048$ kg and $k_p = 2520$ N/m. With the optimum tuning parameters, the absorber spring stiffness is found to be $k_a = 283$ N/m. The natural frequencies of the combined system is found to be 11.53 and 16.9 Hz. The harmonics base excitation has a frequency range of 6 to 20 Hz with the acceleration amplitude equals to $1\ \text{m/s}^2$. The load resistance varies from 0 to 100 Ω and the transduction factor of the coils is approximated as constant with a value of 2.596 Tm.

Figure 3.3 shows the simulation results of the dissipated power ratio. Figure 3.3 (a) is a contour plot of the dissipated power ratio vs. the exciting frequency and load resistance. It can be seen that high dissipated power ratio occurs around three frequencies 11.53 Hz, 15 Hz, and 16.9 Hz. Apparently, the first and third frequencies are the resonance frequencies. The second frequency is the so-called anti-frequency at which the greatest vibration suppression is achieved by the absorber. With a minimal vibration of the primary system, the absorber mass vibrates with a largest velocity amplitude, resulting in the dissipation of a greatest amount of power. When the system is excited around the aforementioned three frequencies, the dissipated power ratio is close to 1. When the exciting frequency is away from these three frequencies, the ratio decreases quickly with the increase of load resistance. A clearer view of how the exciting frequency influences the dissipated power ratio under different load resistance is shown in Figure 3.3 (b). When the load resistance is 0 Ω, the performance of the damper is robust when the exciting frequency is between 12 to 16 Hz. The dissipated power ratio experiences more fluctuations in the same frequency range when the load resistance increases.

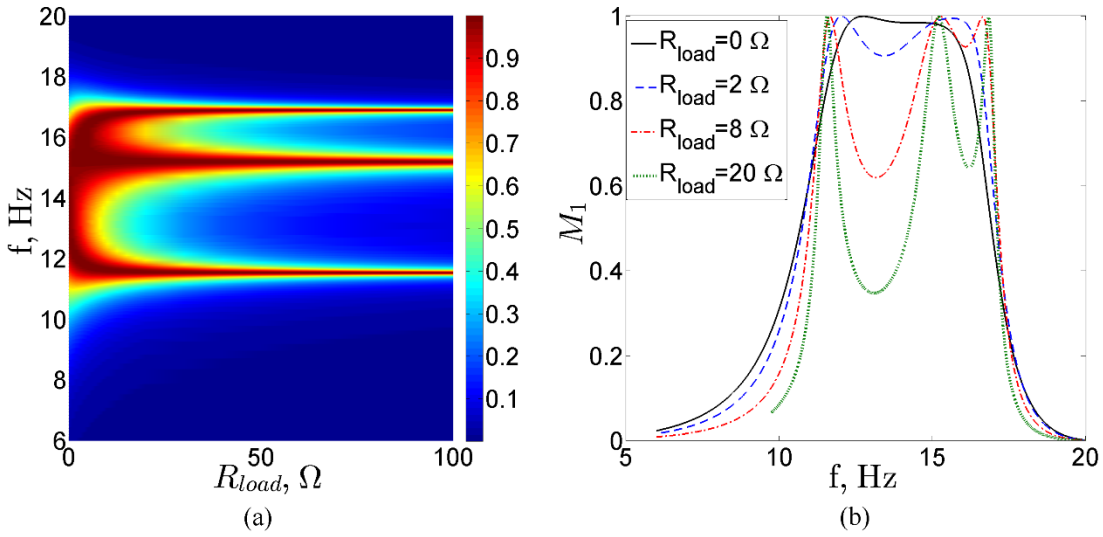

Figure 3.3. Dissipated power ratio.

The harvested power ratio is shown in Figure 3.4. When the system is excited with a frequency near the resonance frequencies (11.53 Hz and 16.9 Hz), or the anti-resonance frequency (15 Hz), the harvested power amplitude increases with an increasing load resistance and is able to reach approximately 95% of the input power amplitude when $R_{load} = 100\,\Omega$. When the exciting frequency is away from these ranges, the ratio increases from $0\,\Omega$ to its maximum point with a load resistance ranging from 5 to $20\,\Omega$ and decreases quickly with a higher load resistance. Recalling Eq. (3.33), increase of load resistance will result in a lower damping ratio but higher portion of power harvested from the dissipated power. Still in this case when the mechanical damping is not considered, the trade-off is not quite significant and both the satisfactory dissipated power ratio and harvested power ratio can be achieved within the load resistance range from 5 to $20\,\Omega$. Figure 3.4 (b) shows how the harvested power ratio varies with the exciting frequency under four different load resistances. Note that no power is harvested when $R_{load} = 0\,\Omega$. It can be seen that over the frequency range from 12 Hz to 16 Hz, the lower the load

resistance, the smaller and more uniform the harvested power ratio. With increase of the load resistance, the harvested power ratio increases with a large variation over the frequency range.

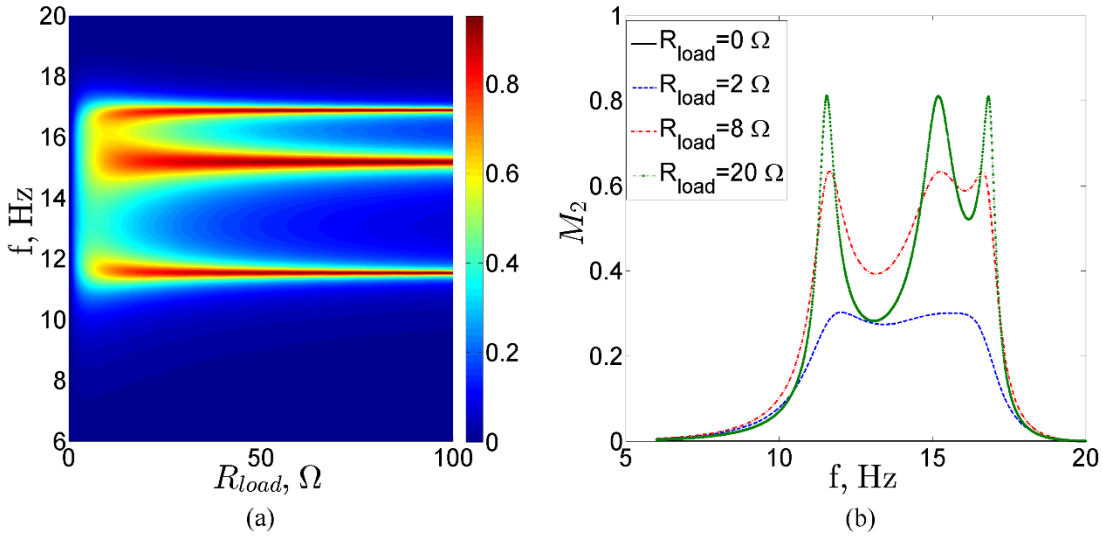

Figure 3.4. Harvested power ratio.

Presence of inherent mechanical damping is also considered. A low damping ratio of 1% is introduced into both the primary and absorber systems. Assuming that the inherent damping is low is justifiable as there is no need to control vibration of a heavily damped system The time history and amplitude of the instantaneous input power, dissipated power, and harvested power are obtained using Eqs. (3.27), (3.29) and (3.32), respectively. Given the range of the load resistance and exciting frequency, a large series of numerical simulation are conducted and the results are presented in Figure 3.5 and Figure 3.6. Comparing Figure 3.5 and Figure 3.3 reveals that a presence of a light inherent damping in the primary system and absorber system does not alter the general trend of the dissipated power ratio. However, the power dissipated by the electromagnetic damper becomes smaller than that of the system free of inherent damping. This is expected as portion of the input power is consumed by the inherent damping.

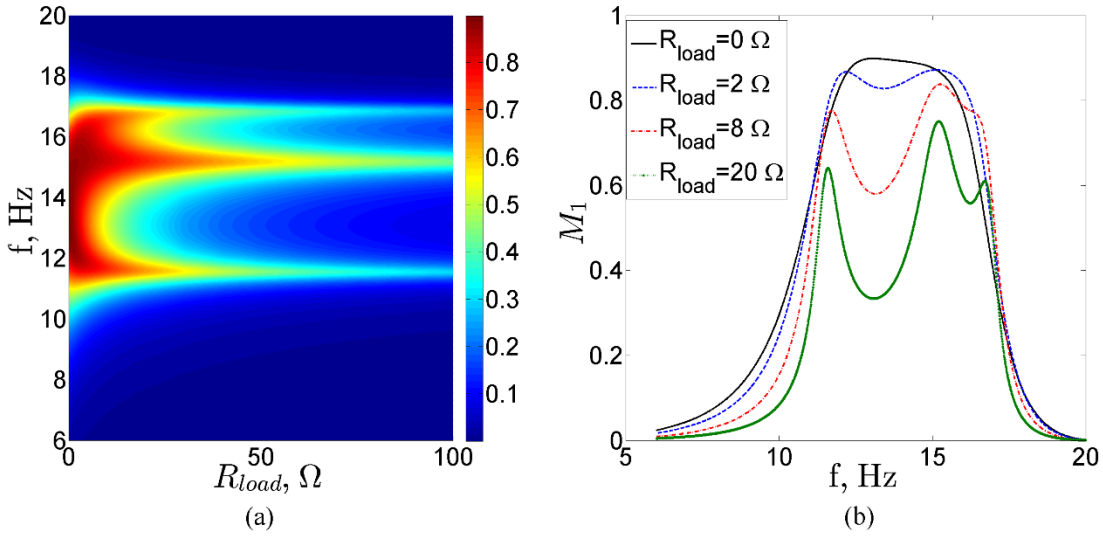

Figure 3.5. Dissipated power ratio when mechanical damping is present.

Comparing Figure 3.6 and Figure 3.4 yields the similar observation. However, when the inherent damping is considered, the trade-off between the power dissipation and the power harvesting becomes more obvious. When setting the load resistance to $15\,\Omega$ to achieve a better harvesting efficiency, the dissipated power ratio within the optimum operation range decreases to around 70% and the corresponding damping ratio is approximately 4%. The harvested power ratio is also closely examined in Figure 3.6 (b) under four different load resistances. Note that no power is harvested if $R_{load} = 0\,\Omega$. Comparing to other two cases, the case with $R_{load} = 8\,\Omega$ reveals a satisfactory balance between the magnitude and robustness of the harvested power ratio.

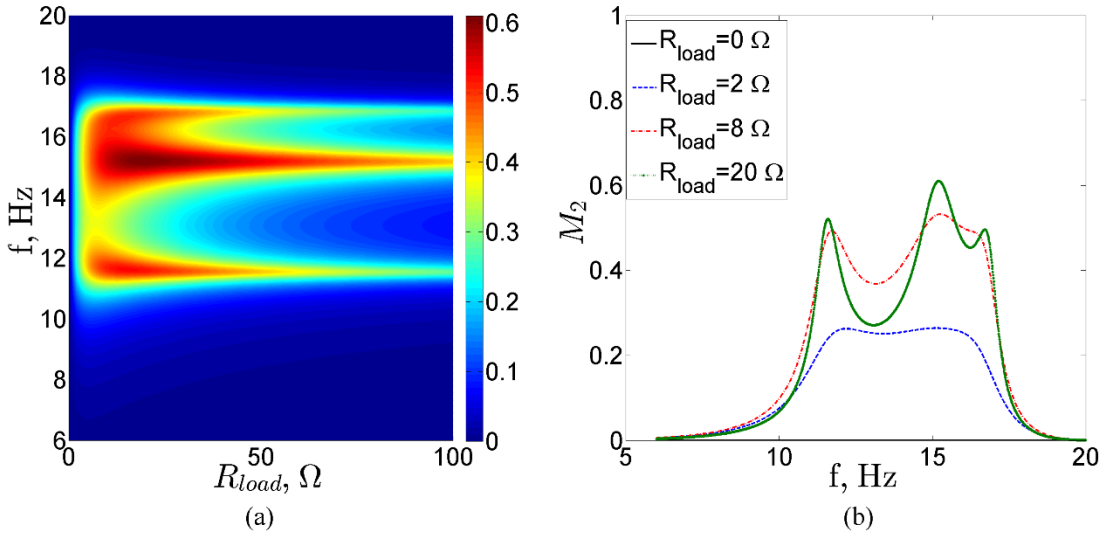

Figure 3.6. Harvested power ratio when mechanical damping is present.

Table 3.1 lists some quantitative results on the damper's performance with the inclusion of mechanical damping under four load resistances. The term $\Delta G / G_{f_p}$ measures the damping effect. Figure 3.7 illustrates the definition of ΔG and G_{f_p} where G_{f_p} is the displacement transmissibility ratio of the primary mass without the absorber and ΔG is the difference between the displacement transmissibility ratio of the primary mass after the absorber is attached and G_{f_p}. Compared to the original displacement transmissibility at resonance, i.e. G_{f_p}, the primary mass experiences much smaller resonance amplitudes with the absorber. The lower the load resistance, the more suppression is obtained. ΔG is also calculated at the original resonance frequency (13.7 Hz) and it can be seen that great suppression has been achieved. The harvested power ratio values at the resonance frequencies and the anti-resonance frequency are also listed in the table. As discussed earlier, the higher the load resistance, the higher the energy harvesting efficiency.

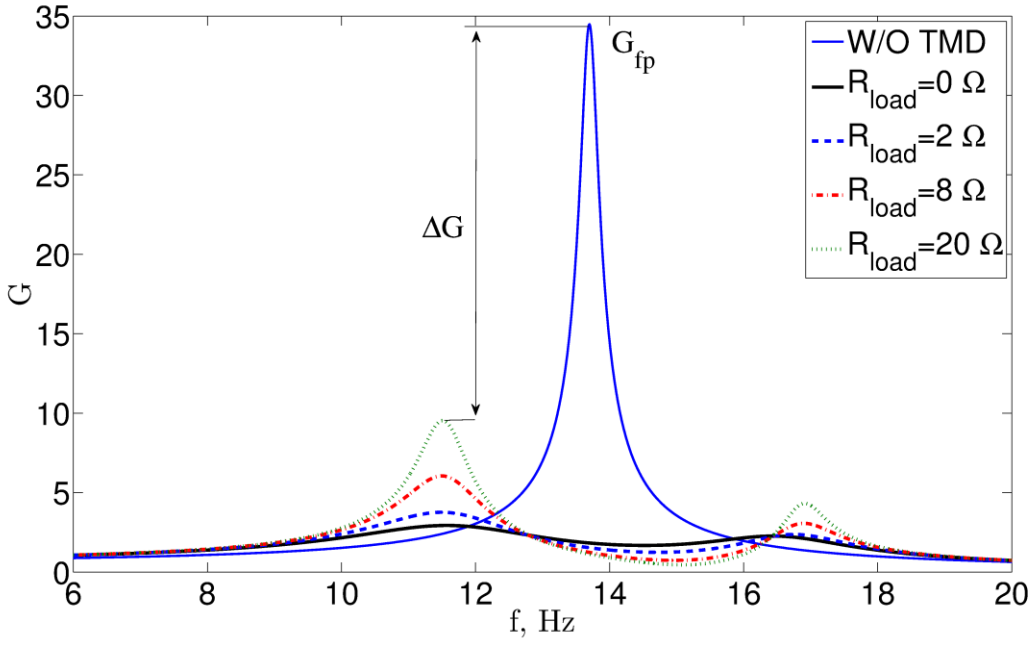

Figure 3.7. Displacement transmissibility ratio with mechanical damping, $\beta_{opt.}$=1.0373

Table 3.1. Quantitative results on vibration suppression and energy harvesting.

R_{load} (Ω)	$\Delta G / G_{f_p}$			M_2			P_e (mW)			P_{load} (mW)		
	f_1	f_p	f_2	f_1	f_{anti}	f_2	f_1	f_{anti}	f_2	f_1	f_{anti}	f_2
0	0.92	0.95	0.94	0	0	0	7.53	4.42	2.24	0	0	0
2	0.89	0.96	0.93	0.23	0.26	0.16	9.96	3.22	2.93	3.02	0.98	0.8
8	0.82	0.96	0.91	0.47	0.53	0.38	15.2	1.77	4.31	9.65	1.12	2.74
20	0.72	0.97	0.87	0.51	0.60	0.44	20.2	0.92	5.45	16.4	0.75	4.43

Table 3.1 also gives the values of the dissipated power and harvested power at the aforementioned three frequencies. Figure 3.8 shows P_e vs. f and P_{load} vs. f for four different load resistances, respectively. As it can be seen, P_e and P_{load} both reaches maximum values at natural frequencies. Despite the fact that more percentage of power is dissipated at lower load

resistances thus higher damping levels, P_e is lower, yet more uniform, at lower resistances. The story is different for P_{load} where its values increases with load resistance.

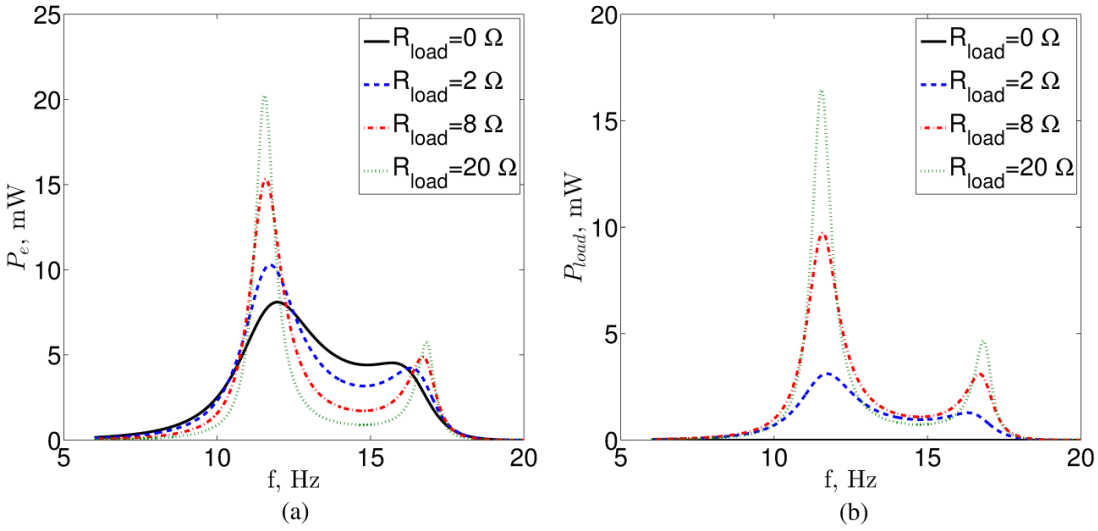

Figure 3.8. (a) Dissipated power; (b) Harvested power, with mechanical damping.

3.3 Experiment results

This subsection presents the experiment results to validate the previously derived optimum parameters and the simulation results on simultaneous vibration suppression and energy harvesting. Recall Figure 2.1 (b) where the photo of the experiment set-up is shown, the identified system parameters are listed in Table 3.2

Table 3.2. Identified system parameters

Primary mass	$m_p = 0.279$ kg
Primary natural frequency	$f_p = 13.7$ Hz
Primary stiffness	$k_p = m_p(2\pi f_p)^2 = 1951.28$ N/m
Primary damping ratio	$\zeta_p = 0.004$
Absorber mass	$m_a = 0.048$ kg

3.3.1 Vibration suppression

With a mass ratio of approximately 0.14, the optimum tuning parameters are found to be:

$$\beta_{opt} = \sqrt{\frac{2}{2-\mu}} = 1.037$$
$$\zeta_{opt} = \frac{1}{2}\sqrt{\frac{\mu(\mu^2 - 8\mu - 12)}{(\mu-2)(\mu^2+2\mu+4)}} = 0.241 \tag{3.35}$$

which requires an absorber stiffness of $k_a = 360.98$ N/m. The natural frequencies of the combined system are found to be 11.53 and 16.89 Hz. The frequencies corresponding to the two fixed points are also found to be 12.75 and 16.42 Hz.

It is expected that the system should be excited by ground motion with a constant base acceleration. An accelerometer attached to the base is used to monitor the acceleration. The root-mean-square (RMS) value of the base acceleration is computed and the amplitude of the signal sent to the shaker is adjusted accordingly. A base acceleration of 0.56 m/s^2 is used and kept relatively constant throughout the experiment.

First, a non-optimally tuned case is examined. The length of the absorber beam is set to 125 mm. The maximum load resistance used is set to be $20\ \Omega$ to ensure no direct contact between the oscillating magnets and the inner wall of the coil when the system is under resonance with the lowest damping ratio. By conducting a sweeping excitation test within the frequency range of 6 to 20 Hz, the displacement responses of the primary mass, absorber mass, and the base are recorded. Relatively displacement of the primary mass is calculated as well as the displacement transmissibility ratio. The test is then repeated for three other load resistances: $8\ \Omega$, $2\ \Omega$ and $0\ \Omega$ representing damping ratios of 6%, 11%, and 17% respectively. Figure 3.9 (a) shows the displacement transmissibility ratios under four different damping levels. It can be seen that there

exists two fixed points where all the curves intersect. The coordinates of these two points are $f_P = 12.6$ Hz, $G_P = 2.501$ and $f_Q = 16.0$ Hz, $G_p = 3.99$ respectively.

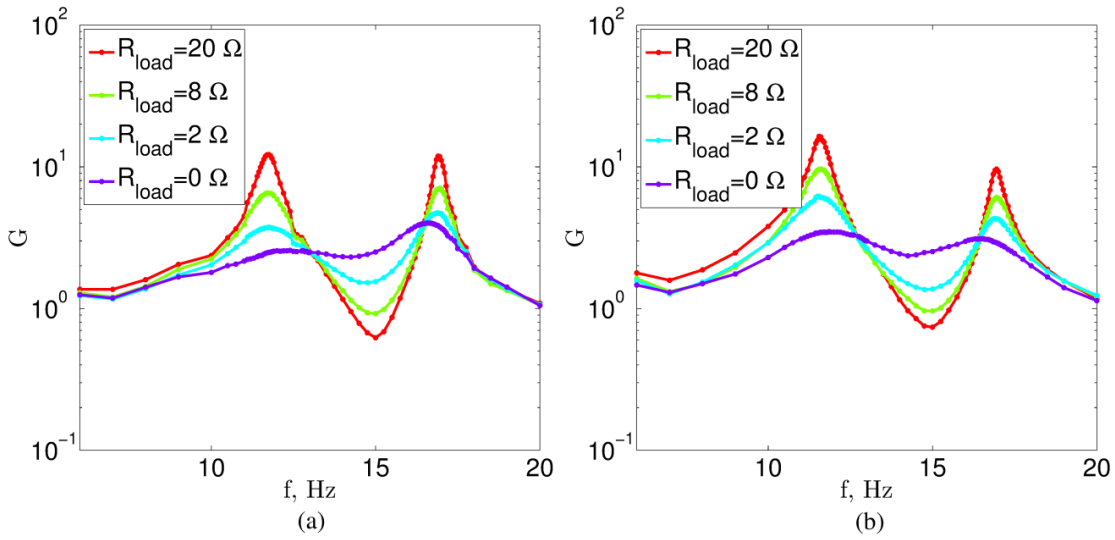

Figure 3.9. Displacement transmissibility of the primary mass under four different damping levels: (a) a non-optimally tuned system; (b) the optimally tuned system.

Then the optimum absorber beam length is determined using the above calculated absorber stiffness. After a slight tuning, the absorber beam length is set to be 117 mm. The experiment is repeated again and the result is shown in Figure 3.9 (b). As shown in the figure, the ordinates of the two fixed pints are almost equal to each other. The abscissa and ordinates of the fixed points are $f_P = 12.75$ Hz, $G_P = 3.145$ and $f_Q = 16.45$ Hz, $G_p = 3.111$ respectively, that are very close to the calculated ones. The system can be considered optimally tuned in respect to the frequency tuning ratio. It is worth noting that the optimum damping ratio is calculated to be 24.1%, corresponding to a damping coefficient of approximately 1.9 Ns/m. This is beyond the maximum damping coefficient achievable by the developed damper. Nevertheless, it should be noted that the displacement transmissibility curve becomes flatter as the load resistance decreases and damping ratio increases. When the load resistance is $0\,\Omega$, the curve reaches a

local maximum value at the second fixed point. It is reasonable to expect that the curve will reach its global maximum value at two fixed points if the optimum damping ratio is achievable.

3.3.2 Energy harvesting

When the system is optimally tuned with respect to the tuning parameter, the voltage across the load resistor is recorded under four different damping level ($R_{load} = 20,\ 8,\ 2,\ 0.2\ \Omega$, where the case of $R_{load} = 0.2\ \Omega$ is considered to be very close to the closed circuit case). As only the displacement signals available, the velocity and acceleration data are obtained through numerical differentiation. With the velocity and acceleration responses, the input power, dissipated power, and harvested power are calculated using Eqs. (3.27), (3.29) and (3.32), respectively.

It is worth noting that numerical differentiation is very susceptible to noise present in signals and each differentiation will amplify noise. To minimize the effect of noises, several measures are taken. First, to obtain better results on the numerical differentiation, the displacement signals are filtered by a low-pass filter with a cut-off frequency of 80 Hz. Then the filtered signals are interpolated using cubic spline approximations. The second measure is taken regarding to the calculation of the power amplitudes. Recalling Section 4, when the system is excited under a certain frequency, the instantaneous input power, dissipated power, and harvested power are essentially harmonic signals with constant offsets. Removing the offsets, the root-mean-square (RMS) value of the remaining signal is proportional to the peak-to-peak amplitude of the original signal. Thus in the experiment, the RMS value of the input power, dissipated power and harvested power over a time period of 15 seconds are conveniently calculated after the mean values of each variable are removed.

Figure 3.10 (a) shows the results of the percentage of the dissipated power amplitude to the input power amplitude. For each load resistance, the calculated dissipated power ratios are marked as

colored dots in the figure. It can be seen that noise still exerts effects after taking the aforementioned measures. Hence, cubic smooth spline is used to fit the data points which gives a better presentation of how the ratio changes with varying exciting frequencies and load resistance. A good agreement between the experiment results and the simulation results is observed. With decrease in load resistance, more power is dissipated in a steady manner within the exciting frequency range of 11 to 17 Hz. The maximum dissipated power ratio occurs around the exciting frequency of11.5, 17.0 and 15.0 Hz with the first two frequencies being the natural frequencies of the structure and the third one the anti-resonance frequency.

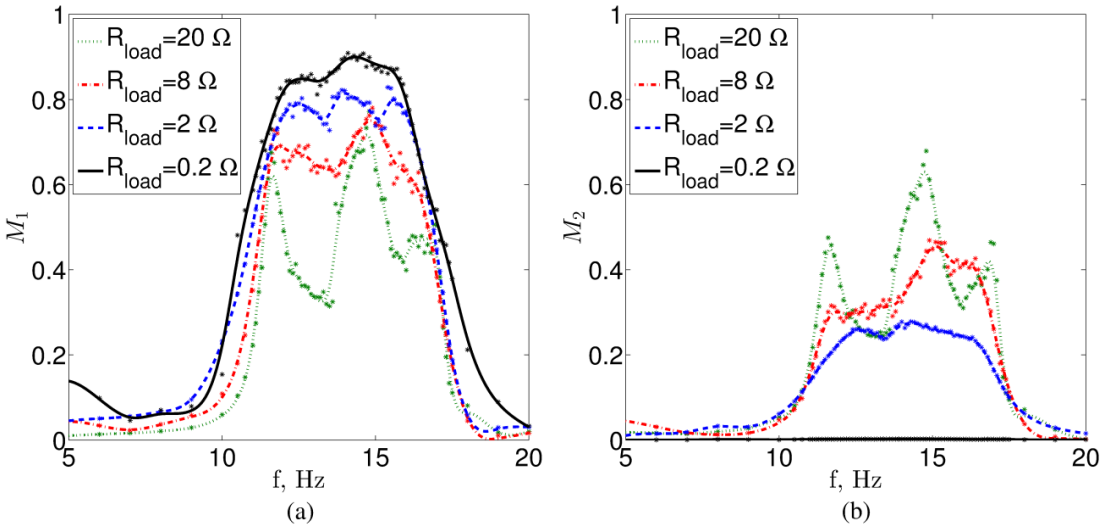

Figure 3.10. Experiment results: (a) Dissipated power ratio; (b) Harvested power ratio.

Figure 3.10 (b) shows the ratio of the harvested power amplitude to the input power amplitude. Optimum exciting frequency range remains the one within 11 to 17 Hz. Although the maximum harvesting ratio is achieved at $R_{load} = 20\ \Omega$, the curve experiences more fluctuation. When $R_{load} = 0.2\ \Omega$ the curve becomes quite flat with ratio values near 0.

Table 3.3 shows the values of the dissipated power ratio and the harvested power ratio under natural frequencies and anti-resonance frequency with four different load resistance. It also gives

the values of the dissipated power amplitude and harvested power amplitude obtained from Figure 3.11. The results from the experiment agree well with the simulation ones. P_e and P_{load} are reasonably small given the size of the apparatus and the excitation level.

Table 3.3. Experiment results on energy harvesting.

R_{load} (Ω)	M_1			M_2			P_e (mW)			P_{load} (mW)		
	f_1	f_{anti}	f_2	f_1	f_{anti}	f_2	f_1	f_{anti}	f_2	f_1	f_{anti}	f_2
0.2	0.72	0.87	0.54	0.00	0.00	0.00	1.93	1.38	0.83	0.02	0.01	0.01
2	0.65	0.74	0.49	0.19	0.26	0.18	2.33	0.59	0.59	0.65	0.21	0.21
8	0.64	0.74	0.45	0.28	0.45	0.30	6.44	0.57	1.83	3.91	0.48	1.50
20	0.61	0.63	0.51	0.44	0.57	0.46	7.26	0.68	2.06	5.20	0.57	1.89

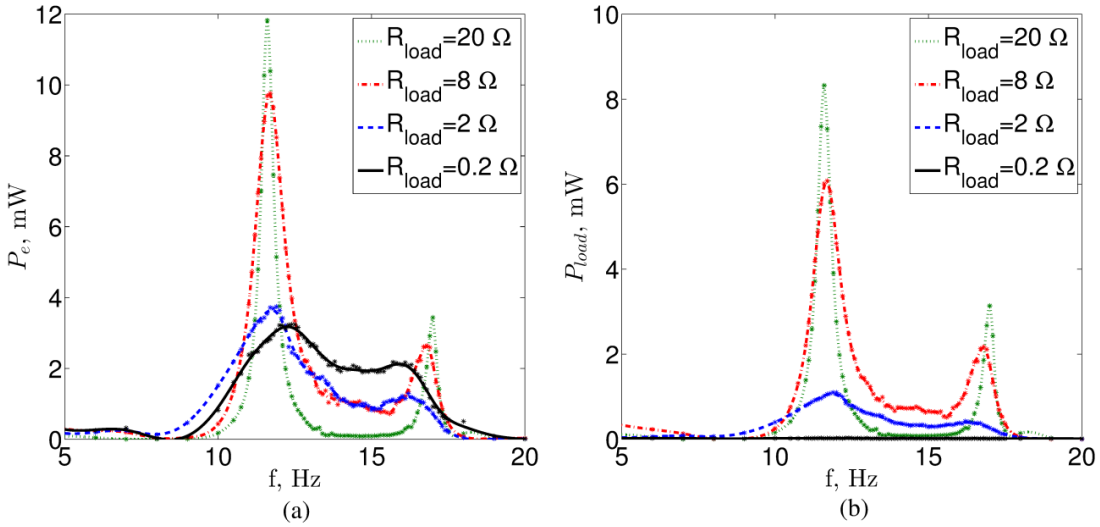

Figure 3.11. Experiment results: (a) dissipated power ratio; (b) harvested power ratio.

Chapter 4 Transient Responses

The transient responses of the system installed with a model B TMD are investigated in this chapter. The tuning strategies are based on: (a) the stability maximization criterion (SMC); and (b) the energy harvesting efficiency. Both the simulation and experiment results are presented to validate the tuning strategies.

4.1 System modelling

4.1.1 SMC

The SMC was developed by Nishitani and Matsihisa (1997) and applied to the design of a model B TMD by Xiang and Nishitani (2015). The idea of the SMC is outlined in this subsection and the energy harvesting efficiency is also considered.

Consider a linear system of the order N with a scalar input, the state-space model can be written as,

$$\dot{\boldsymbol{X}} = \boldsymbol{A}\boldsymbol{X} + \boldsymbol{B}\boldsymbol{u} \tag{4.1}$$

where $\boldsymbol{X}$ and $\boldsymbol{u}$ are the state vector and input, respectively, $\boldsymbol{A}$ is the state matrix or system matrix, and $\boldsymbol{B}$ is the input vector. If all the eigenvalues λ_i $(i = 1, \cdots, N)$ are distinctive, $\boldsymbol{A}$ is diagonalizable and semi-simple. The free vibration response can be written as,

$$\boldsymbol{X}(t) = \mathrm{e}^{\boldsymbol{A}(t-t_0)}\,\boldsymbol{X}(t_0) = \sum_{i=1}^{N} \boldsymbol{P}_i \boldsymbol{X}(t_0) e^{\lambda_i (t-t_0)} \tag{4.2}$$

where $\boldsymbol{P}_i$ is given by such Lagrange's interpolation polynomial as,

$$\boldsymbol{P}_i = \frac{(\boldsymbol{A}-\lambda_1\boldsymbol{I})\cdots(\boldsymbol{A}-\lambda_{i-1}\boldsymbol{I})(\boldsymbol{A}-\lambda_i\boldsymbol{I})\cdots(\boldsymbol{A}-\lambda_N\boldsymbol{I})}{(\lambda_i-\lambda_1)\cdots(\lambda_i-\lambda_{i-1})(\lambda_i-\lambda_{i+1})\cdots(\lambda_i-\lambda_N)} \tag{4.3}$$

The degree of stability is defined as the absolute value of the maximum real part of the eigenvalues,

$$\Lambda = -\max_i \mathrm{Re}(\lambda_i) \tag{4.4}$$

where $\Lambda > 0$ and the following inequality holds,

$$\left|\mathrm{e}^{\boldsymbol{A}(t-t_0)}\,\boldsymbol{X}(t_0)\right| \le \sum_{i=1}^{N} \left|\boldsymbol{P}_i \boldsymbol{X}(t_0)\right| e^{\Lambda(t-t_0)} \tag{4.5}$$

For a damped SDOF primary system equipped with a model B TMD, the equations of motion for the system are given as

$$m\ddot{x} + (k+k_a)x - k_a x_a + c\dot{x} = -m\ddot{y} \tag{4.6}$$

$$m_a\ddot{x}_a + c_a\dot{x}_a + k_a x_a - k_a x = -m_a\ddot{y} \tag{4.7}$$

where m and m_a are the primary mass and the absorber mass, respectively, k and k_a are the primary spring stiffness and the absorber spring stiffness, respectively, c and c_a are the damping coefficient of the primary structure and the absorber damper, respectively, x and x_a are the displacement of the primary mass relative to the base and the displacement of the absorber mass relative to the base, respectively and y is the base displacement. Similar to Section 3.1, a set of variables are defined to facilitate the analysis,

$$\omega_p = \sqrt{\frac{k}{m}},\ \omega_a = \sqrt{\frac{k_a}{m_a}},\ \beta = \frac{\omega_a}{\omega_p},\ \mu = \frac{m_a}{m_p},\ \zeta_p = \frac{c}{2m_a\omega_p}, \zeta_a = \frac{c_a}{2m_a\omega_a} \tag{4.8}$$

Equations. (4.6) and (4.7) now become,

$$\begin{aligned} &\ddot{x} + (\omega_p^2 + \mu\omega_a^2)x - \mu\omega_a^2 x_a + 2\zeta_p\omega_p\dot{x} = -\ddot{y} \\ &\ddot{x}_a + 2\zeta_a\omega_a\dot{x}_a + \mu\omega_a^2 x_a - \mu\omega_a^2 x = -\ddot{y} \end{aligned} \tag{4.9}$$

Introducing a new time scale $\tau = \omega_p t$, with $\ddot{x} = \frac{d^2x}{dt^2} = \omega_p^2 \frac{d^2x}{d\tau^2} = \omega_p^2 x'', \dot{x} = \frac{dx}{dt} = \omega_p \frac{dx}{d\tau} = \omega_p x'$,

Eq. (4.9) becomes,

$$\begin{aligned} &x'' + (1+\mu\beta^2)x - \mu\beta^2 x_a + 2\zeta_p \dot{x} = -\ddot{y} \\ &x_a'' + 2\zeta_a \dot{x}_a + \mu x_a - \mu x = -\ddot{y} \end{aligned} \tag{4.10}$$

With $\boldsymbol{X} = [x', x_a', x, x_a]^T$, the state matrix $\boldsymbol{A}$ can be expressed as,

$$A = \begin{bmatrix} -2\zeta_p & 0 & -(1+\mu\beta^2) & \mu\beta^2 \\ 0 & -2\beta\zeta_a & \beta^2 & -\beta^2 \\ 1 & 0 & 0 & 0 \\ 0 & 1 & 0 & 0 \end{bmatrix} \tag{4.11}$$

Solving the characteristic equation yields four eigenvalues in complex conjugate pairs denoted as $\lambda_{1,2} = -a_1 \pm jb_1, \lambda_{3,4} = -a_2 \pm jb_2$. By defining $g = \beta\zeta_a$, the characteristic equation can be obtained as,

$$\lambda^4 + 2(g+\zeta_p)\lambda^3 + (\beta^2 + 4\zeta_p g + 1 + \mu\beta^2)\lambda^2 + 2(\zeta_p\beta^2 + g + \mu g\beta^2)\lambda + \beta^2 = 0 \tag{4.12}$$

which can also be written using the eigenvalue solutions,

$$(\lambda + a_1 + jb_1)(\lambda + a_1 - jb_1)(\lambda + a_2 + jb_2)(\lambda + a_2 - jb_2) = 0 \tag{4.13}$$

Comparing the coefficients of λ from the above two equations, the following can be obtained,

$$2(g + \zeta_p) = 2(a_1 + a_2) \tag{4.14}$$

$$\beta^2 + 4\zeta_p g + 1 + \mu\beta^2 = s_1^2 + s_2^2 + 4a_1 a_2 \tag{4.15}$$

$$2(\zeta_p\beta^2 + g + \mu g\beta^2) = 2(a_1 s_1^2 + a_2 s_2^2) \tag{4.16}$$

$$\beta^2 = s_1^2 s_2^2 \tag{4.17}$$

where $s_1^2 = a_1^2 + b_1^2$ and $s_2^2 = a_2^2 + b_2^2$. It can be seen from Eq. (4.14) that the degree of stability will be maximized if $a_1 = a_2$ and meanwhile g is maximized. By substituting Eq. (4.14) into Eqs. (4.15) and (4.16) with the condition of $a_1 = a_2$, the following can be obtained,

$$\beta^2 + 4\zeta_p g + 1 + \mu\beta^2 - (g + \zeta_p)^2 = s_1^2 + s_1^2 \tag{4.18}$$

$$\zeta_p \beta^2 + g + \mu g \beta^2 = \frac{g + \zeta_p}{2}(s_1^2 + s_2^2) \tag{4.19}$$

Substituting Eq. (4.18) into Eq. (4.19) yields,

$$(g - \zeta_p)[g^2 - (1-\mu)\beta^2 - \zeta_p^2 + 1] = 0 \tag{4.20}$$

This will result in,

$$g = \sqrt{(1-\mu)\beta^2 + \zeta_p^2 - 1} \tag{4.21}$$

It can be seen that g will be maximized if β is maximized.

From Eq. (4.17) the following should be satisfied,

$$\beta \le \frac{s_1^2 + s_2^2}{2} \tag{4.22}$$

The equality holds when $s_1 = s_2$ and β will be maximized. Hence g will be maximized.

Based on the above discussion, the degree of stability will be maximized when (Xiang & Nishitani, 2015),

$$a_1 = a_2,\ s_1 = s_2 \tag{4.23}$$

4.1.2 Energy harvesting

The absorber's efficiency in energy harvesting is also considered. When the system is given an initial disturbance $(X_0, V_0, X_{a0}, V_{a0})$ where X_0 and V_0 are the initial relative displacement and relative velocity of the primary mass to the base, and X_{a0} and V_{a0} are the initial relative displacement and relative velocity of the absorber mass to the base. The initial energy of the system is give as,

$$E_{in} = \frac{1}{2}kX_0^2 + \frac{1}{2}mV_0^2 + \frac{1}{2}k_a(X_{a0} - X_0)^2 + \frac{1}{2}m_aV_{a0}^2 \tag{4.24}$$

Recalling Section 2.2, the current induced in the electric circuit has the expression of,

$$i = \frac{\Theta}{2R_{coil} + R_{load}}\dot{x}_a \tag{4.25}$$

The harvested power can be written as,

$$p_{load}(t) = i^2(t)R_{load} = \frac{\Theta^2 R_{load}}{(2R_{coil} + R_{load})^2}\dot{x}_a^2(t) \tag{4.26}$$

The total harvested energy from the transient response is the integration of the harvested power over the entire time period (T) of the vibration,

$$E_{load} = \int_o^T p_{load}(t)dt \tag{4.27}$$

A performance index is thus defined as the ratio of the harvested energy to the initial energy,

$$I = \frac{E_{load}}{E_{in}} \tag{4.28}$$

When the primary system is damped, Eq. (4.28) can also be written as,

$$I = \frac{E_{load}}{E_{cm} + E_{ce}} \tag{4.29}$$

where E_{cm} is the energy dissipated by the primary damping and E_{ce} is the energy dissipated by the absorber damper. After neglecting the mechanical damping of the absorber system which is negligible comparing to the electrical damping coefficient, the amount of harvested energy satisfies,

$$E_{load} = \frac{R_{load}}{2R_{coil} + R_{load}} E_{ce} \tag{4.30}$$

if one recalls Eq. (3.33).

4.2 Simulation results

To investigate the SMC criterion for designing a model B TMD and the energy harvesting efficiency, simulations are conducted using the following system parameters: m =0.34 kg, $f_p = 13.7$ Hz and $m_a = 0.048$ kg.

4.2.1 Undamped primary system

The primary system is first considered to be undamped. The optimum parameters derived according to the SMC are given as,

$$\begin{aligned} \beta_{opt} &= \frac{1-\sqrt{1-4\mu}}{2\mu} \\ \zeta_{opt} &= \frac{\sqrt{1-\sqrt{1-4\mu}}}{\sqrt{2}} \end{aligned} \tag{4.31}$$

which are calculated to be,

$$\begin{aligned} \beta_{opt} &= 1.205 \\ \zeta_{opt} &= 0.4124 \end{aligned} \tag{4.32}$$

To verify the derivation, the Genetic Algorithm toolbox in MATLAB is utilized with the problem defined as a multi-objective optimization. The objective functions are written as,

$$\begin{aligned} J_1(\beta, \zeta_a) &= \max(a_1, a_2) - \min(a_1, a_2) \\ J_2(\beta, \zeta_a) &= \left| \sqrt{a_1^2 + b_1^2} - \sqrt{a_2^2 + b_2^2} \right| \end{aligned} \tag{4.33}$$

The algorithm searches for the minimum value of $J_1(\beta, \zeta_a)$ and $J_2(\beta, \zeta_a)$ within the range of $0 \le \beta \le 1.5$ and $0 \le \zeta_a \le 1$. The optimum parameters are found to be,

$$\begin{aligned} \beta_{opt} &= 1.2048 \\ \zeta_{opt} &= 0.4122 \end{aligned} \tag{4.34}$$

with the following objective function values,

$$\begin{aligned} J_1(\beta, \zeta_a) &= 0.0001 \\ J_2(\beta, \zeta_a) &= 0.0352 \end{aligned} \tag{4.35}$$

The optimum values are nearly identical to the ones obtained through the analytical method, validating the derivation.

The transient response of the system is simulated with the initial condition of (0.01, 0, 0, 0). Figure 4.1 shows the displacement response of the primary mass when the system is tuned with respect to the SMC, both from the analytical method and Genetic Algorithm, and the "fixed-points" theory. It can be seen that the response of the primary structure decays faster when the system is tuned with the SMC than with the "fixed-points" theory.

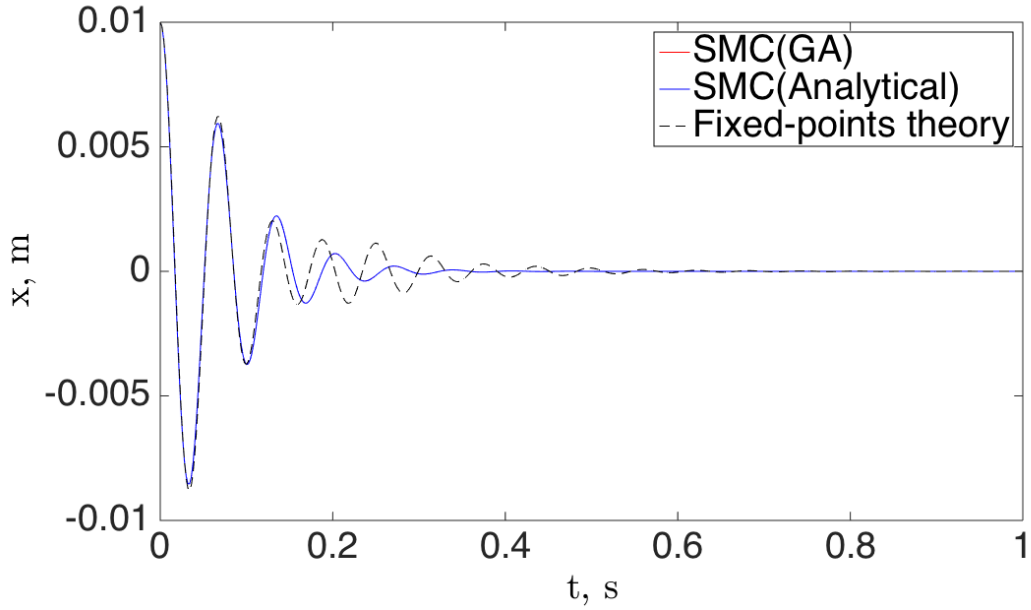

Figure 4.1. Transient response of the primary mass using different tuning methods

Simulations are also conducted to evaluate the relationship between the frequency tuning ratio β, the damping ratio ζ_a and the degree of stability. The eigenvalues of the system are calculated and the maximum value of the real parts of the eigenvalues is plotted in contour plot as shown in Figure 4.2. The maximum point corresponds to the condition when $\beta = 1.2$ and $\zeta_a = 0.41$. This is another validation on the analytical method as well as the optimization results using Genetic Algorithm. The plot also indicates that the system possesses higher degree of stability with both larger damping ratio ζ_a and frequency tuning ratio β.

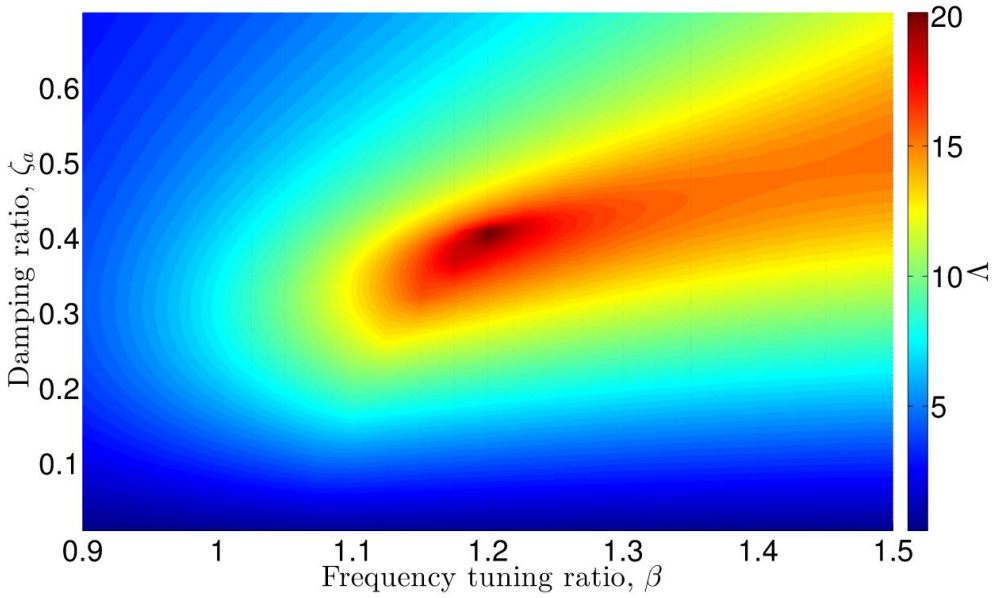

Figure 4.2. Degree of stability for an undamped primary system

When the mechanical damping in the absorber is neglected, i.e. $\zeta_a = \zeta_e = \dfrac{c_e}{2m_a\omega_a}$ where

$$c_e = \frac{\Theta^2}{2R_{coil} + R_{load}} \tag{4.36}$$

the degree of stability and the percentage of the harvested energy are investigated with respect to the frequency tuning ratio β and the load resistance R_{load}. As investigated in Chapter 2, the electromagnetic damper used in this study has a coil resistance of $R_{coil} = 2.3\ \Omega$ and a transduction factor of $\Theta = 2.596$ Tm. Figure 4.3 (a) shows a contour plot of the degree of stability. The highest degree of stability is achieved with the lowest load resistance. This is understandable as the damping ratio is reversely proportional to the load resistance. A higher damping coefficient is achieved with a lower load resistance. Figure 4.3 (b) shows the percentage of the harvested energy during the free response. As predicted in the previous section, given a load resistance, regardless of the β value, the percentage remains a constant. The larger the

load resistance, the higher the percentage of the harvested energy. When the load resistance has a value close to zero, almost no energy can be harvested. This represents a significant trade-off situation when the smallest load resistance is associated with the highest degree of stability but the least amount of the harvested energy.

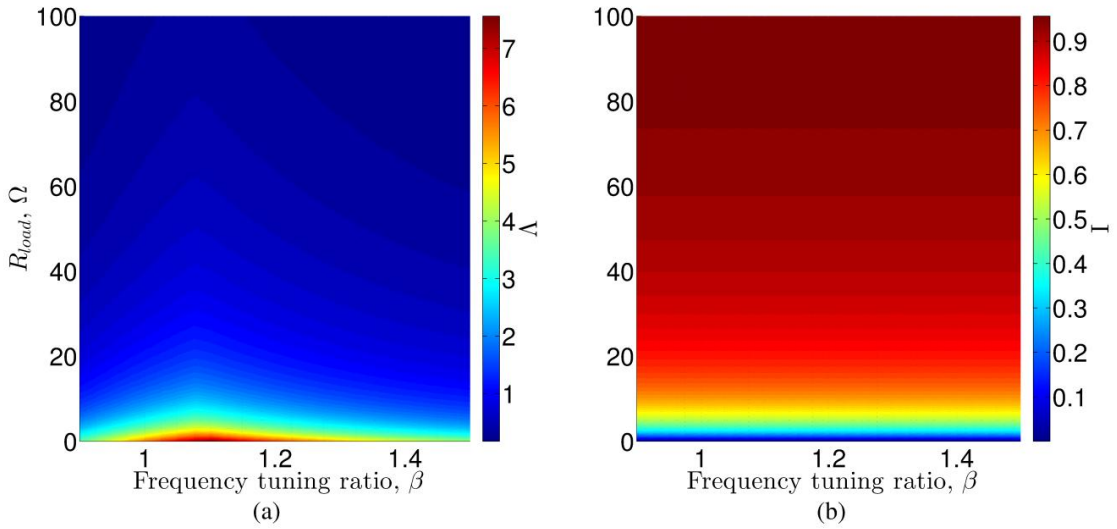

Figure 4.3. (a) Degree of stability; (b) percentage of harvested energy, when employing an electromagnetic damper.

4.2.2 Damped primary system

The optimum tuning parameters for a damped primary system with different mass ratio and primary damping level can be found in a comprehensive table in literature (Xiang & Nishitani, 2015). The procedure of using Genetic algorithm would be straightforward and thus not presented here.

Introducing a damping ratio of 1% into the primary system, the contour plot of the system's degree of stability is shown in Figure 4.4. The point with the maximum degree of stability corresponds to the tuning condition when $\beta = 1.2$ and $\zeta_a = 0.41$. The introduction of a low

level of the primary damping does not have a significant influence on the tuning parameters for the highest degree of stability.

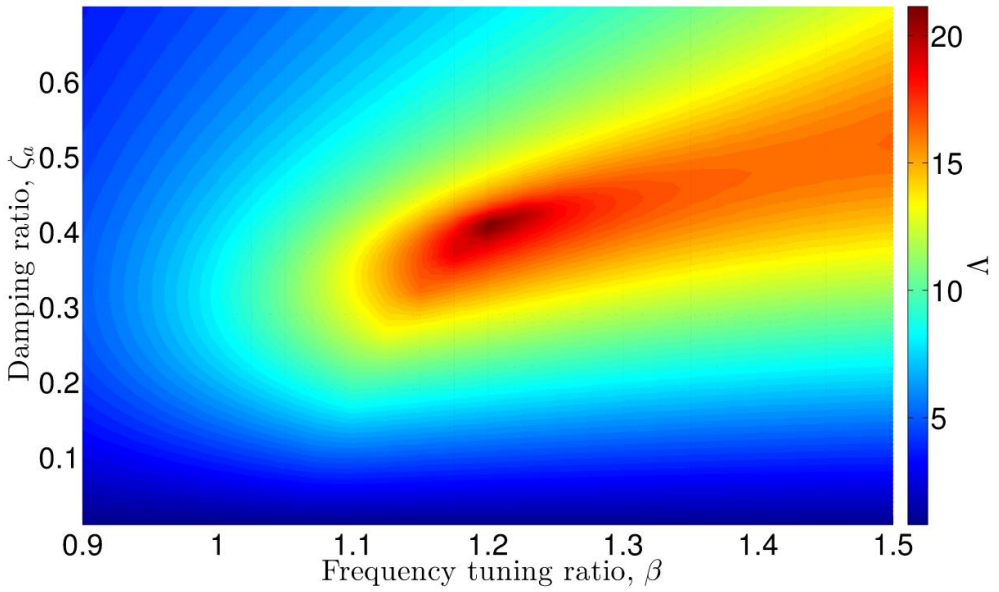

Figure 4.4. Degree of stability when ζ_p=0.01.

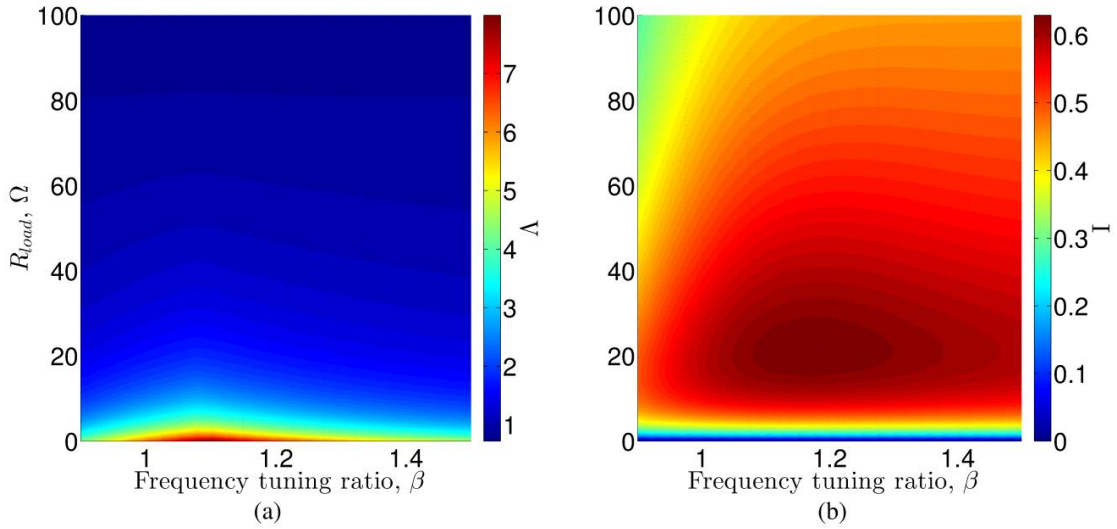

Figure 4.5. (a) Degree of stability; (b) percentage of harvested energy, when ζ_p=0.01.

Figure 4.5 shows the degree of stability and the percentage of the harvested energy when using an electromagnetic damper for the absorber. It can be seen that with the primary damping, a large load resistance does not necessarily bring a high amount of the harvested energy. This is because

the increase in load resistance will lower the absorber damping ratio and the amount of the energy dissipated by the absorber especially when the absorber damping level is lower than the primary damping one. Given a primary damping ratio, there exists an optimum load resistance value which remains the same regardless of the frequency tuning ratio β. As it can be obtained from Figure 4.5 (b), when the primary damping ratio equals to 1%, the optimum load resistance is approximately $20\ \Omega$ that corresponds to $\zeta_a = 3.3\%$.

Figure 4.6 shows the degree of stability and the percentage of the harvested energy when the primary damping ratio is set to be 5%. The optimum load resistance is found to be around $13\ \Omega$ that corresponds to $\zeta_a = 4.6\%$. Even though a closed-form solution for the optimum load resistance is not readily available, it can be concluded that for a system with higher primary damping, a lower optimum load resistance is required in order to harvest the maximum amount of energy from the transient response.

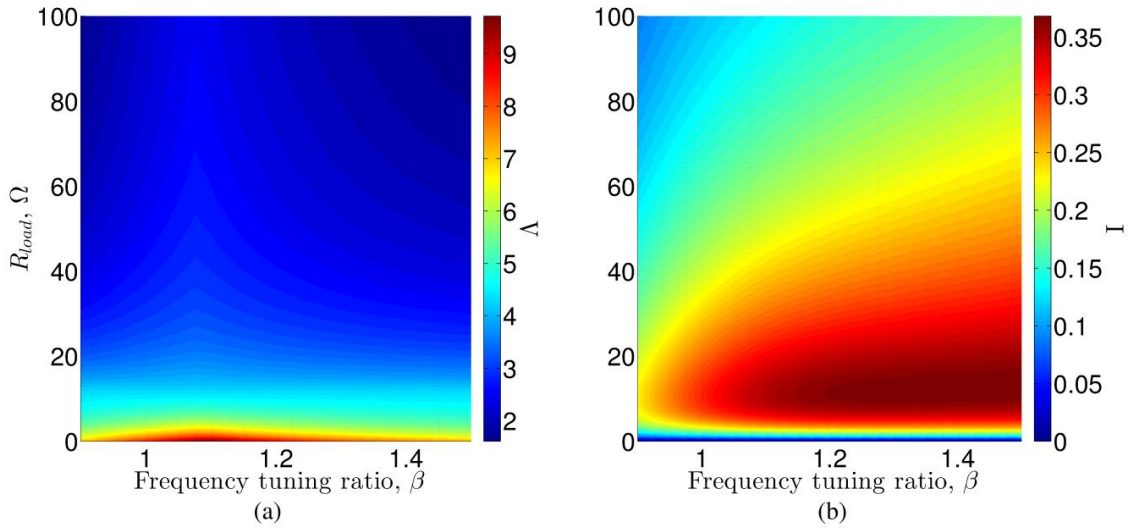

Figure 4.6. (a) Degree of stability; (b) percentage of harvested energy, when ζ_p=0.05.

Another feature to be observed from Figure 4.5 and Figure 4.6 is the trade-off situation between the degree of stability and the energy harvesting efficiency. To increase the system's stability, a

lower load resistance is desired for the maximum absorber damping coefficient. However, this does not guarantee the maximum amount of harvested energy and a certain load resistance is required in order to optimize the energy harvesting efficiency. Given this trade-off situation, a multi-objective optimization is proposed. The Genetic Algorithm toolbox in MATLAB is again utilized with the objective functions written as

$$\begin{aligned} J_1(\beta,\zeta_a) &= -\Lambda \\ J_2(\beta,\zeta_a) &= -I \end{aligned} \tag{4.37}$$

The negative sign is introduced as the algorithm searches for the minimum value of the objective functions. With a primary damping ratio of 1%, given the range of $0 \le \beta \le 1.5$ and $0 \le R_{load} \le 100$, the Pareto Front is found and shown in Figure 4.7. The parameters of the obtained solutions are listed in Table 4.1.

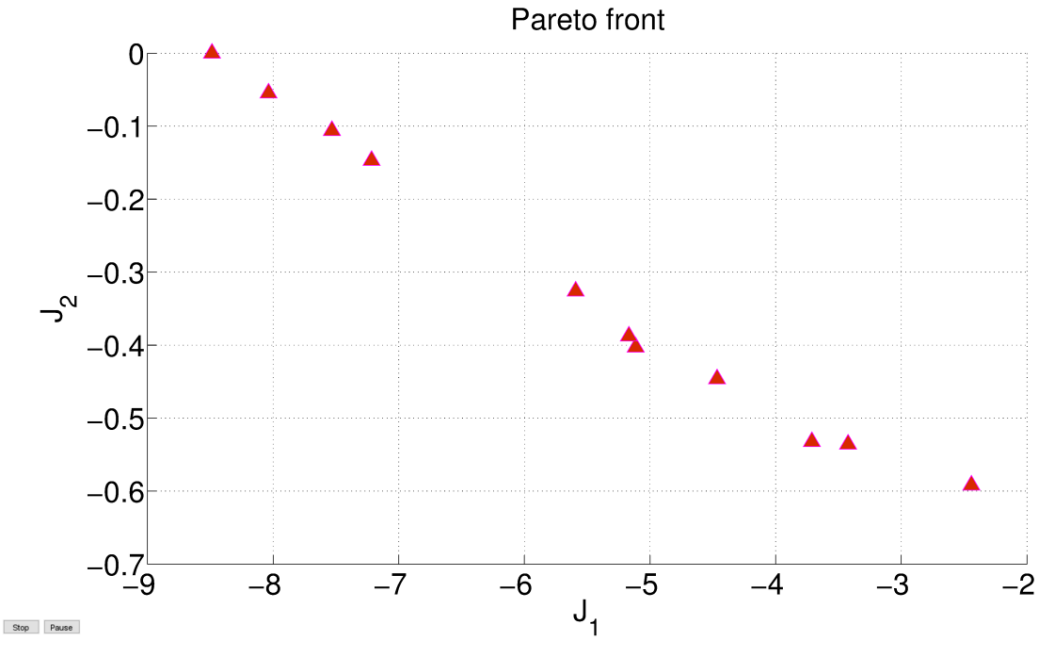

Figure 4.7. Pareto Front for the multi-objective optimization.

Table 4.1. Solutions in the Pareto Front

β	R_{load} (Ω)	I	Λ
1.0986	0.0005	0.0001	8.4866
1.0989	0.2652	0.0548	8.0363
1.1043	0.7932	0.1471	7.2165
1.1050	0.5432	0.1061	7.5317
1.1052	3.3349	0.4027	5.1139
1.1147	6.2759	0.5323	3.7120
1.1236	2.2825	0.3261	5.5917
1.1437	3.0811	0.3876	5.1684
1.1461	3.9818	0.4463	4.4665
1.2110	6.0371	0.5357	3.4238
1.4863	7.0964	0.5919	2.4423

For a multi-objective optimization problem, all solutions in the Pareto Front are considered equally optimal. As can be seen that the obtained frequency tuning ratio β are mainly within 1.0 to 1.3, and the load resistance R_{load} are under $10\,\Omega$. This provides a reference when designing the absorber and it's feasible that an optimum energy harvesting and vibration suppression device can be achieved with a properly chosen design criterion.

It is worth noting that the simulation results given here are subjected to the use of the specific electromagnetic damper involved in this study whose transduction factor is limited. For the primary system under investigation, the achievement of the optimum damping ratio requires the lowest load resistance for the electromagnetic damper. Figure 4.8 shows the two performance criteria when the transduction factor is equal to 10 Tm, which is near four times of that of the current damper. It can be seen that even though the optimum load resistance increases after raising the transduction factor, the achievement of the maximum degree of stability no longer

requires the lowest load resistance and the trade-off situation is less significant than the previous. It would be justifiable to assume that an electromagnetic damper with higher transduction factor would alleviate the trade-off significance and better achieve simultaneous optimum vibration suppression and energy harvesting.

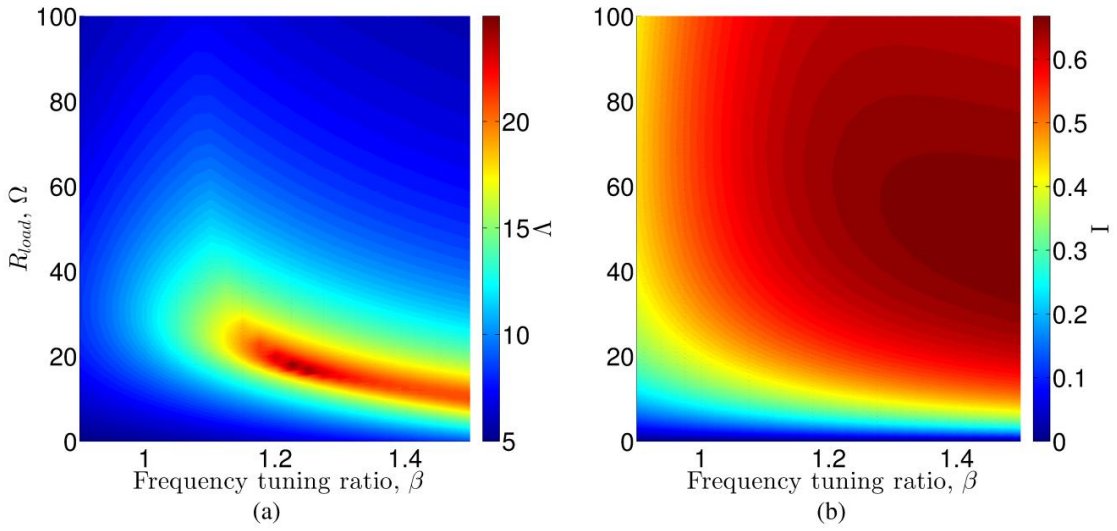

Figure 4.8. (a) Degree of stability; (b) percentage of harvested energy, when Θ=10 Tm and ζ_p=0.05.

4.3 Experimental results

This subsection presents the results of an experimental validation. The identified system parameters can be found in Table 3.2. For reference, an analytical model is established with the identified system parameters. By adjusting the length of the absorber beam, different frequency tuning ratio β can be achieved. The electromagnetic damper has a transduction factor of 2.596 Tm and the load resistance varies from 0 to $100\ \Omega$.

Transient response tests are conducted by releasing the primary mass at the displacement of 4.2 mm with $V_0 = 0$, $X_{a0} = 4.2$ (mm) and $V_{ao} = 0$. The displacements of the primary mass, absorber

mass and the voltage across the load resistance (V(t)) are recorded, and the energy harvesting efficiency, i.e. the percentage of the harvested energy to the initial energy, is calculated using,

$$\frac{E_{load}}{E_{in}} = \frac{\int_0^T \frac{V^2(t)}{R_{load}} dt}{\frac{1}{2} k X_0^2} \tag{4.38}$$

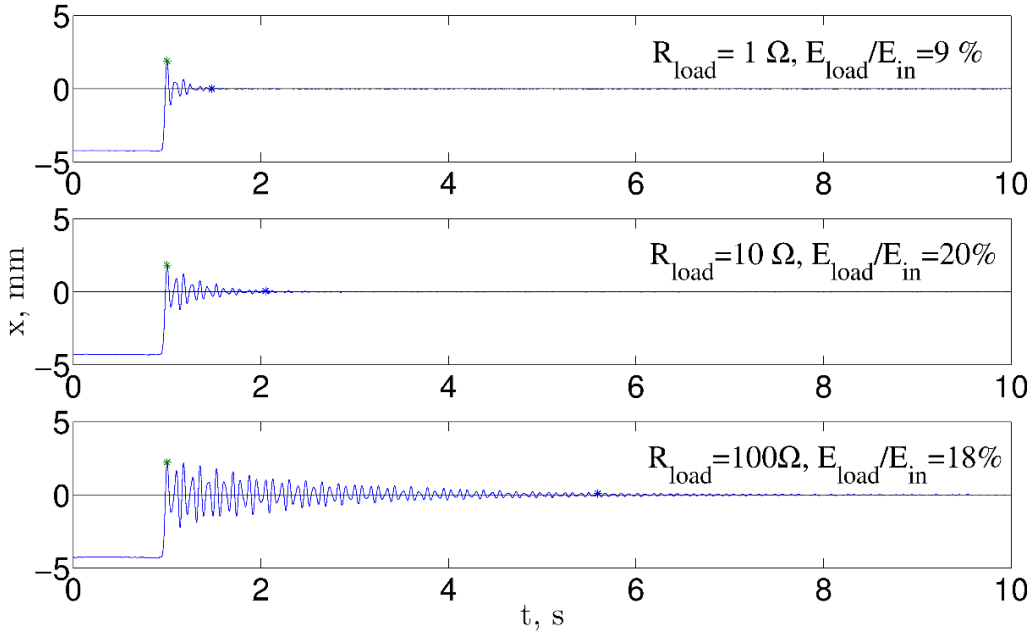

Figure 4.9. Transient responses of the primary mass with different load resistance when β=1.0.

Figure 4.9 shows the response of the primary mass under the load resistance of 1, 10 and 100 Ω when $\beta = 1.0$. Such a β value is achieved when the length of the absorber beam is adjusted so that the identified natural frequencies of the system are nearly identical to the ones calculated from the analytical model. As it can be seen that the lower the load resistance, the shorter the oscillation due to the higher absorber damping. In Figure 4.9, the first star points out the first oscillation peak while the second star indicates the first following peak whose amplitude is 5% of the first peak. As the degree of stability Λ is not readily available from the experimental results, a different criterion is adopted: the decaying time (Δt) the system needs for the

displacement of the primary mass to decrease to 5% of its first oscillation peak. The smaller the Δt value, the more stable the system. From Figure 4.9 one can also observe that the smallest load resistance corresponds to the smallest energy harvesting efficiency, which reminds us of the trade-off discussed previously. It should be noted that the calculated percentage is much lower than the expected because the primary mass is not able to oscillate back to a position close to the initial release position, resulting the initial energy to be higher in calculation than its actual value.

By changing the frequency tuning ratio, $\beta = 1.0, 1.1, 1.2$ and adjusting the load resistance to be R_{load}=0.2, 1, 2, 3, 4, 5, 6, 7, 8, 9, 10, 11, 12, 15, 20, 25, 50 and 100 Ω under each frequency tuning ratio, two criteria, Δt and percentage of the harvested energy, are investigated and the results are shown in Figure 4.10 and Figure 4.11, respectively. As the measurement is very susceptible to noise, similar to Section 3.3, band-pass filter and spline curve-fitting are used during data processing and the results are also presented using spline approximation.

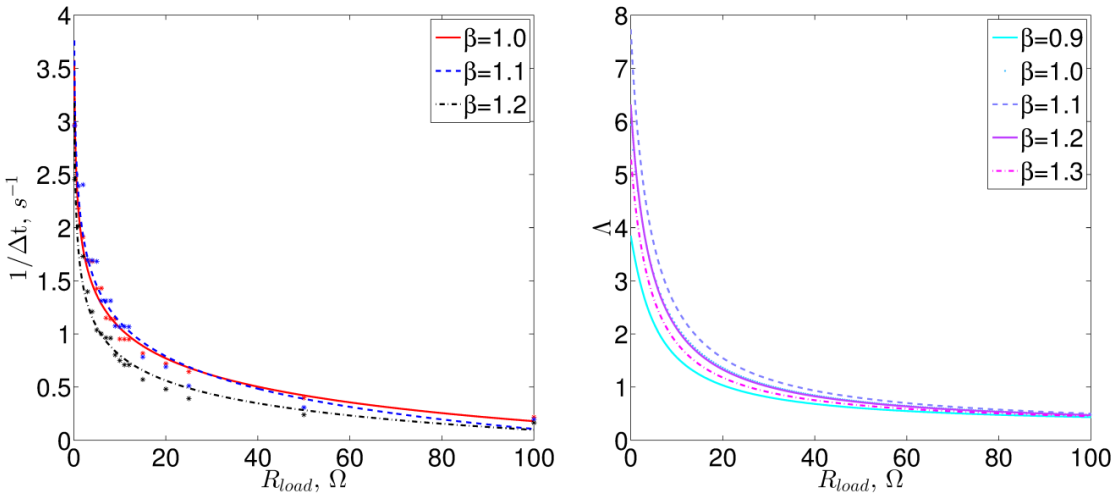

Figure 4.10. (a) Experiment results: Criterion 1, $1/\Delta t$; (b) simulation results, Λ.

Figure 4.10 (a) shows how system's stability varies with different load resistance under different frequency tuning ratio β. For comparison, simulations are conducted using the established analytical model with consideration of the primary damping and Figure 4.10 (b) gives the results on the degree of stability Λ. In order to better compare the experiment results with the simulation results, the reciprocal of the decaying time Δt is taken. The higher the load resistance, the lower $1/\Delta t$ value. The system is less stable with a low absorber damping. In addition, with a higher β value, the system needs more time to return to the equilibrium. From Figure 4.10 (b), it can be seen that system possesses higher stability as Λ increases when β increases from 0.9 to 1.1. When β further increases, the system becomes less stable. Given the possible error in measurement and the difficulty to achieve the exact β value, the experiment results agrees fairly with the simulation ones.

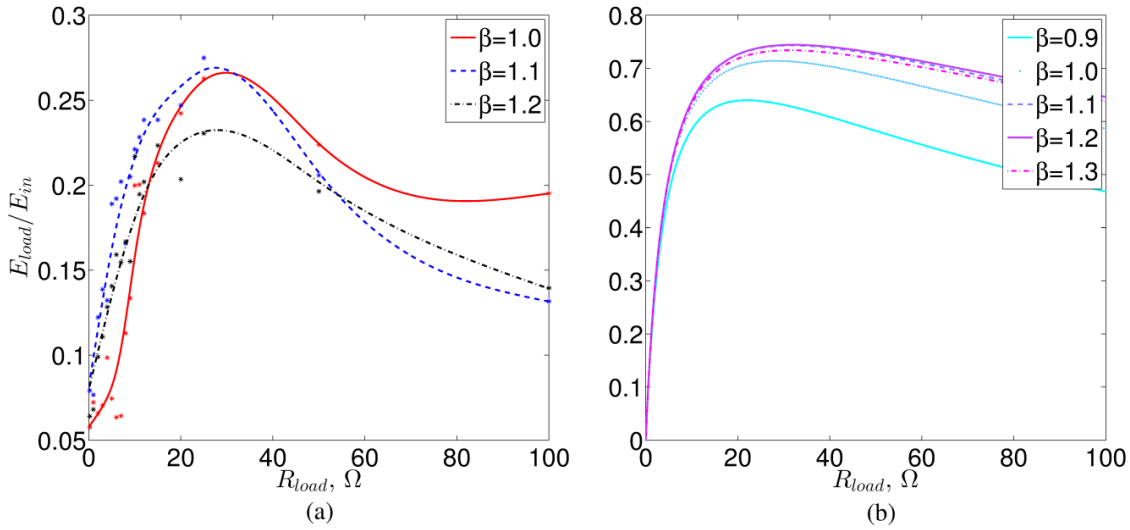

Figure 4.11. (a) Experiment results: Criterion 2, percentage of harvested energy, (b) simulation results.

Figure 4.11 (a) shows the percentage of the harvested energy under different tuning conditions. As it can be seen that there exists an optimum load resistance for three different β values where the highest percentage of harvested energy is achieved. The value for this optimum load resistance is found to be approximately $25\,\Omega$. The simulation results using the experiment system parameters are also given in Figure 4.11 (b). The percentage of harvested energy increases as β increase from 0.9 to 1.2 and start decreasing as β reaches 1.3. The optimum load resistance for the maximum percentage of harvested energy is found to be around $22\,\Omega$.

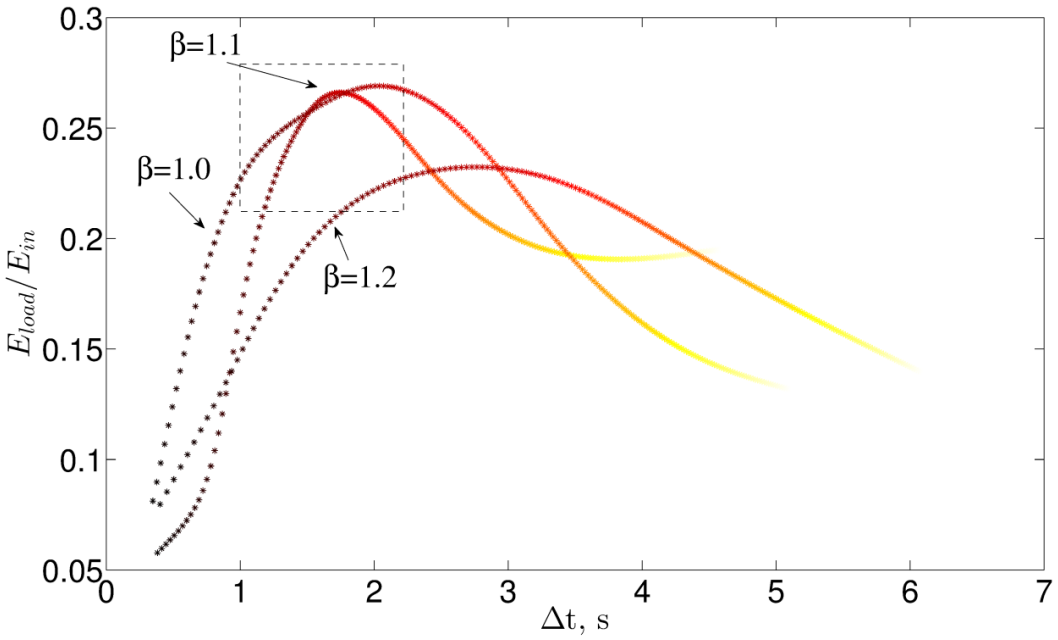

Figure 4.12. Experimental results of the energy harvesting criterion under different tuning conditions

Figure 4.12 provides references when achieving optimum tuning condition with respect to the two different criteria. The abscissa and ordinate present the two criteria, respectively and the color of the curve corresponds to different values of load resistance with a lighter color representing a higher load resistance. As discussed before, lower load resistance can help the system restore equilibrium faster at the cost of energy harvesting efficiency. A satisfying balance can be achieved when the value of the tuning parameters fall in the area enclosed by a square in Figure 4.12. Depending on the design criterion, an optimum vibration absorber/energy harvester can be achieved using the proposed apparatus.

Chapter 5 Responses under Random Excitation

In this chapter, the tuning strategies of a model B TMD are investigated with the intention to minimize the power dissipated by the primary damping and maximize the power dissipated by the absorber damper in order to achieve effective vibration suppression and harvest more energy from the system. Following the procedure employed by Zilletti, Elliott, and Rustighi (2012), analytical results are first provided with a detailed derivation according to different performance criteria. The effectiveness of a model B TMD will be examined based on the dissipated power both by the primary and absorber damping. The energy harvesting efficiency is also considered when the proposed electromagnetic damper is installed as the absorber damper. Simulations are conducted to validate the derivation and experimental results are also presented.

5.1 Analytical investigation

5.1.1 General discussion on the model B TMD

Consider a damped SDOF primary system installed with a model B TMD. The equations of motion can be written as,

$$\begin{aligned} m\ddot{x} + (k + k_a)x - k_a x_a + c\dot{x} &= -m\ddot{y} \\ m_a\ddot{x}_a + c_a\dot{x}_a + k_a x_a - k_a x &= -m_a\ddot{y} \end{aligned} \tag{5.1}$$

The parameters have been defined in the previous chapters. To measure the response magnitudes the mean square relative velocity is used (Zilletti et al., 2012),

$$E[V^2] = \int_{-\infty}^{\infty} |G|^2 S_y(\omega) d\omega \tag{5.2}$$

$$E[V_a^2] = \int_{-\infty}^{\infty} |G_a|^2 S_y(\omega) d\omega \tag{5.3}$$

where G is the velocity response function of the primary mass, G_a is that of the absorber mass and $S_y(\omega)$ is the input mean square spectral density function. In order to find out the velocity response functions of the primary and absorber mass, harmonic ground motion $y = Ye^{j\omega t}$ is first assumed. Thus the steady-state responses of the primary system and absorber system are defined by $x = Xe^{j\omega t}$ and $x_a = X_a e^{j\omega t}$, respectively. The steady-state velocity response magnitudes of the primary mass and the absorber mass are found to be,

$$V = (j\omega)\bullet X = (j\omega)\bullet\omega^2 Y\frac{a_1' + jb_1'}{c' + jd'} \tag{5.4}$$

$$V_a = (j\omega)\bullet X_a = (j\omega)\bullet\omega^2 Y\frac{a_2' + jb_2'}{c' + jd'} \tag{5.5}$$

where,

$$\begin{aligned}
a_1' &= k_a m + k_a m_a - m m_a\omega^2 \\
b_1' &= c_a m\omega \\
a_2' &= k_a m + k m_a + k_a m_a - m m_a\omega^2 \\
b_2' &= c m_a\omega \\
c' &= k k_a - k m_a\omega^2 - k_a m_a\omega^2 - k_a m\omega^2 + m m_a\omega^4 - c c_a\omega^2 \\
d' &= c_a k_a\omega + c_a k\omega - c_a m\omega^3 + c k_a\omega - c m_a\omega^3
\end{aligned} \tag{5.6}$$

By defining the following variables,

$$\omega_p = \sqrt{\frac{k}{m}}, \omega_a = \sqrt{\frac{k_a}{m_a}}, \beta = \frac{\omega_a}{\omega_p}, \mu = \frac{m_a}{m_p}, \zeta_p = \frac{c}{2m\omega_p}, \zeta_a = \frac{c_a}{2m_a\omega_p}, r = \frac{\omega}{\omega_p} \tag{5.7}$$

Equations (5.4) and (5.5) can be normalized as the following velocity response functions,

$$G = \frac{V}{\omega_p(\frac{m\omega^2 Y}{k})} = \frac{-2\zeta_a r^2 + jr[(1+\mu)\beta^2 - r^2]}{[(1-r^2)(\beta^2 - r^2) - (\mu\beta^2 + 4\zeta_p\zeta_a)r^2] + 2jr[(\beta^2 - r^2)\zeta_p + (1+\mu\beta^2 - r^2)\zeta_a]}$$

(5.8)

$$G_a = \frac{V_a}{\omega_p(\frac{m_a\omega^2 Y}{k})} = \frac{-2\zeta_p r^2 + jr[(1+\mu)\beta^2 + 1 - r^2]}{[(1-r^2)(\beta^2 - r^2) - (\mu\beta^2 + 4\zeta_p\zeta_a)r^2] + 2jr[(\beta^2 - r^2)\zeta_p + (1+\mu\beta^2 - r^2)\zeta_a]}$$

(5.9)

If the input spectrum is assumed to be ideally white, i.e. $S_y(\omega) = S_0$, Eqs. (5.2) and (5.3) can then be re-written as,

$$E[V^2] = S_0 \int_{-\infty}^{\infty} |G|^2 d\omega = \omega_p S_0 \int_{-\infty}^{\infty} |G|^2 dr \tag{5.10}$$

$$E[V_a^2] = S_0 \int_{-\infty}^{\infty} |G_a|^2 d\omega = \omega_p S_0 \int_{-\infty}^{\infty} |G_a|^2 dr \tag{5.11}$$

Two indexes are defined as,

$$I_{p1} = \frac{cE[V^2]}{4\pi S_0 k} \tag{5.12}$$

$$I_{p2} = \frac{c_a E[V_a^2]}{4\pi S_0 k} \tag{5.13}$$

where the constant $2\pi S_0 k$ is introduced to ensure that the performance indexes are dimensionless. The index I_{p1} represents the power dissipated by the primary damping while the index I_{p2} the power dissipated by the absorber damping. Based on Eq. (5.10), the mean square value of the relative velocity of the primary mass times the mechanical damping *c* can be expressed as follow,

$$cE[V^2] = S_0 k(2\zeta_p)\int_{-\infty}^{\infty}|G|^2 dr \tag{5.14}$$

Similarly based on Eq. (5.11) for the absorber damping,

$$c_a E[V_a^2] = S_0 k(2\mu\zeta_a)\int_{-\infty}^{\infty}|G_a|^2 dr \tag{5.15}$$

Thus the performance indexes become,

$$I_{p1} = \frac{\zeta_p}{2\pi}\int_{-\infty}^{\infty}|G|^2 dr \tag{5.16}$$

$$I_{p2} = \frac{\mu\zeta_a}{2\pi}\int_{-\infty}^{\infty}|G_a|^2 dr \tag{5.17}$$

Equation (5.16) is investigated first. By writing Eq. (5.8) into a convenient form, one has

$$G = \frac{-jr^3 B_3' - r^2 B_2' + jrB_1' + B_0'}{r^4 A_4' - jr^3 A_3' - r^2 A_2' + jrA_1' + A_0'} \tag{5.18}$$

where,

$$A_0' = \beta^2, A_1' = 2\zeta_a + 2\mu\beta^2\zeta_a + 2\beta^2\zeta_p, A_2' = 1 + \mu\beta^2 + \beta^2 + 4\zeta_a\zeta_p, A_3' = 2\zeta_p + 2\zeta_a, A_4' = 1,$$
$$B_0' = 0, B_1' = \mu\beta^2 + \beta^2, B_2' = 2\zeta_a, B_3' = 1 \tag{5.19}$$

The integral in Eq. (5.16) can be performed using the formula in literature (Newland, 2012) and it results in,

$$I_{p1} = \frac{1}{2\pi}\frac{1}{2}\frac{\begin{array}{c}\zeta_p\pi(4\mu\beta^2\zeta_a^2\zeta_p + 4\beta^2\zeta_p\zeta_a^2 + \mu^2\beta^4\zeta_p + \mu\beta^4\zeta_p - 2\beta^2\zeta_a \\ +4\zeta_a^3 + \mu\beta^4\zeta_a + 4\beta^2\zeta_a\zeta_p^2 + 4\zeta_p\zeta_a^2 + 4\mu\beta^2\zeta_a^3 + \beta^4\zeta_a + \zeta_a)\end{array}}{\begin{array}{c}2\mu\beta^2\zeta_a\zeta_p + \mu^2\beta^4\zeta_a\zeta_p + 4\mu\beta^2\zeta_a^2\zeta_p^2 + 4\mu\beta^2\zeta_a^3\zeta_p - 2\beta^2\zeta_p\zeta_a + \mu\beta^4\zeta_a^2 \\ +\mu\beta^4\zeta_p^2 + \beta^4\zeta_a\zeta_p + 4\beta^2\zeta_p^3\zeta_a + 4\beta^2\zeta_a^2\zeta_p^2 + \zeta_a\zeta_p + 4\zeta_a^2\zeta_p^2 + 4\zeta_p\zeta_a^3\end{array}} \tag{5.20}$$

Similarly, Eq. (5.17) is found to be,

$$I_{p2}=\frac{1}{2\pi}\frac{1}{2}\frac{\begin{array}{c}\zeta_a\pi(4\mu\beta^2\zeta_a^2\zeta_p+4\mu\beta^2\zeta_a\zeta_p^2+\mu^2\beta^4\zeta_p+\mu\beta^4\zeta_p+2\mu\beta^2\zeta_p\\ +4\beta^2\zeta_p^2\zeta_a+\mu\beta^4\zeta_a+4\zeta_a\zeta_p^2+4\zeta_p\zeta_a^2+4\beta^2\zeta_p^3+\beta^4\zeta_a+\zeta_p)\end{array}}{\begin{array}{c}\mu(2\mu\beta^2\zeta_a\zeta_p+\mu^2\beta^4\zeta_a\zeta_p+4\mu\beta^2\zeta_a^2\zeta_p^2+4\mu\beta^2\zeta_a^3\zeta_p-2\beta^2\zeta_p\zeta_a+\mu\beta^4\zeta_a^2\\ +\mu\beta^4\zeta_p^2+\beta^4\zeta_a\zeta_p+4\beta^2\zeta_p^3\zeta_a+4\beta^2\zeta_a^2\zeta_p^2+\zeta_a\zeta_p+4\zeta_a^2\zeta_p^2+4\zeta_p\zeta_a^3)\end{array}} \tag{5.21}$$

5.1.1.1 Undamped primary system

The special case where the primary structure is undamped is first considered. When $\zeta_p=0$, Eqs. (5.20) and (5.21) can be reduced to,

$$I_{p1}=0 \tag{5.22}$$

$$I_{p_2}=\frac{1}{4}\frac{\mu+1}{\mu^2} \tag{5.23}$$

Equation (5.22) is self-explanatory as no power is dissipated if the primary system is free of damping. Equation (5.23) indicates that the power dissipated by the absorber damper is constant. This is easy to understand from the energy balance point of view. When there exists no primary damping, the input power will be equal to the power dissipated by the absorber damping and since the excitation is assumed to be ideally white, the value of the dissipated power remains constant.

Even though the dissipated power by the primary damping is zero in this case, the mean square relative velocity of the primary mass is still investigated in order to find the optimum frequency tuning ratio β and damping ratio ζ_a to minimize the following objective function,

$$I_p=\frac{1}{2\pi}\int_{-\infty}^{\infty}|G|^2\,dr \tag{5.24}$$

In order to do that, the following conditions need to be satisfied,

$$\frac{\partial I_p}{\partial \beta} = 0$$
$$\frac{\partial I_p}{\partial \zeta_a} = 0 \tag{5.25}$$

which lead to,

$$\begin{aligned} &-4\mu\beta^3\zeta_a(2\mu\beta^2\zeta_a^2 + 4\zeta_a^2 - \beta^2 + 1) = 0 \\ &-\mu\beta^4(-2\mu\beta^2\zeta_a^2 - 4\zeta_a^2 + 1 + \mu\beta^4 - 2\beta^2 + \beta^4) = 0 \end{aligned} \tag{5.26}$$

The above equations yield,

$$(\mu^2 + \mu)\beta^6 + (2 - 2\mu)\beta^4 + (3\mu - 6)\beta^2 + 4 = 0 \tag{5.27}$$

$$\zeta_a = \sqrt{\frac{\beta^2 - 1}{2\mu\beta^2 + 4}} \quad (\beta > 1) \tag{5.28}$$

respectively. For Eq. (5.27) to have real positive roots, the following needs to be satisfied,

$$\Delta = 27\mu^5 + 72\mu^4 + 184\mu^3 + 87\mu^2 + 12\mu - 4 > 0 \tag{5.29}$$

which holds true only when $\mu < 0.15$.

Figure 5.1 shows the contour of I_p when $\mu = 0.05$. As it can be seen, no global minimum points exist. Eq. (5.28) is plotted as the black dashed curve in Figure 5.1 and the local minimum and maximum points are marked as '*' and 'o' on the line, respectively. The local minimum point has the corresponding tuning parameters of $\beta = 1.03$ and $\zeta_a = 0.12$. Table 5.1 lists the optimum values of β and ζ_a when μ ranges from 0.03 to 0.14.

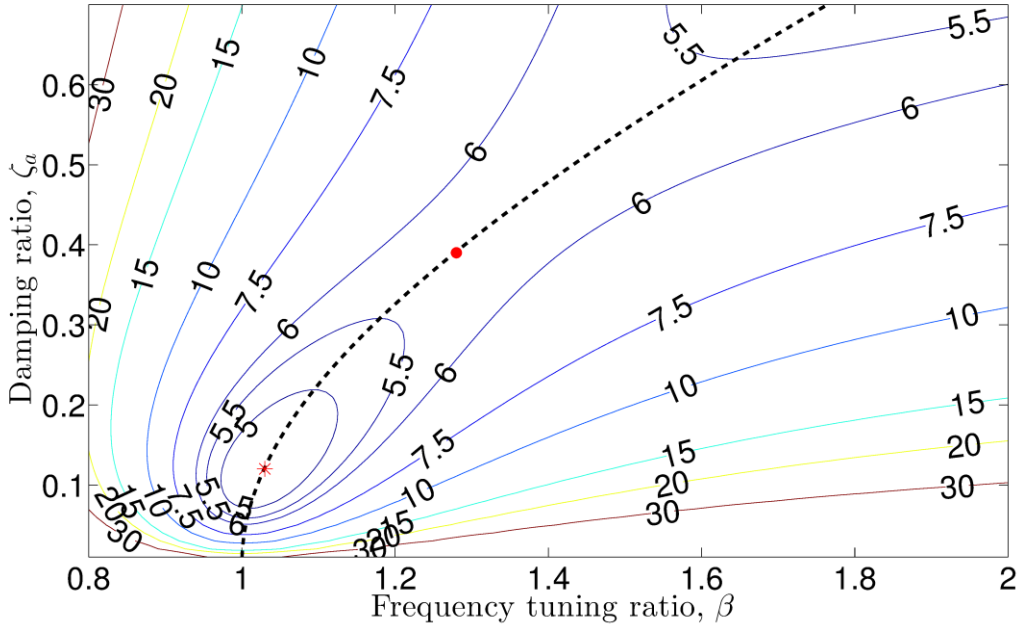

Figure 5.1. Contour of I_p when μ=0.05.

Table 5.1. Optimum values of β and ζ_a for undamped primary system

μ	β^{opt}	ζ_a^{opt}
0.03	1.016	0.090
0.04	1.022	0.105
0.05	1.028	0.119
0.06	1.035	0.132
0.07	1.042	0.145
0.08	1.051	0.158
0.09	1.060	0.171
0.10	1.069	0.184
0.11	1.081	0.199
0.12	1.095	0.215
0.13	1.113	0.235

0.14	1.146	0.268

Figure 5.2 shows the contour of I_p when $\mu = 0.18$. Since Eq. (5.29) is no longer satisfied, there exists no local minimum point.

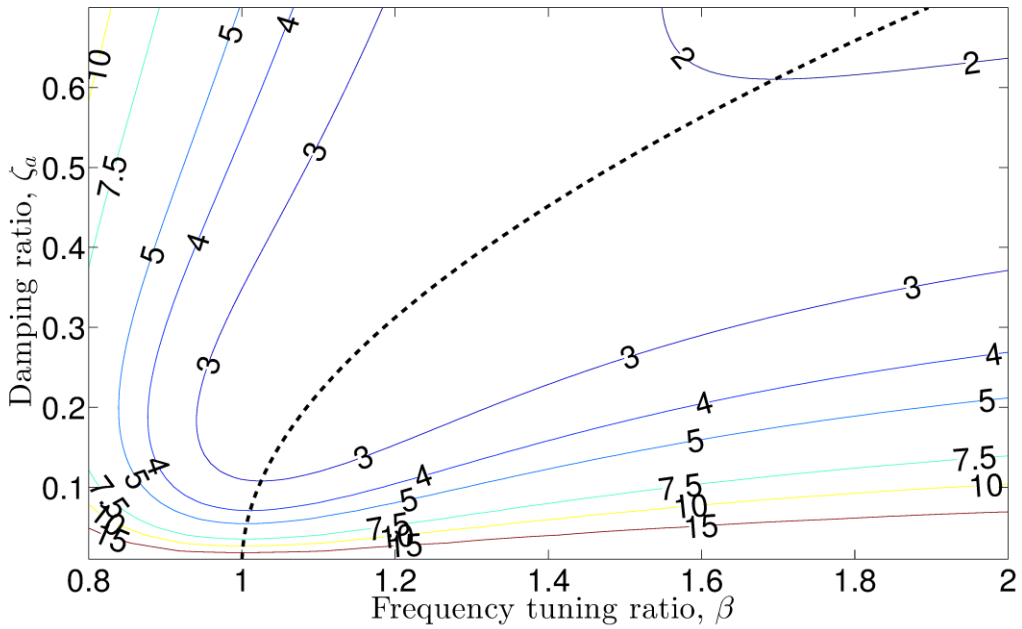

Figure 5.2. Contour of I_p when μ=0.18.

It is worth noting that the performance index under discussion here is the mean squared relative velocity of the primary mass instead of the absolute velocity. Thus the index $E[V^2]$ does not strictly represent the kinetic energy of the primary mass. A mathematical difficulty is encountered when investigating the kinetic energy of the primary mass. Here is a brief explanation.

The absolute velocity of the primary mass is found out to be,

$$V_{abs} = (j\omega)\bullet(X+Y)$$
$$= j\omega Y \frac{(kk_a - km_a\omega^2 - cc_a\omega^2) + j(kc_a\omega + k_a c_a\omega + k_a c\omega - cm_a\omega^3)}{(kk_a - km_a\omega^2 - k_a m_a\omega^2 - k_a m\omega^2 + mm_a\omega^4 - cc_a\omega^2) + j(c_a k_a\omega + c_a k\omega - c_a m\omega^3 + ck_a\omega - cm_a\omega^3)}$$

(5.30)

which can be normalized to be,

$$G_{abs} = \frac{V_{abs}}{\omega_p(\frac{m\omega^2 Y}{k})} = \frac{1}{r}\frac{2r(-\zeta_a - \mu\beta^2\zeta_a - \beta^2\zeta_p + \zeta_p r^2) + j(\beta^2 - r^2 - 4\zeta\zeta_a r^2)}{[(1-r^2)(\beta^2 - r^2) - (\mu\beta^2 + 4\zeta_p\zeta_a)r^2] + 2jr[(\beta^2 - r^2)\zeta_p + (1+\mu\beta^2 - r^2)\zeta_a]}$$

(5.31)

It is difficult to use the reference formula (Newland, 2012) to calculate the following integral,

$$E[V_{abs}^2] = S_0\int_{-\infty}^{\infty}\left|G_{abs}\right|^2 d\omega = \omega_p S_0\int_{-\infty}^{\infty}\left|G_{abs}\right|^2 dr \tag{5.32}$$

Thus the performance index for the primary kinetic energy is not investigated. Nevertheless, the index $E[V^2]$ is representative of the primary kinetic energy.

5.1.1.2 Damped primary system

In order to minimize the power dissipated by the primary damping and maximize the power dissipated by the absorber, the following conditions have to be satisfied,

$$\frac{\partial I_{p1}}{\partial\beta} = 0$$
$$\frac{\partial I_{p1}}{\partial\zeta_a} = 0 \tag{5.33}$$

$$\frac{\partial I_{p2}}{\partial \beta} = 0$$
$$\frac{\partial I_{p2}}{\partial \zeta_a} = 0 \tag{5.34}$$

Substituting Eq. (5.20) into Eq. (5.33) yields

$$\begin{aligned}&\mu\beta\zeta_p\zeta_a(-\zeta_p\zeta_a+\mu^2\beta^4\zeta_p^2-4\mu\beta^2\zeta_p\zeta_a^3+2\mu\beta^4\zeta_p\zeta_a+\beta^2\zeta_p\zeta_a-2\mu^2\beta^4\zeta_a^3\\&+2\mu^2\beta^4\zeta_p^3\zeta_a-2\beta^4\zeta_p\zeta_a^3+2\beta^4\zeta_p^3\zeta_a+2\mu\beta^4\zeta_p^4-4\zeta_p^2\zeta_a^2+\mu\beta^2\zeta_p^2-4\zeta_p\zeta_a^3\\&+4\mu\beta^2\zeta_p^3\zeta_a+\beta^4\zeta_a^2-2\mu\beta^4\zeta_a^4-\mu\beta^2\zeta_p\zeta_a-\beta^2\zeta_a^2-4\beta^2\zeta_a^4)=0\end{aligned} \tag{5.35}$$

$$\begin{aligned}&-\mu\beta^2\zeta_p(-24\mu\beta^2\zeta_p\zeta_a^3-4\beta^2\zeta_p^2\zeta_a^2-8\zeta_p^2\zeta_a^2-16\zeta_p\zeta_a^3-2\zeta_p^2\beta^4+\zeta_p^2\beta^2\\&-4\zeta_p^4\beta^2+8\beta^4\zeta_p^2\zeta_a^2-4\mu\beta^4\zeta_a^4+8\mu^2\beta^4\zeta_p^2\zeta_a^2+8\mu\beta^4\zeta_p\zeta_a^3+8\mu^2\beta^4\zeta_p^3\zeta_a\\&+8\mu\beta^2\zeta_p^3\zeta_a+8\beta^2\zeta_p\zeta_a^3+2\mu^2\beta^4\zeta_p^2-8\mu^2\beta^4\zeta_p\zeta_a^3+4\mu\beta^4\zeta_p^4+\mu\beta^2\zeta_p^2\\&+2\mu^2\beta^6\zeta_p\zeta_a+8\mu\beta^4\zeta_p^3\zeta_a+2\mu\beta^6\zeta_p\zeta_a+\mu\beta^6\zeta_a^2+\mu^3\beta^6\zeta_p^2+\mu^2\beta^6\zeta_p^2+\beta^6\zeta_a^2)=0\end{aligned} \tag{5.36}$$

Substituting Eq. (5.21) into Eq. (5.34) yields

$$\begin{aligned}&-\beta\zeta_p\zeta_a(-\zeta_p\zeta_a+\mu^2\beta^4\zeta_p^2-4\mu\beta^2\zeta_p\zeta_a^3+2\mu\beta^4\zeta_p\zeta_a+\beta^2\zeta_p\zeta_a-2\mu^2\beta^4\zeta_a^3\\&+2\mu^2\beta^4\zeta_p^3\zeta_a-2\beta^4\zeta_p\zeta_a^3+2\beta^4\zeta_p^3\zeta_a+2\mu\beta^4\zeta_p^4-4\zeta_p^2\zeta_a^2+\mu\beta^2\zeta_p^2-4\zeta_p\zeta_a^3\\&+4\mu\beta^2\zeta_p^3\zeta_a+\beta^4\zeta_a^2-2\mu\beta^4\zeta_a^4-\mu\beta^2\zeta_p\zeta_a-\beta^2\zeta_a^2-4\beta^2\zeta_a^4)=0\end{aligned} \tag{5.37}$$

$$\begin{aligned}&-\beta^2\zeta_p(-24\mu\beta^2\zeta_p\zeta_a^3-4\beta^2\zeta_p^2\zeta_a^2-8\zeta_p^2\zeta_a^2-16\zeta_p\zeta_a^3-2\zeta_p^2\beta^4+\zeta_p^2\beta^2\\&-4\zeta_p^4\beta^2+8\beta^4\zeta_p^2\zeta_a^2-4\mu\beta^4\zeta_a^4+8\mu^2\beta^4\zeta_p^2\zeta_a^2+8\mu\beta^4\zeta_p\zeta_a^3+8\mu^2\beta^4\zeta_p^3\zeta_a\\&+8\mu\beta^2\zeta_p^3\zeta_a+8\beta^2\zeta_p\zeta_a^3+2\mu^2\beta^4\zeta_p^2-8\mu^2\beta^4\zeta_p\zeta_a^3+4\mu\beta^4\zeta_p^4+\mu\beta^2\zeta_p^2\\&+2\mu^2\beta^6\zeta_p\zeta_a+8\mu\beta^4\zeta_p^3\zeta_a+2\mu\beta^6\zeta_p\zeta_a+\mu\beta^6\zeta_a^2+\mu^3\beta^6\zeta_p^2+\mu^2\beta^6\zeta_p^2+\beta^6\zeta_a^2)=0\end{aligned} \tag{5.38}$$

Comparing the above four equations, it can be seen that Eq. (5.37) is equivalent to Eq. (5.35) and Eq. (5.38) is to Eq. (5.36). This indicates that the minimization of the dissipated power by the primary damping and maximization of the power dissipated by the absorber both correspond to the same optimum value of β and ζ_a, provided that μ and ζ_p are not zero.

Equations (5.37) and (5.38) can be rewritten as

$$\begin{aligned}&(-2\zeta_a^3\zeta_p\mu^2+2\zeta_a\zeta_p\mu+2\zeta_p^4\mu+2\zeta_p^3\zeta_a\mu^2-2\zeta_a^3\zeta_p+2\zeta_p^3\zeta_a+\mu^2\zeta_p^2-2\zeta_a^4\mu+\zeta_p^2)\beta^4\\&+(-4\zeta_a^4-\zeta_a\zeta_p\mu+4\zeta_p^2\zeta_a^2-4\zeta_a^3\zeta_p\mu+\zeta_p^2\mu+4\zeta_p^3\zeta_a\mu-\zeta_a^2+\zeta_a\zeta_p)\beta^2\\&+(-4\zeta_a^3\zeta_p-4\zeta_p^2\zeta_a^2-\zeta_a\zeta_p)=0\end{aligned} \tag{5.39}$$

$$\begin{aligned}&(-4\beta^2-4\mu\beta^4)\zeta_a^4+(8\zeta_p\mu\beta^4-16\zeta_p-24\zeta_p\mu\beta^2+8\zeta_p\beta^2-8\zeta_p\mu^2\beta^4)\zeta_a^3\\&+(\beta^6+8\zeta_p^2\mu^2\beta^4+\mu\beta^6-8\zeta_p^2-2\beta^4+8\zeta_p^2\beta^4-4\zeta_p^2\beta^4+\beta^2)\zeta_a^2\\&+(2\zeta_p\mu\beta^6+8\zeta_p^3\mu\beta^2+8\zeta_p^3\mu^2\beta^4+2\zeta_p\mu^2\beta^6+8\zeta_p^3\mu\beta^4)\zeta_a\\&+(\zeta_p^2\mu^2\beta^6+4\zeta_p^4\mu\beta^4+\zeta_p^2\mu\beta^2+\zeta_p^2\mu^3\beta^6+2\zeta_p^2\mu^2\beta^4)=0\end{aligned} \tag{5.40}$$

Solving the above equations can be mathematically challenging. Hence a different approach is employed. Given the values of μ and ζ_p, a real positive β value can be obtained by solving Eq. (5.39) with a specific ζ_a value. By repeating this procedure, a set of data points $(\beta,\ \zeta_a)$ can be obtained and can be plotted into a curve which represents the relationship of these optimum parameters. Same for Eq. (5.40). With two curves available, the optimum value of β and ζ_a can be determined from the intersection point. Figure 5.3 shows the contour of I_{p1} when $\mu=0.05$ and $\zeta_p=0.05$. The purple and black curves correspond to Eqs. (5.39) and (5.40), respectively. These two curves intersect at two points: '*' represents the local minimum point and 'o' the local maximum.

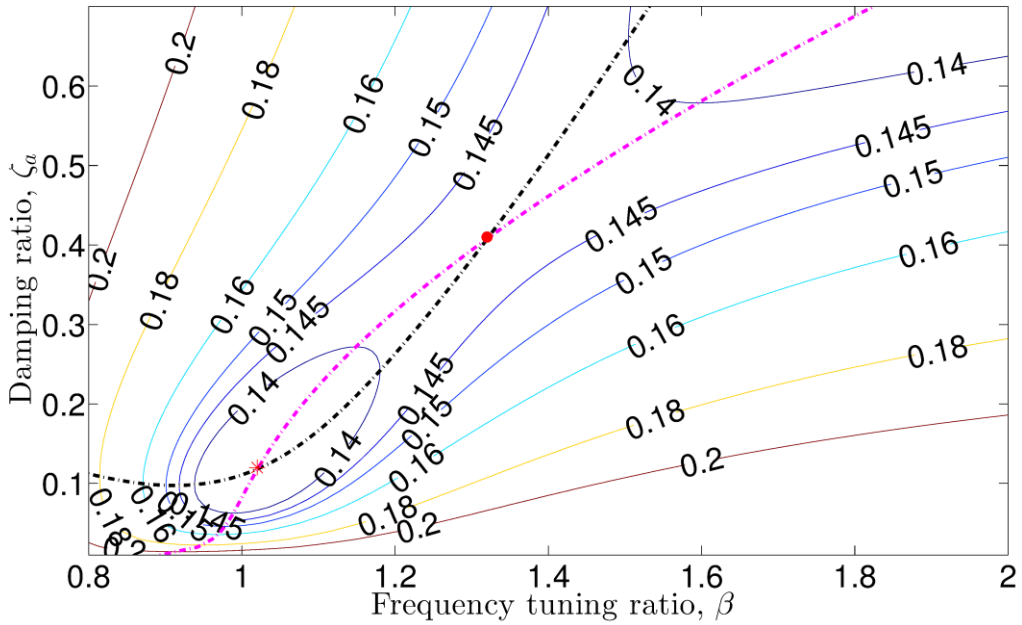

Figure 5.3. Contour of I_{p1} when μ=0.05 and ζ_p=0.05.

Figure 5.4 shows the contour of I_{p1} when $\mu = 0.15$ and $\zeta_p = 0.05$. As can be seen, the curves do not intersect. This is similar to the case with an undamped primary system where there exists no local minimum points when $\mu > 0.14$.

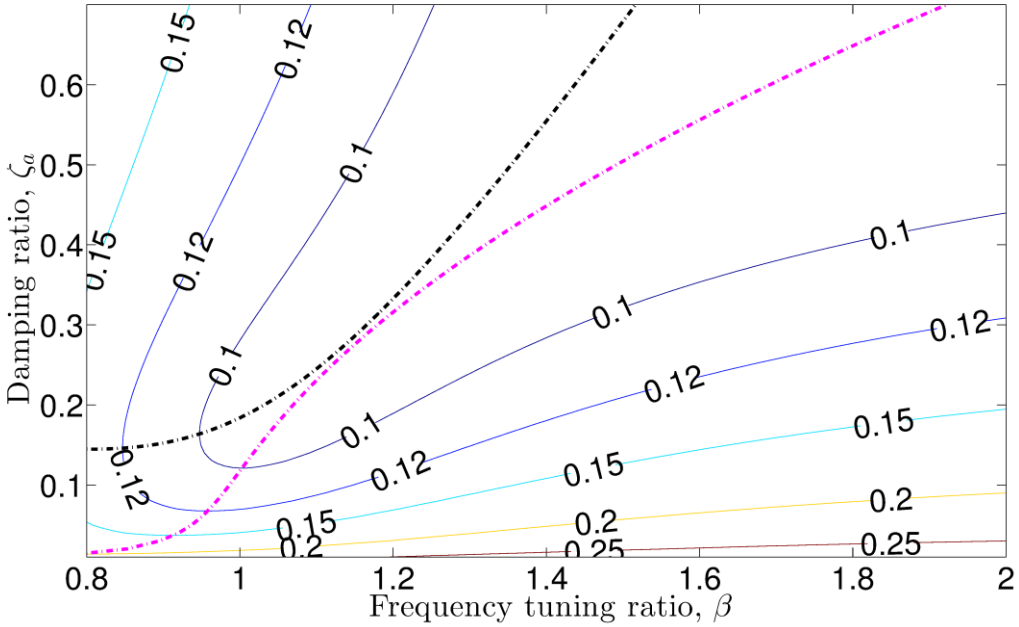

Figure 5.4. Contour of I_{p1} when μ=0.15 and ζ_p=0.05.

5.1.2 Discussion on the model B TMD with the electromagnetic damper

In this section, the dissipated power index I_{p3} and harvested power index I_{p4} are defined for a model B TMD equipped with an electromagnetic damper.

For the dissipated power:

$$I_{p3} = \frac{c_e E[V_a^{\,2}]}{4\pi S_0 k} = \frac{\mu \zeta_e}{2\pi} \int_{-\infty}^{\infty} |G_a|^2 \, dr \tag{5.41}$$

where,

$$\zeta_e = \frac{c_e}{2 m_a \omega_p} \tag{5.42}$$

For the sake of simplicity, the mechanical damping of the absorber is neglected. As the absorber damping consists entirely of electrical damping, I_{p3} has the same analytical form as I_{p2} with $\zeta_e = \zeta_a$. Recall Eq. (2.10), the electrical damping coefficient is defined as,

$$c_e = \frac{\Theta^2}{2R_{coil} + R_{load}} \tag{5.43}$$

where Θ is the transduction factor and is equal to 2.596 Tm for the electromagnetic damper used in this study, $2R_{coil}$ and R_{load} are the coil resistance and load resistance, respectively. I_{p3} varies with the frequency tuning ratio β and load resistance R_{load}. Equations (5.39) and (5.40) yield two curves which capture the relationship of β and R_{load}.

Given the relationship between the dissipated power and harvested power, the harvested power index is defined as,

$$I_{p4} = \frac{R_{load}}{R_{coil} + R_{load}} I_{p3} = \frac{R_{load}}{R_{coil} + R_{load}} \frac{\mu\zeta_e}{2\pi} \int_{-\infty}^{\infty} \left|G_a\right|^2 dr \tag{5.44}$$

Numerical investigations are conducted with the following system parameters: m = 0.34 kg and $f_p = 13.7$ Hz. For $\mu = 0.05$ and $\zeta_p = 0.05$, Figure 5.5 (a) shows the contour of I_{p3}. The maximum point is label in "*" and corresponds to a frequency tuning ratio of $\beta = 1.02$ and load resistance $R_{load} = 15\ \Omega$. This is the same as that found in Figure 5.3 where the maximum point represents the following: $\beta = 1.02$ and $\zeta_a = 0.12$.

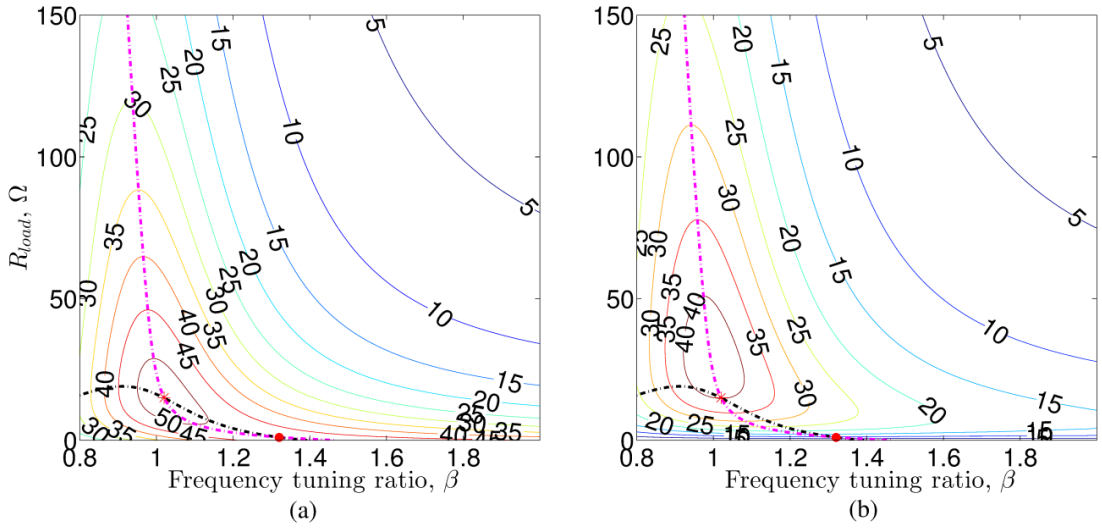

Figure 5.5. Contour of (a) I_{p3}; (b) I_{p4}, when μ=0.05 and ζ_p=0.05.

The contour of I_{p4} for $\mu = 0.05$ and $\zeta_p = 0.05$ is shown in Figure 5.5 (b) with the curves from Figure 5.5 (a). The curves are plotted as a reference to see the trade-off between vibration suppression and energy harvesting. From Figure 5.5 (b) it can be seen that the intersection point is located in the proximity of the points with high harvested power, which means that the trade-off situation is not significant as a satisfactory amount of the dissipated power and harvested power can be achieved at the same time with the given system parameters.

Figure 5.6 shows the contour of I_{p3} and I_{p4} for $\mu = 0.08$ and $\zeta_p = 0.05$. The intersection point is label in ‘’*” and corresponds to a frequency tuning ratio of $\beta = 1.05$ and load resistance $R_{load} = 4\,\Omega$. With a higher mass ratio, the system requires a higher absorber damping ratio, i.e. a lower load resistance, to achieve the greatest amount of the dissipated power. However, the intersection point which represents the optimum state for power dissipation only corresponds to a fair amount of the harvested power. The increase of mass ratio worsens the trade-off situation.

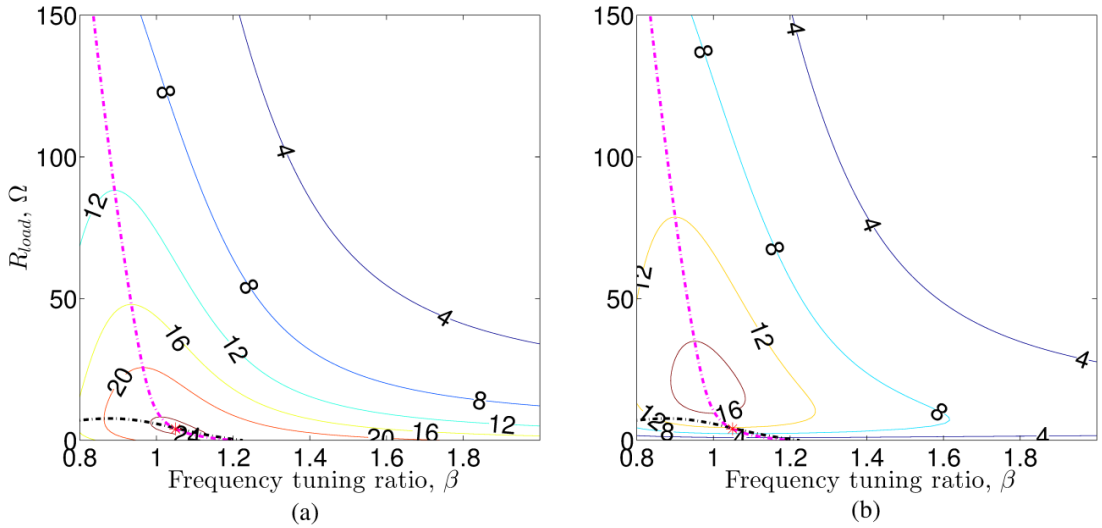

Figure 5.6. Contour of (a) I_{p3}; (b) I_{p4}, when μ=0.08 and ζ_p=0.05.

On the other hand, increase of the primary damping ratio has little effect on the trade-off situation. Figure 5.7 shows the contour of I_{p3} and I_{p4} for $\mu = 0.08$ and $\zeta_p = 0.15$. The intersection point in Figure 5.7 (a) corresponds to a tuning ratio of $\beta = 1.003$ and load resistance $R_{load} = 5\,\Omega$. With a larger primary damping ratio, the system requires a smaller frequency tuning ratio for the maximum amount of the dissipated power. The trade-off remains a moderate level as it can be seen from Figure 5.7 (b).

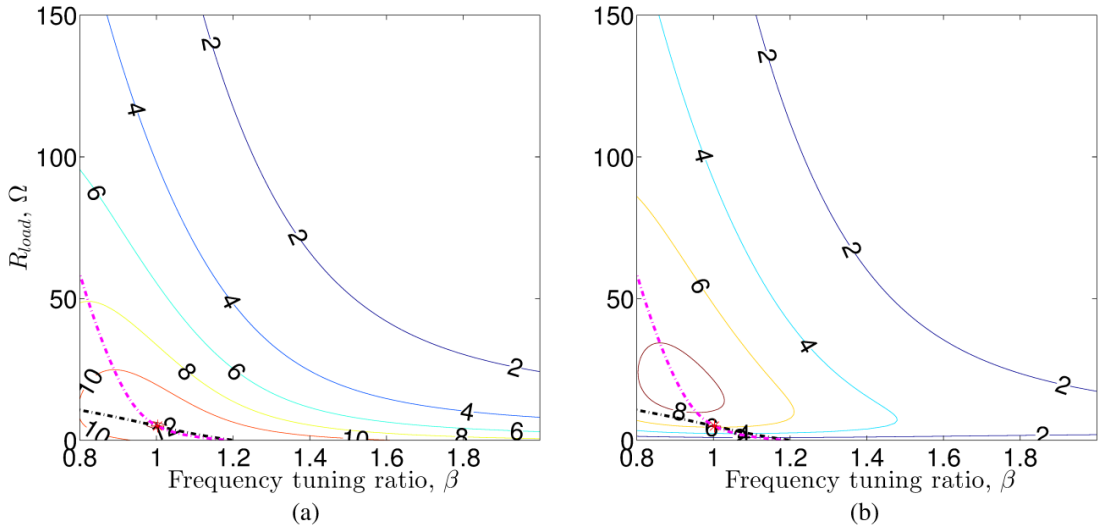

Figure 5.7. Contour of (a) I_{p3}; (b) I_{p4}, when μ=0.08 and ζ_p=0.15.

5.2 Simulation results with the band-limited white noise

Simulations are conducted to validate the results discussed above. The following parameters are used: m = 0.34 kg, $f_p = 13.7$ Hz and $\zeta_p = 0.05$. The ground motion is approximated by a band-limited white noise with a frequency range of 5 to 25 Hz. The mean squared relative velocities of the primary mass and absorber mass are calculated and the performance indexes are obtained using Eqs. (5.12) and (5.13) with an approximate spectral density of $S_0 = 8.98 \times 10^{-5}$ N^2s/rad. This spectral density value is calculated by averaging the squared magnitude of the Fourier Transform of the input over the time interval.

Figure 5.8 shows the contour of I_{p1} and I_{p2} when $\mu = 0.05$ and $\zeta_p = 0.05$. As it can be seen that the minimization of the power dissipated by the primary damping is equivalent to the maximization of the power dissipated by the absorber damping, and local minimum/maximum point exists as expected.

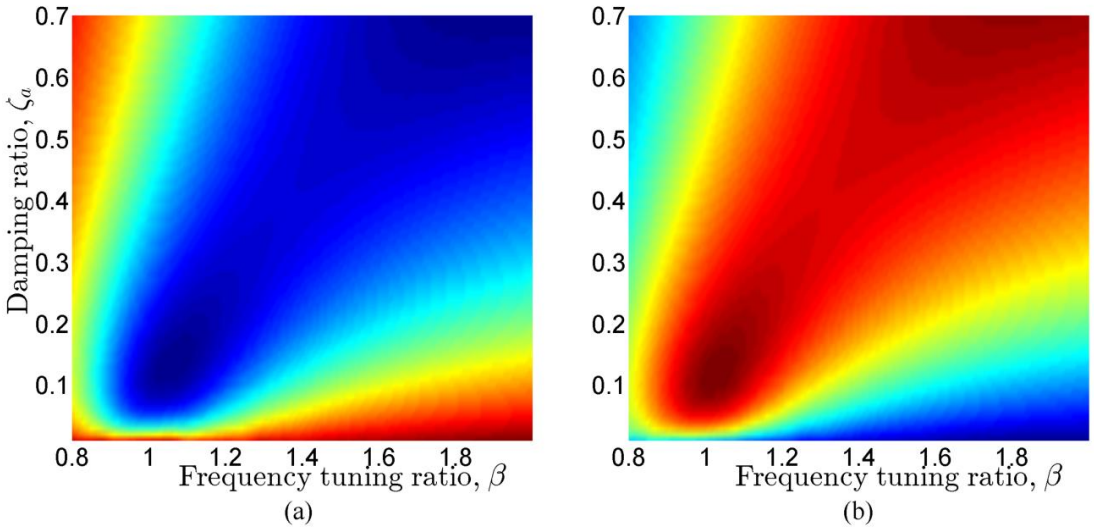

Figure 5.8. Contour of (a) I_{p1}; (b) I_{p2}, when μ=0.05 and ζ_p=0.05.

Figure 5.9 shows the contour of I_{p1} and I_{p2} when the mass ratio is increased to $\mu = 0.15$. The local maximum point does not exist anymore and the maximum dissipated power increases with increase of the frequency tuning ratio and damping ratio.

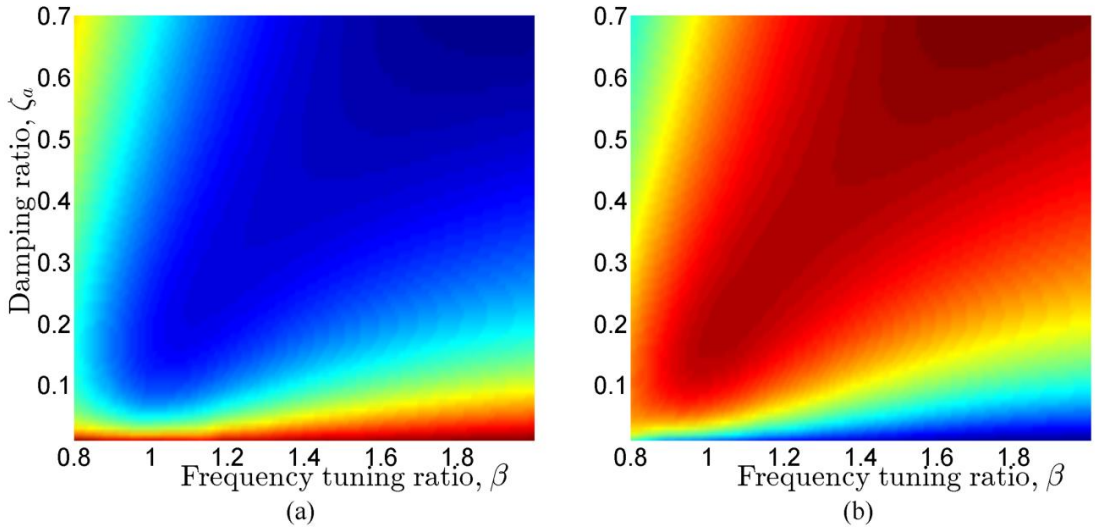

Figure 5.9. Contour of (a) I_{p1}; (b) I_{p2}, when μ=0.15 and ζ_p=0.05.

When the system is installed with an electro-magnetic damper, simulations are also conducted to investigate the relationship between the frequency tuning ratio β, load resistance R_{load} and the dissipated and harvested power. The mechanical damping of the absorber system is neglected. Figure 5.10 shows the contours of I_{p3} and I_{p4} when $\mu = 0.05$ and $\zeta_p = 0.05$. Compared with Figure 5.5, they show a good agreement with the analytical investigation.

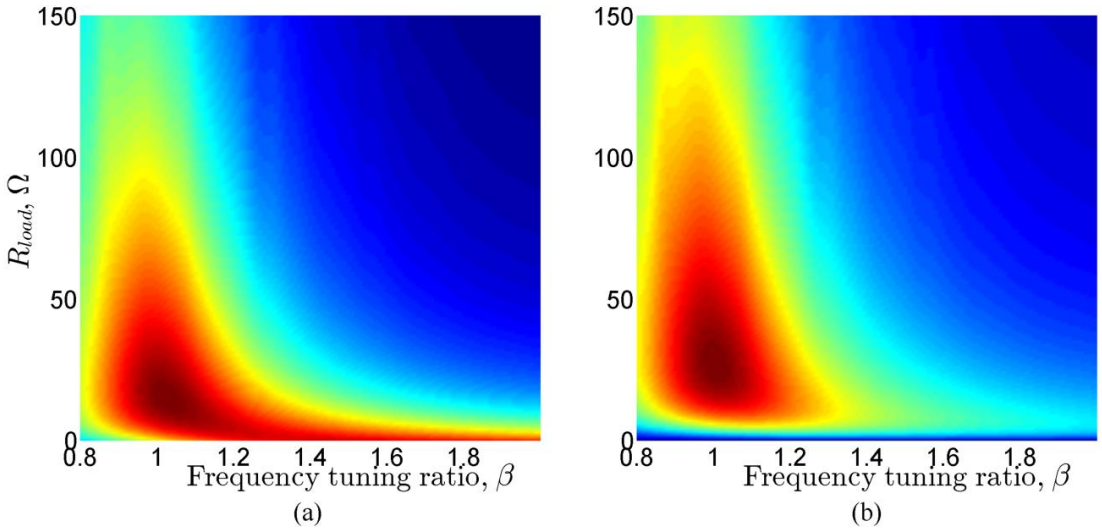

Figure 5.10. Contour of (a) I_{p3}; (b) I_{p4}, when μ=0.05 and ζ_p=0.05.

Figure 5.11 shows the contour of I_{p3} and I_{p4} when $\mu = 0.05$ and $\zeta_p = 0.15$. The increase of the primary damping has lowered the optimum tuning ratio value but barely affected the trade-off situation.

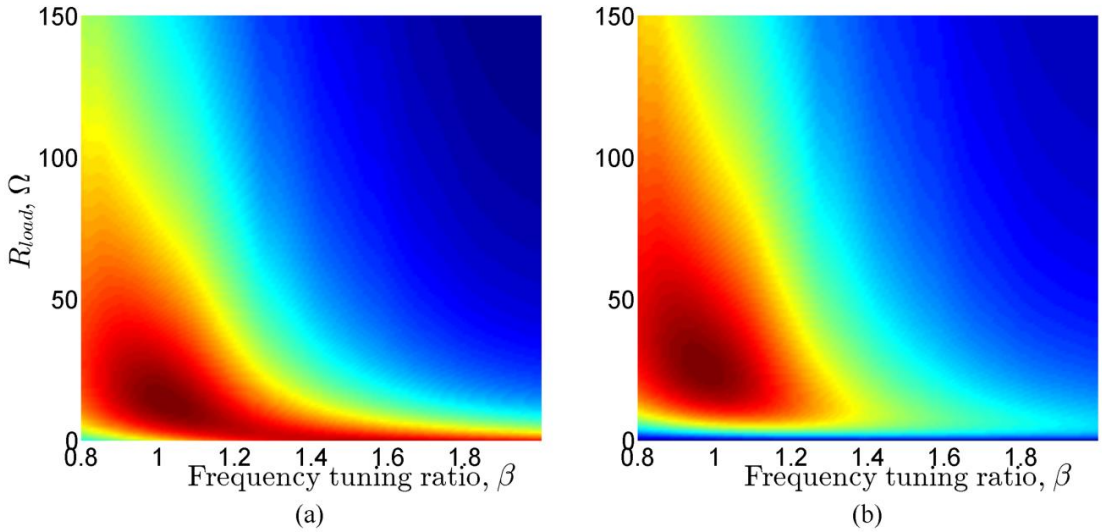

Figure 5.11. Contour of (a) I_{p3}; (b) I_{p4}, when μ=0.05 and ζ_p=0.15.

Figure 5.12 shows the contours of I_{p3} and I_{p4} when $\mu = 0.15$ and $\zeta_p = 0.15$. As predicted, the trade-off between the dissipated power and harvested power has become more significant with the increase of the mass ratio.

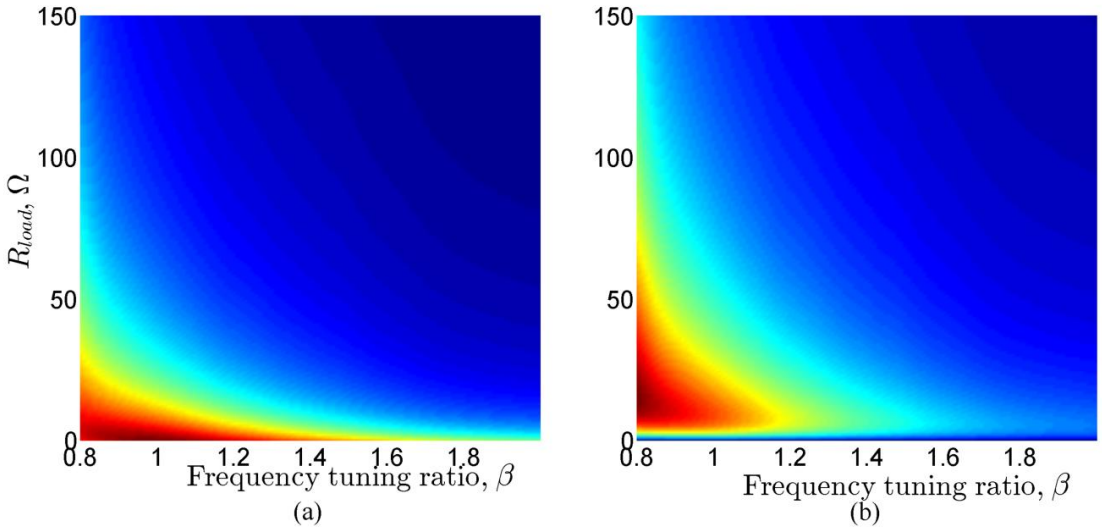

Figure 5.12. Contour of (a) I_{p3}; (b) I_{p4}, when μ=0.15 and ζ_p=0.15.

5.3 Experimental results

The experiment is conducted with the intention to show how the four performance criteria, i.e. $I_{p1,2,3,4}$ vary with different frequency tuning ratios and damping ratios/load resistances. In order to achieve a certain range of β and especially, ζ_a using the proposed electromagnetic damper, a different primary structure is used. The apparatus is shown in Figure 5.13. The identified system parameters are listed in Table 5.2.

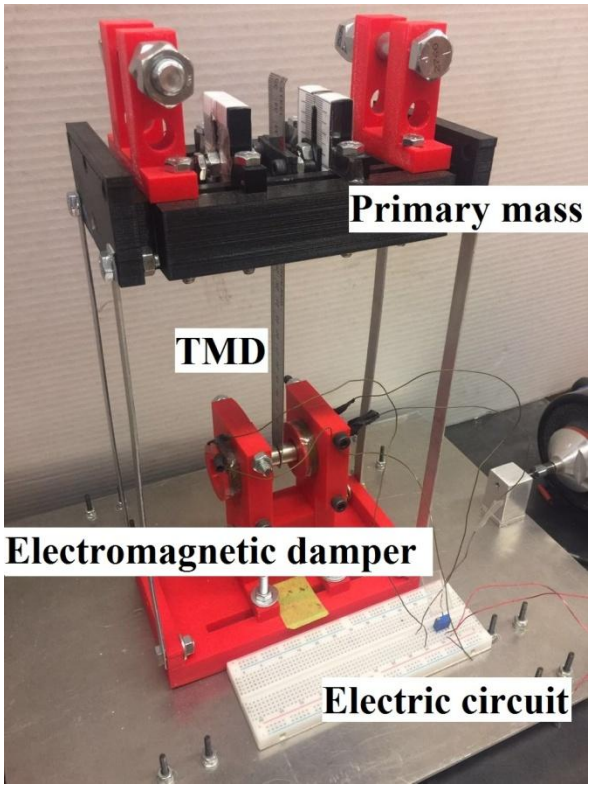

Figure 5.13. Photo of the experiment set-up.

Table 5.2. Identified system parameters

Primary mass	$m_p' = 0.697$ kg
Primary natural frequency	$f_p' = 5.2$ Hz
Primary stiffness	$k_p' = m_p'(2\pi f_p')^2 = 744.05$ N/m
Primary damping ratio	$\zeta_p' = 0.001$
Absorber mass	$m_a = 0.048$ kg

Table 5.3. The beam lengths vs. the frequency tuning ratios and the load resistances vs. the absorber damping ratios.

Beam length (mm)	β	Load resistance (Ω)	ζ_a
250	1.440	0.2	0.4476
255	1.347	2.5	0.3026
260	1.264	5	0.2238
265	1.189	7.5	0.1776

270	1.121	10	0.1472
275	1.059	12.5	0.1256
280	1.003	15	0.1096
285	0.952	17.5	0.0972
290	0.904	20	0.0873
295	0.861	22.5	0.0793
300	0.821	25	0.0726
305	0.784	30	0.0621
		35	0.0543
		40	0.0482
		50	0.0394
		75	0.0270
		100	0.0205
		200	0.0105

In order to achieve different frequency tuning ratios and damping ratios, the length of the absorber beam is adjusted from 250 mm to 305 mm with a 5 mm increment. At each length, the load resistance is varied from 0.2 Ω to 200 Ω. This yields a parameter range of $0.78 \le \beta \le 1.44$ and $0.01 \le \zeta_a \le 0.45$. When the system is tuned within this parameter range, random base motion is used to excite the system. The input signal is chosen as band-limited white noise with a range of 1 to 15 Hz. The natural frequencies of the combined system lie within the chosen frequency band so that the system dynamics can be fully excited. To obtain smoother results, 10 sets of random excitations are used and average values of the criteria are calculated. As shown in Figure 5.14, each set of excitation lasts 10 seconds followed by 10 seconds of interval. The base acceleration is calculated by differentiating the displacement twice

and the power spectral density of the base acceleration is calculated for 10 sets of excitation and the results are summed and averaged, resulting in an approximate spectral density of $S_0 = 1.5\times10^{-4}$ N^{2}s/rad.

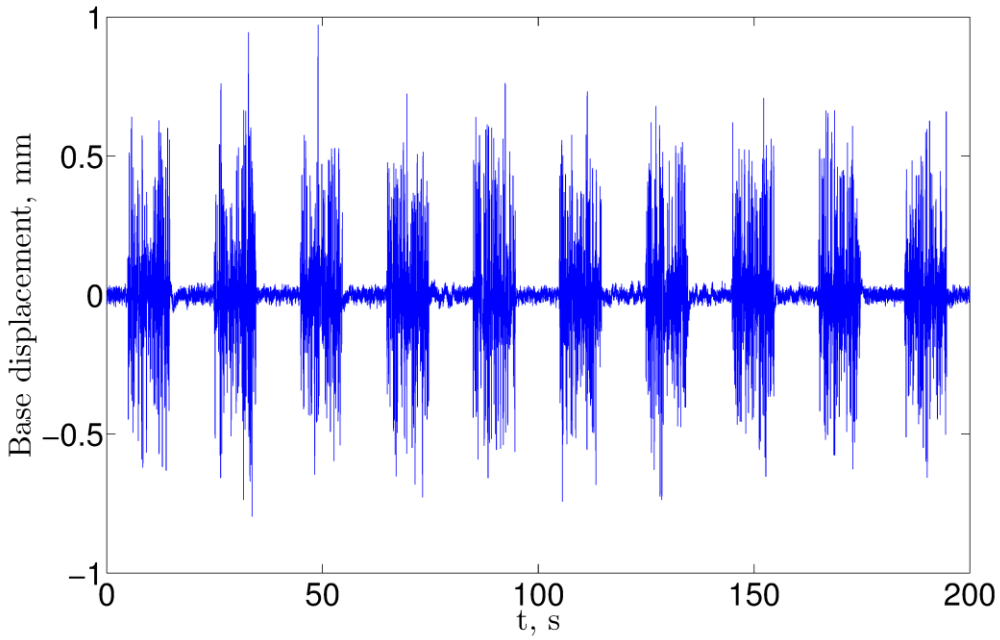

Figure 5.14. Base displacement for one set of random excitation

The displacements of the base, primary mass, and absorber mass are recorded as well as the voltage across the load resistance. The velocities of the base, primary mass, and absorber mass are then obtained by differentiating the displacement signal and the criteria are calculated using the following formulas

$$I_{p1} = \frac{c_p E[V^2]}{4\pi S_0 k_p} = \frac{c_p}{4\pi S_0 k_p}\frac{1}{T}\int_T V^2(t)dt \tag{5.45}$$

$$I_{p2} = \frac{c_a E[V_a^{\,2}]}{4\pi S_0 k_p} = \frac{c_a}{4\pi S_0 k_p}\frac{1}{T}\int_T V_a^{\,2}(t)dt \tag{5.46}$$

$$I_{p3} = \frac{c_e E[V_a^2]}{4\pi S_0 k_p} = \frac{c_e}{4\pi S_0 k_p} \frac{1}{T} \int_T V_a^2(t) dt \tag{5.47}$$

$$I_{p4} = \frac{R_{load}}{R_{coil} + R_{load}} I_{p3} \tag{5.48}$$

where T is the excitation period and $I_{p2} = I_{p3}$ as the mechanical damping of the absorber was neglected.

As the laser sensors are susceptible to noises which can introduce a significant error in the differentiation of displacement signal, the measured signal is first filtered by a low-pass filter with a cut-off frequency of 80 Hz. The filtered displacement signal is then interpolated using cubic spline approximation before numerical differentiation to obtain the velocity.

Figure 5.15 shows from both 3D and 2D perspectives how the power dissipated by the primary damping I_{p1} varies with the frequency tuning ratio β and the damping ratio ζ_a which is calculated from the load resistance. To better distinguish each curve, the line color is adjusted according to β value. The color of the lines changes from dark red to light yellow as the β value increases. For the red curves which correspond to a β value less than 1.2, as the damping ratio increases, I_{p1} decreases to the minimum point and then starts increasing. As β increases to 1.2, the increasing trend for I_{p1} with a further increase of damping ratio is lessened. When β exceeds 1.2, I_{p1} decreases monotonically with an increase of the damping ratio.

As a reference, simulations are also conducted using the identified system parameters. The system is under a ground motion of band-limited white noise (1 to 15 Hz) with an approximate power spectral density of $S_0 = 8.56 \times 10^{-5}$ N^{2}s/rad. The primary damping ratio is slightly increased to 0.5% as the quality of the simulation results deteriorates significantly and does not

show a clear pattern of the performance criterion when the primary damping ratio decreases to 0.1%. This measure of increasing the primary damping in simulation is justifiable as the simulation results are presented here to demonstrate the pattern of the performance criterion for reference purpose. The frequency tuning ratio β varies from 0.8 to 1.5 with an increment of 0.05 and the damping ratio ζ_a changes from 0.01 to 0.5. The simulation results of I_{p1} are presented in Figure 5.15 (c) and (d) in both 3D and 2D views. As it can be seen, both the experimental and simulation results share the same pattern that, with an increase of β, I_{p1} starts decreasing monotonically with an increase of ζ_a instead of reaching a minimum point first and then start increasing. The lowest I_{p1} value from the simulation is achieved when $\beta = 1.05$, shown as an orange-color curve. This value is close to the one obtained from the experiment which is $\beta = 1.003$ despite the slight excessive descending pattern.

Figure 5.16 shows how the dissipated power by the absorber damper I_{p2} is affected by the frequency tuning ratio β and damping ratio ζ_a. When β is smaller than 1.2, with an increase of the damping ratio, I_{p2} experiences a gradual increase before it decreases while when β is greater than 1.2, I_{p2} keeps growing with a larger value of the damping ratio. This is similar to the results obtained from the simulation which are shown in Figure 5.16 (c) and (d). Despite the slight non uniformity of the experimental results and its minor discrepancy with the simulation results, the experimental results are considered representative of the system behaviors. Comparison of subplots (a) and (b) of Figure 5.16 and those of Figure 5.15 also validates that the minimization of I_{p1} is equivalent to the maximization of I_{p2}.

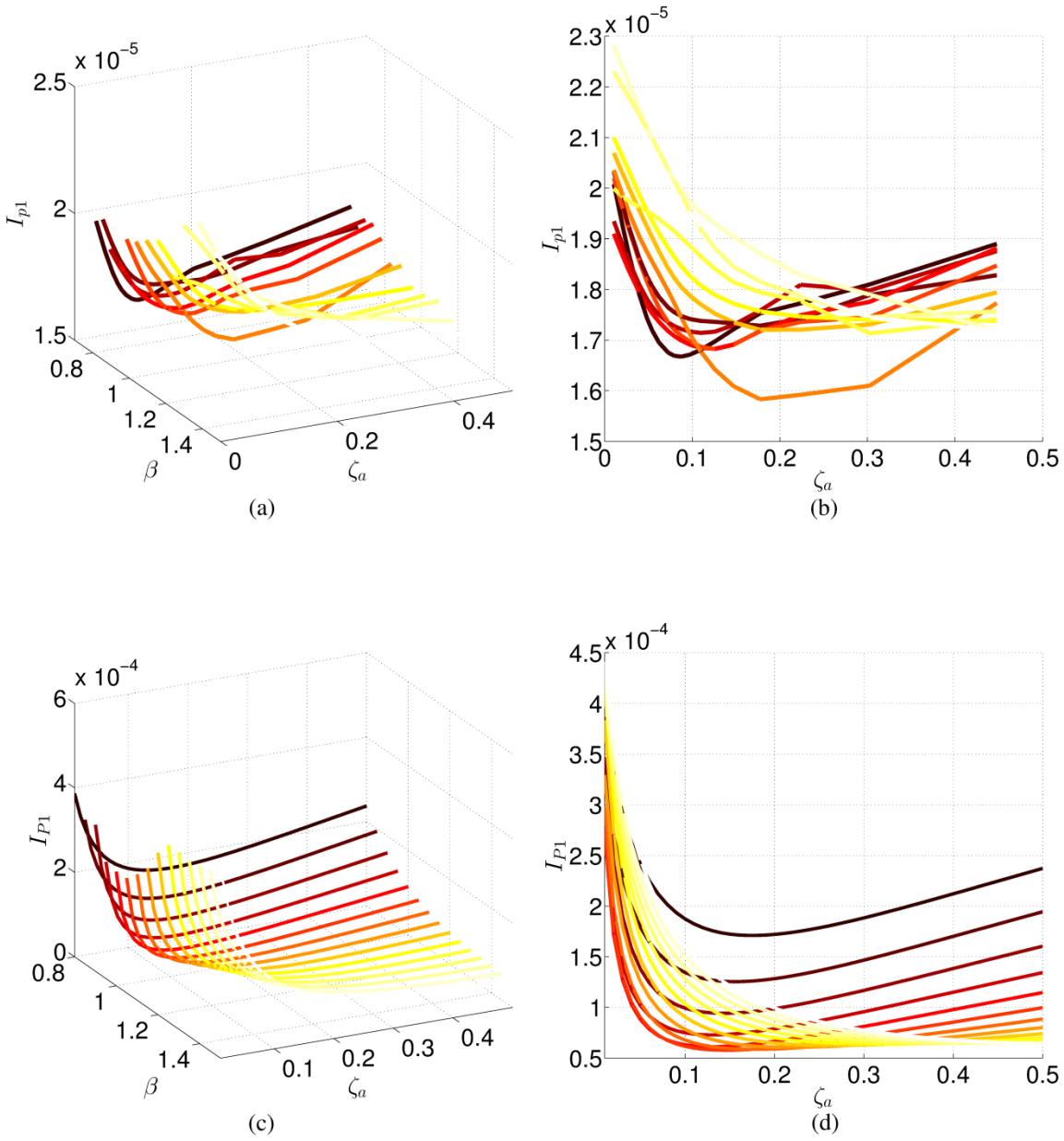

Figure 5.15. Experiment results of I_{p1} (a) 3D; (b) 2D; simulation results of I_{p1} (c) 3D; (d) 2D.

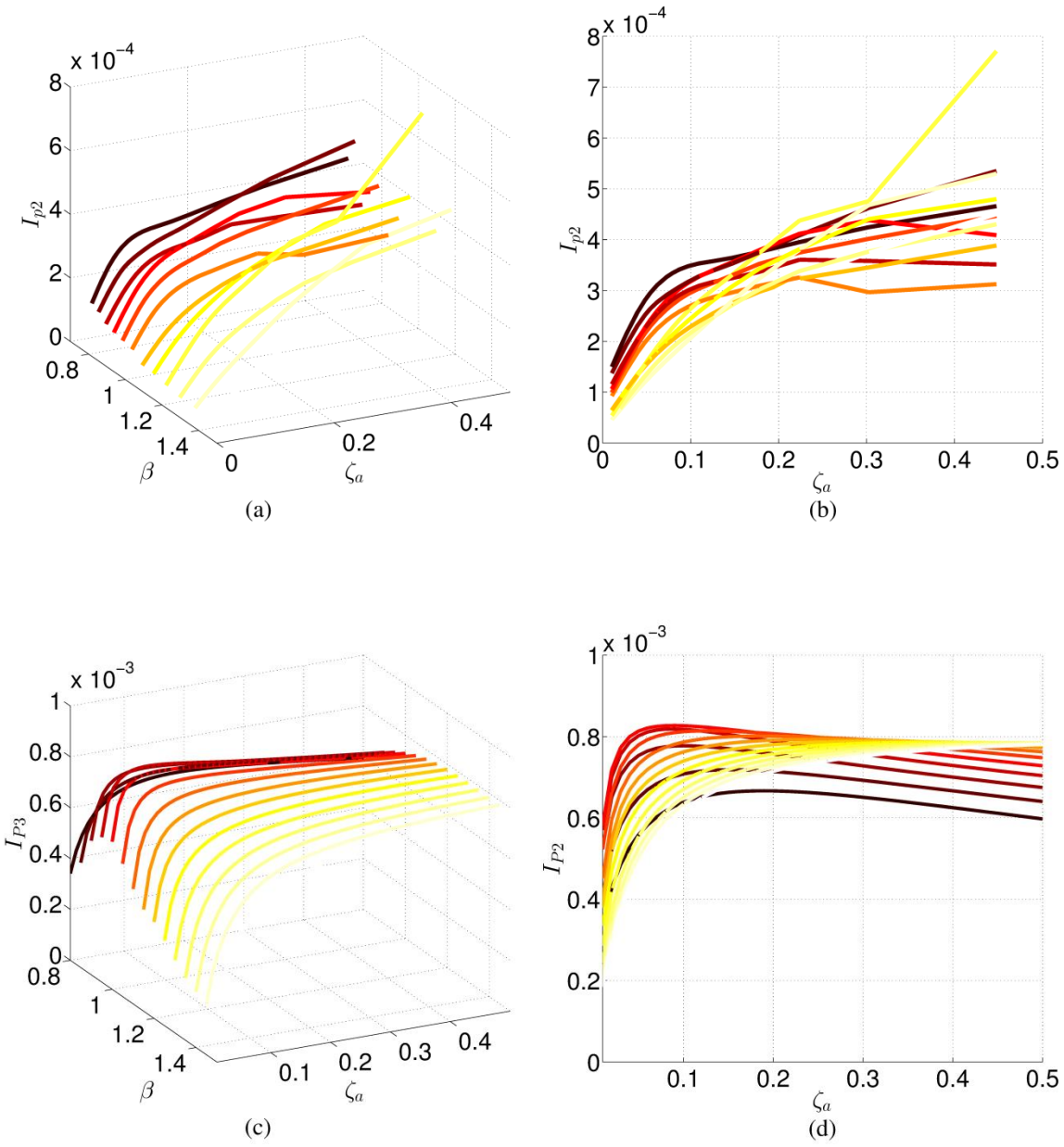

Figure 5.16. Experiment results of I_{p2} (a) 3D; (b) 2D; simulation results of I_{p2} (c) 3D; (d) 2D.

Figure 5.17 show the variation of I_{p3} with respect to the frequency tuning ratio β and load resistance R_{load}. As it can be seen, I_{p3} experiences different trends when the β value is smaller or greater than 1.2. Given consideration on all sources of the measurement errors and the discrepancy induced from the displacement differentiation, the experiment results are considered acceptable.

The harvested energy I_{p4} under different tuning ratios and load resistances is shown in Figure 5.18. As predicted in the previous discussion, under different frequency tuning conditions, the harvested energy peaks with a certain load resistance and decays with the increase of load resistance. Among the maximum points for each frequency tuning condition, the peak point at a β value near 1 has the greatest magnitude. Given a R_{load} value, I_{p4} increases as β approaches 1 and then starts decreasing with a greater β value.

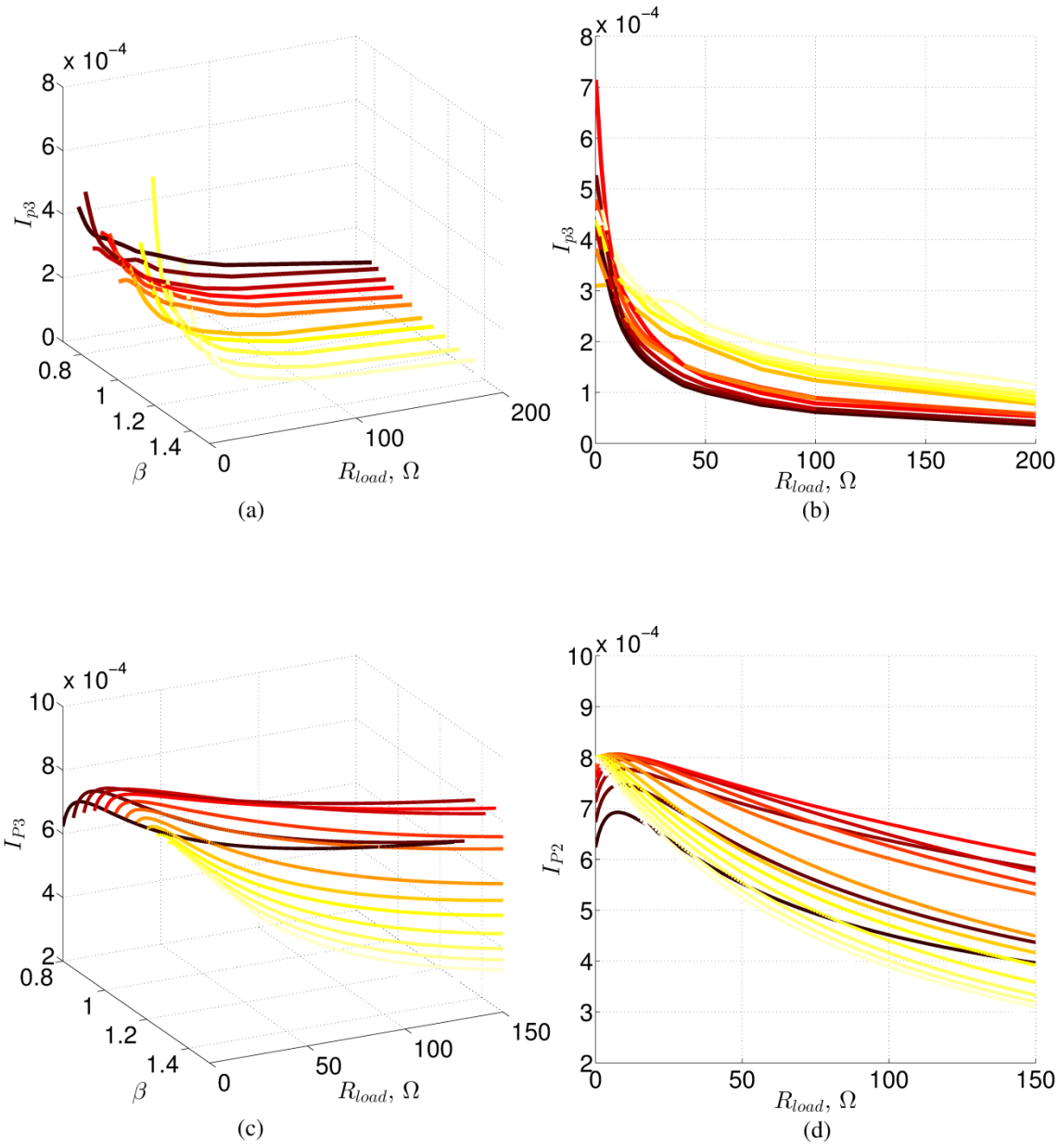

Figure 5.17. Experiment results of I_{p3} (a) 3D; (b) 2D; simulation results of I_{p3} (c) 3D; (d) 2D.

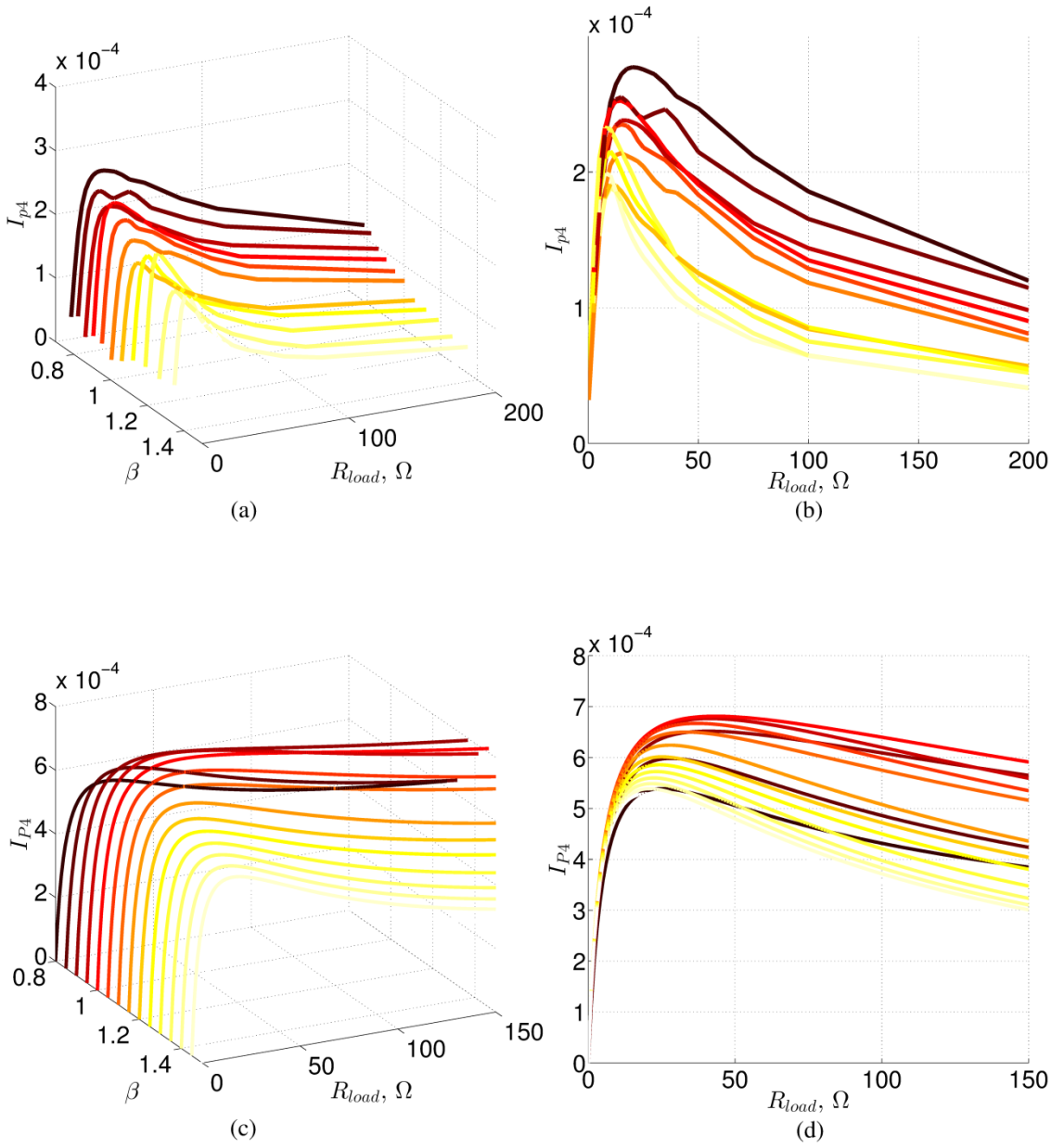

Figure 5.18. Experiment results of I_{p4} (a) 3D; (b) 2D; simulation results of I_{p4} (c) 3D; (d) 2D.

Chapter 6 Model B TMD in Multi-degree-of-freedom (MDOF) System

This chapter is dedicated to the investigation of a 2-DOF primary system with a model B TMD installed between the two main floors. The schematic of the system under consideration is shown in Figure 6.1. Due to the limitation of this study's scope, only simulation results are presented and the discussion on different tuning strategies are limited in depth. Based on the results in this chapter, future work can be intrigued for more detailed investigation.

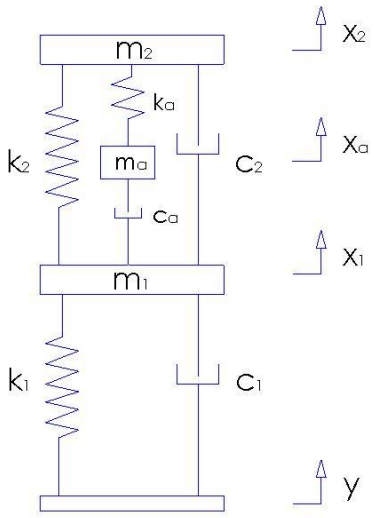

Figure 6.1. MDOF primary structure installed with a non-traditional vibration absorber.

6.1 Harmonic base excitation

6.1.1 Vibration suppression

When the above structure is under base excitation, the equation of motion can be written in the following matrix form,

$$\begin{bmatrix} m_1 & 0 & 0 \\ 0 & m_2 & 0 \\ 0 & 0 & m_a \end{bmatrix}\begin{bmatrix} \ddot{x}_1 \\ \ddot{x}_2 \\ \ddot{x}_a \end{bmatrix}+\begin{bmatrix} c_1+c_2+c_a & -c_2 & -c_a \\ -c_2 & c_2 & 0 \\ -c_a & 0 & c_a \end{bmatrix}\begin{bmatrix} \dot{x}_1 \\ \dot{x}_2 \\ \dot{x}_a \end{bmatrix}+\begin{bmatrix} k_1+k_2 & -k_2 & 0 \\ -k_2 & k_2+k_a & -k_a \\ 0 & -k_a & k_a \end{bmatrix}\begin{bmatrix} \ddot{x}_1 \\ \ddot{x}_2 \\ \ddot{x}_a \end{bmatrix}=\begin{bmatrix} -m_1\ddot{y} \\ -m_2\ddot{y} \\ -m_a\ddot{y} \end{bmatrix}$$

(6.1)

where m_1, m_2 and m_a are the masses for the first floor, the second floor and the absorber, respectively, k_1 , k_2 and k_a are the spring stiffness for the first floor, the second floor and the absorber, respectively, and c_1, c_2 and c_a are the damping coefficients for the first floor, the second floor and the absorber mass, respectively, y represents the base displacement, x_1, x_2 and x_a are the displacements of the first floor, the second floor and the absorber, each relative to the base displacement. The following variables are defined for the absorber system,

$$\omega_a=\sqrt{\frac{k_a}{m_a}},\ \beta_i=\frac{\omega_a}{\omega_{pi}},\ \zeta_{ai}=\frac{c_a}{2m_a\omega_{pi}} \tag{6.2}$$

ω_a is the natural frequency of the absorber system, ω_{pi} is the ith natural frequency of the primary structure, β_i is the frequency tuning ratio regarding the ith mode and ζ_{ai} is the damping ratio regarding the ith mode. Assume the base motion to be harmonic in the form of $y=Ye^{j\omega t}$ with ω representing the exciting frequency, the steady-state response of the displacements for the first floor, second floor, and the absorber mass can be written as

$$x_1=X_1e^{j\omega t},\ x_2=X_2e^{j\omega t},\ x_a=X_ae^{j\omega t} \tag{6.3}$$

where X_1, X_2 and X_a are the amplitudes of the displacement of the first floor, second floor, and the absorber mass, respectively. By substituting Eq. (6.3) and $y=Ye^{j\omega t}$ into Eq. (6.1) and performing matrix operation and the complex algebra, the displacement amplitudes of the two

floors and the absorber mass can be obtained. This can be accomplished through Maple program and the expressions for each displacement are not given here due to the length and complexity of the formulae (See Appendix A). Similar to Chapter 3, the displacement transmissibility ratios for each floor is defined as,

$$G_i = \frac{|X_i| k_i}{m_i \omega^2 Y},\ i = 1, 2 \tag{6.4}$$

To simplify the investigation, an undamped primary system is considered with the following system parameters: $m_1 = m_2 = 0.5$ kg , $k_1 = k_2 = 980$ N/m . The natural frequencies of the primary structure are found to be $f_{p1} = 4.35$ Hz and $f_{p2} = 11.40$ Hz . The first mode is to be suppressed with an absorber having the mass of $m_{a1} = 0.048$ kg . The subscript 1 means the absorber is designed to suppress the 1st mode of the primary structure. The natural frequency of the absorber is first set equal to the first natural frequency of the primary system, resulting in a frequency tuning ratio of $\beta_1 = 1.0$ and an absorber stiffness of $k_{a1} = 35.94$ N/m .

As the first mode is under suppression in which the second floor experiences the bigger vibration, the displacement transmissibility of the second floor of the primary system is plotted against the exciting frequency with different absorber damping ratio, as shown in Figure 6.2. The curve for the primary structure without the absorber is also shown in the figure for comparison. It can be seen that, similar to a SDOF primary system attached with an absorber, there exists two fixed points for a 2-DOF primary system with a vibration absorber under different absorber damping ratios.

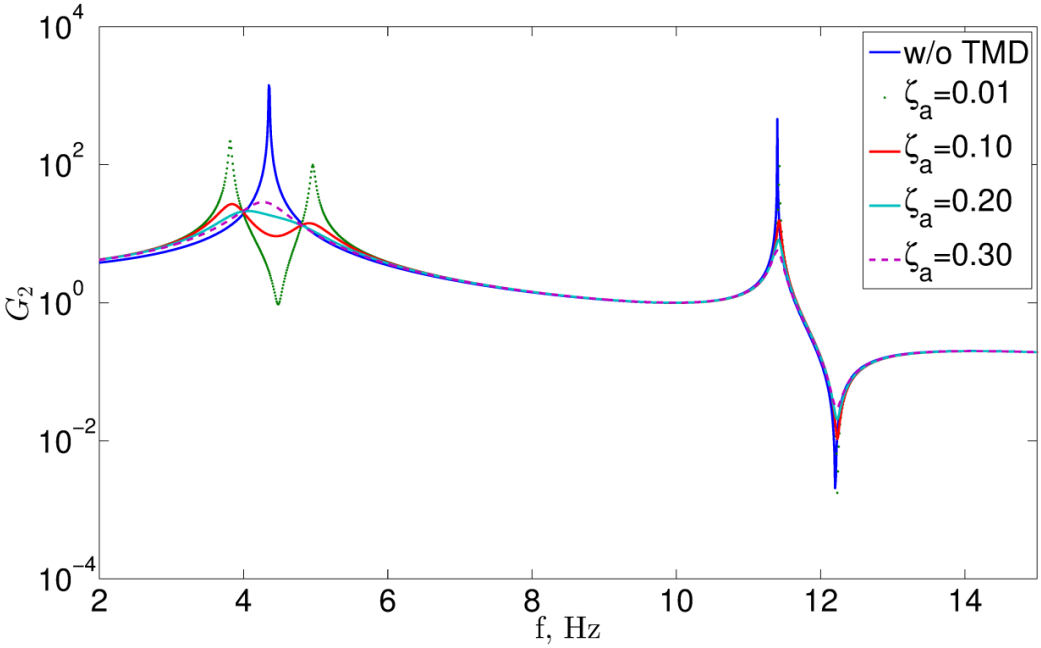

Figure 6.2. Displacement transmissibility ratio of the second floor.

The discovery and discussion on the two invariant points for MDOF primary system installed with a vibration absorber can be found in literature with a focus on the traditional vibration absorber (Chueng, Wong, & Cheng, 2015; Greco, Lucchini, & Marano, 2015; Nishimura, Yoshida, & Shimogo, 1989). One of the analytical methods to attack the problem of finding the optimum frequency tuning ratio and damping ratio is to employ the Sherman-Morrison matrix inversion formula (Ozer & Royston, 2004, 2005). However, this method is found to be not applicable to the case with a non-traditional vibration where the absorber damper is directly attached between the absorber mass and the floor below. Other researchers have also explored numerical methods with different performance criteria to find the optimum parameters for the system (Zuo & Nayfeh, 2002, 2004). To the best knowledge of the author, there has not been discussion on the optimization of MDOF system with a non-traditional absorber.

With the two 'fixed points', it would be natural to first apply the fixed-points theory of Den Hartog to find the optimum parameters. The performance index is the displacement

transmissibility of the second floor. Since the existence of the two fixed points is independent of the absorber damping, G_2 can be expressed in the following form,

$$G_2 = \sqrt{\frac{A_{m2}c_a^2 + B_{m2}}{C_{m2}c_a^2 + D_{m2}}} \tag{6.5}$$

The expressions of A_{m2}, B_{m2}, C_{m2} and D_{m2} are not given here due to their lengths (For reference, Appendix A gives the displacement magnitudes of the steady-state response of the primary mass and absorber mass). It is expected that if one follows the derivation for a SDOF system, which includes finding the abscissas of the fixed points, letting the two coordinates to be equal to find the optimum β_1, and finding the optimum damping ratio ζ_{a1} with Brock's approach, the optimum parameters for a MDOF system with a vibration absorber can be obtained. However, with multiple degrees of freedom in presence, the derivation loses its mathematical elegance and simplicity as for a SDOF system. Thus a numerical optimization method, Genetic Algorithm in MATLAB, is employed and combined with the 'fixed-points' theory. The process of finding the optimum parameters is shown below with the system parameters same as above.

Recalling Eq.(6.5), the abscissas of the two fixed points can be found after solving the following equation,

$$\frac{A_{m2}}{B_{m2}} = \frac{C_{m2}}{D_{m2}} \tag{6.6}$$

This yields a 4th order equation for ω^2 whose roots can be found using the 'root' function in MATLAB. The abscissas of the fixed points are calculated to be,

$$f_1 = 3.98 \text{ Hz}, f_2 = 4.80 \text{ Hz} \tag{6.7}$$

The optimum frequency tuning ratio β_1 is expected to be one that makes the coordinates of the two points equal. To achieve this, an objective function is defined as the absolute value of the difference between $G_2(f_1)$ and $G_2(f_2)$. Calculations are carried out through the range of $0.8 \le \beta_1 \le 1.2$ and the optimum β_1 is found to be,

$$\beta_1^{opt} = 0.9556 \tag{6.8}$$

with a 0.0032 difference in the two coordinates.

To find out the optimum damping ratio ζ_{a1}, it is required that the curve of G_2 passes through the two fixed points horizontally, which means the coordinates of the points are equal to that of the nearest natural frequency. A multi-objective optimization problem is defined and the objective functions are,

$$\begin{aligned} J_1(\zeta_{a1}) &= \left|G_2(f_1) - G_2(f_{c1})\right| \\ J_2(\zeta_{a1}) &= \left|G_2(f_2) - G_2(f_{c2})\right| \end{aligned} \tag{6.9}$$

where $f_{c1} = 3.73$ Hz and $f_{c2} = 4.84$ Hz are the first two natural frequencies of the combined system. After a certain amount of iterations, the following two damping ratios are found and each corresponds to the condition when,

$$\begin{aligned} (\zeta_{a1})_1 &= 0.1126,\ J_1(\zeta_{a1}) = 0.0001,\ J_2(\zeta_{a1}) = 1.7506 \\ (\zeta_{a1})_2 &= 0.1359,\ J_1(\zeta_{a1}) = 1.5380,\ J_2(\zeta_{a1}) = 0.0000 \end{aligned} \tag{6.10}$$

This is again similar to the derivation for an SDOF system where it is impossible for the curve to pass horizontally through the fixed points simultaneously. Hence, a convenient average value is used for the optimum damping ratio,

$$\zeta_{opt1} = \sqrt{\frac{(\zeta_{a1})_1^2 + (\zeta_{a1})_2^2}{2}} = 0.1248 \tag{6.11}$$

Figure 6.3 shows the displacement transmissibility for the second floor respectively under the optimum tuning ratio and different damping ratios including the optimum one.

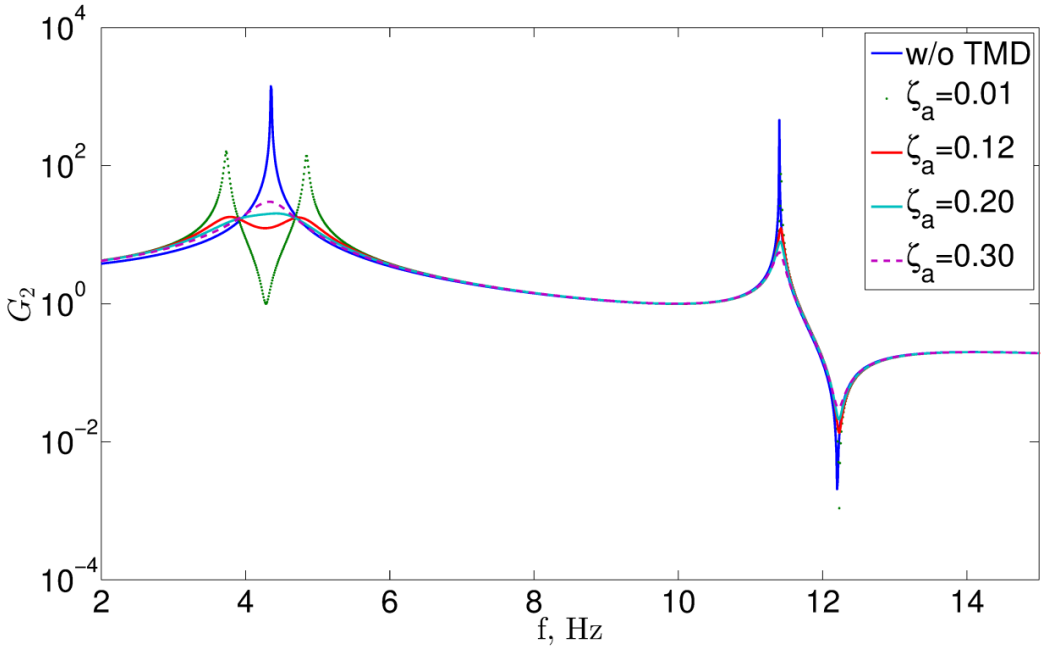

Figure 6.3. Displacement transmissibility of the second floor when β_1=0.9556.

The suppression of the second mode is also studied. The first floor experiences greater vibration when the second mode is suppressed. Figure 6.4 shows the displacement transmissibility of the first floor when the absorber is tuned using the second mode, i.e. $\beta_2 = 1.0$ and different damping ratios. One can also observes the two fixed points. The optimum tuning parameters for tuning the second mode can also be found using a similar procedure as discussed above.

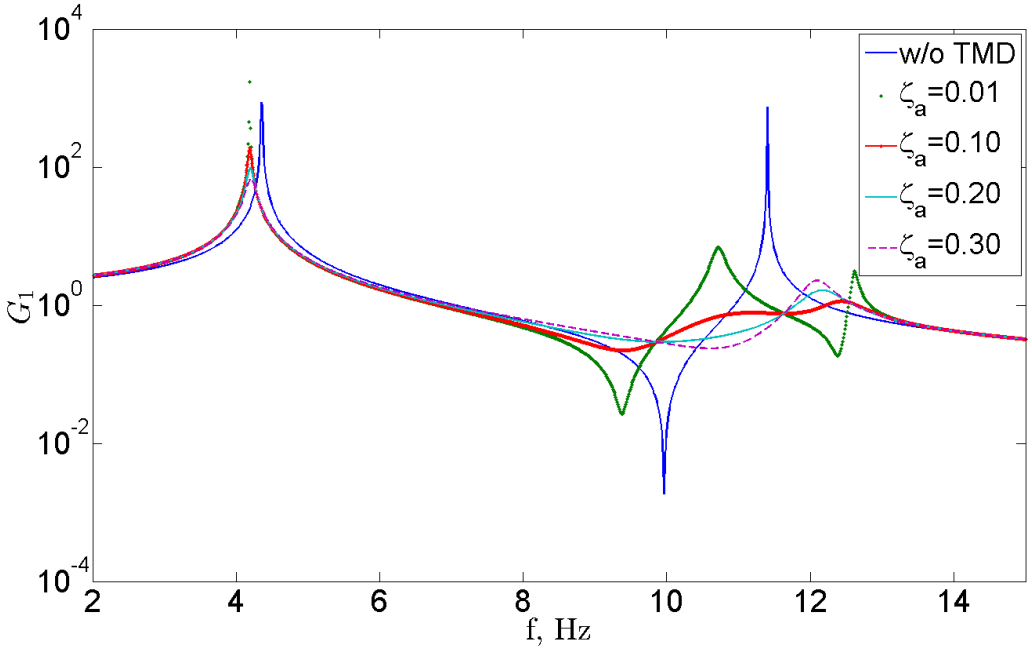

Figure 6.4. Displacement transmissibility of the first floor when β_2=1.0.

A second absorber is added with the same absorber mass $m_{a2} = m_{a1} = 0.048$ kg to enable tuning of both the modes. Figure 6.5 shows the schematic of such a configuration. Figure 6.6 show the displacement transmissibility for each floor when both the modes are under suppression with different damping ratios and $\beta_1 = 0.9556$ and $\beta_2 = 1.0$ .The suppression of the first mode appears to is compromised with addition of another vibration absorber installed between the first floor and the base to tune the second mode. Another interesting phenomenon to notice is that for G_1 there exist four fixed points near the second mode of the original system when both the absorbers are tuned to suppress both the modes, which invites more rigorous mathematical investigation. It should be noted that the existence of four fixed points has been mentioned in literature (Vakakis & Paipetis, 1986). The authors discussed the effect of a traditional vibration absorber on a linear 2DOF structure and the derivation suggested four fixed points in the plot of force transmissibility vs. the exciting frequency. The analytical model was simplified where the floor masses of the primary structure are equal to each other and so is the stiffness. However, the

method of attack is also only applicable to a traditional vibration absorber where an equivalent mass is used for the absorber system (Harris & Crede, 1976)

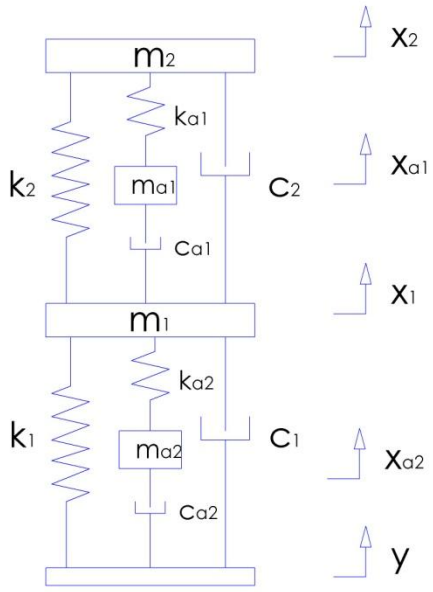

Figure 6.5. MDOF system with both modes tuned by vibration absorbers.

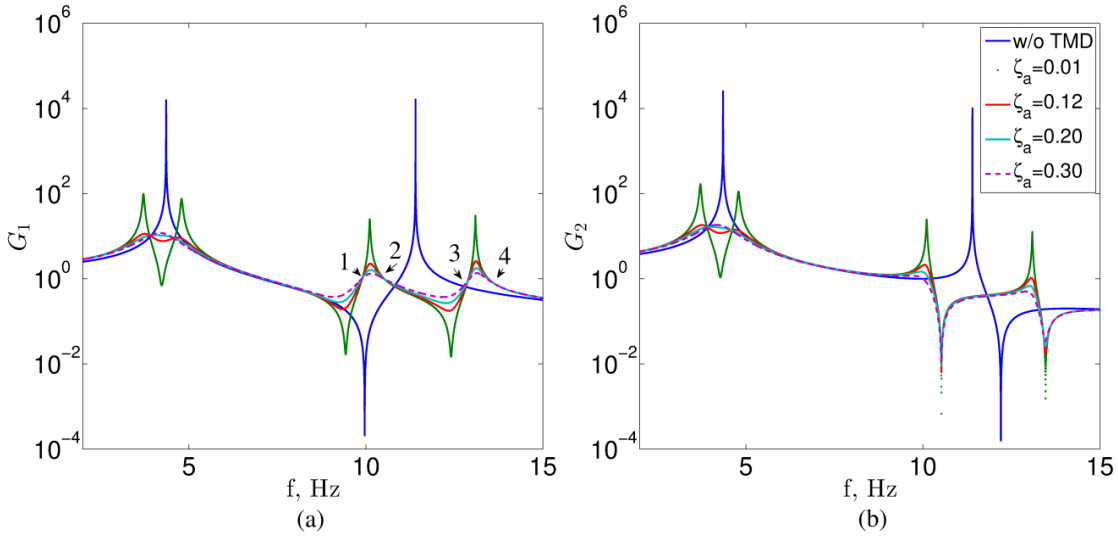

Figure 6.6. Displacement transmissibility of (a) the first floor; (b) the second floor, when β_1=0.9556 and β_2=1.0.

6.1.2 Energy harvesting

When an electromagnetic damper is used as the absorber damper, the energy harvesting efficiency is again brought to attention along with the vibration suppression. Following a similar process as that in Chapter 3, this subsection investigates two performance criteria regarding vibration suppression and energy harvesting.

For the system shown in Figure 6.1, with the vibration absorber tuned to suppress the first mode of the primary structure under harmonic base excitation, the instantaneous input power can be written as,

$$\begin{aligned} p_{in}(t) &= P_{in} e^{2j\omega t} \\ &= -m_1 \ddot{y}(t)[\dot{y}(t) + \dot{x}_1(t)] - m_2 \ddot{y}(t)[\dot{y}(t) + \dot{x}_2(t)] - m_a \ddot{y}(t)[\dot{y}(t) + \dot{x}_a(t)] \end{aligned} \tag{6.12}$$

where P_{in} is the amplitude of the input power. The instantaneous dissipated power can be written as,

$$p_e(t) = P_e e^{2j\omega t} = c_e[\dot{x}_a(t) - \dot{x}_1(t)]^2 = \frac{\Theta^2}{2R_{coil} + R_{load}}[\dot{x}_a(t) - \dot{x}_1(t)]^2 \tag{6.13}$$

where P_e is the amplitude of the dissipated power. The harvested power is given as,

$$p_{load}(t) = P_{load} e^{2j\omega t} = \frac{\Theta^2 R_{load}}{(2R_{coil} + R_{load})^2}[\dot{x}_a(t) - \dot{x}_1(t)]^2 \tag{6.14}$$

where P_{load} is the amplitude of the dissipated power. Two performance criteria are defined: the dissipated power ratio and the harvested power ratio with the same definition as in Chapter 3,

$$M_1 = \frac{P_e}{P_{in}} \tag{6.15}$$

$$M_2 = \frac{P_{load}}{P_{in}} \tag{6.16}$$

Simulations are conducted with the same system parameters as above, $m_1 = m_2 = 0.5$ kg, $k_1 = k_2 = 980$ N/m. The absorber has a mass of $m_{a1} = 0.048$ kg and is tuned with regard to the frequency tuning ratio. According to the previous discussion, $\beta_1^{opt} = 0.9556$. The natural frequencies of the combined system are found to be $f'_{p1} = 3.73$ Hz, $f'_{p2} = 4.84$ Hz and $f'_{p3} = 11.42$ Hz .The exciting frequency ranges from 1 to 15 Hz and the load resistance is adjusted between 1 to 100 Ω. Figure 6.7 shows the contour of the two performance criteria when no mechanical damping is considered.

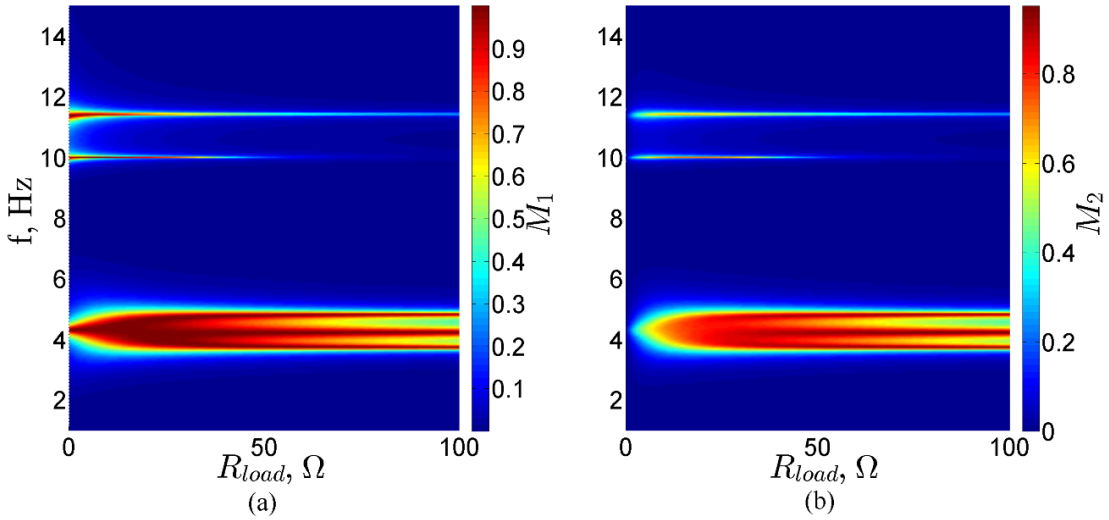

Figure 6.7. (a) Dissipated power ratio; (b) harvested power ratio, for MDOF system

The above figure presents a few interesting features. The highest dissipated power ratio is achieved when the exciting frequency is equal to the first natural frequency of the primary system at 4.35 Hz when the load resistance is low. As the load resistance increases, when the system is excited at its first two natural frequencies, the dissipated power ratio reaches the highest value. When the exciting frequency is equal to the third natural frequency, however, small dissipated power ratio is observed. A large amount of power is dissipated at two exciting

frequencies near the third natural frequency and the dissipated power decreases when the load resistance is increased. The harvested power ratio presented in Figure 6.7 (b) follows a similar pattern and it can be seen that the trade-off between vibration suppression and energy harvesting is not very significant.

After adding mechanical damping to the primary structure with $c_1 = 0.01 \bullet 2\sqrt{m_1 k_1} = 0.44$ Ns/m and $c_2 = 0.01 \bullet 2\sqrt{m_2 k_2} = 0.44$ Ns/m, the two performance criteria are again investigated and shown in Figure 6.8. Despite a similar pattern as with the undamped primary system, both the ratios have been reduced significantly at higher exciting frequencies. When the exciting frequency is near the first natural frequency of the system, the value of the dissipated power ratio decreases with an increasing load resistance. The harvested power ratio reaches the maximum point at certain load resistance near $25\ \Omega$.

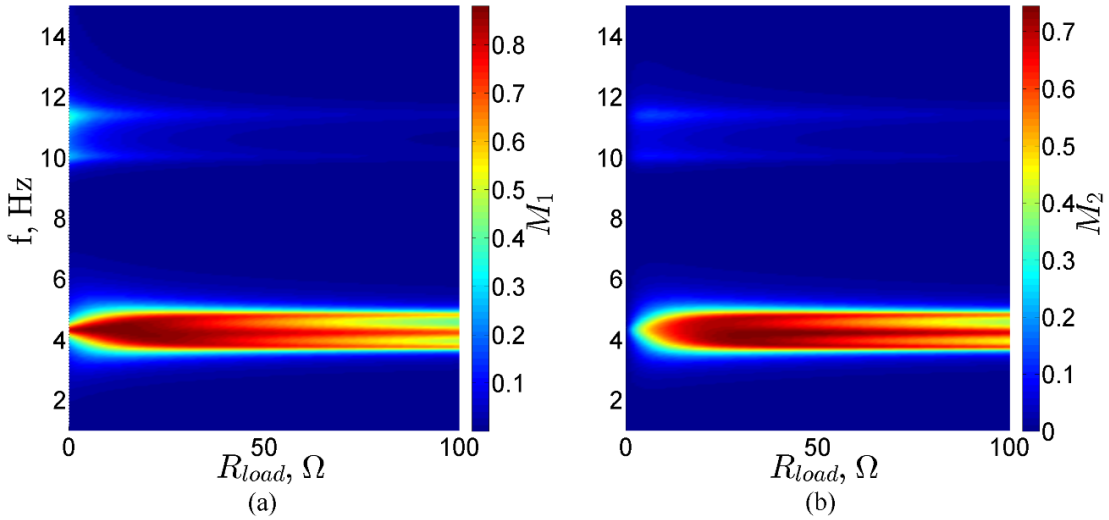

Figure 6.8. (a) Dissipated power ratio; (b) harvested power ratio, for MDOF system with mechanical damping

6.2 Random base excitation

This subsection considers the random base excitation. The non-traditional TMD is installed between the first floor and the second floor and the first mode of the primary system is to be suppressed. The previous defined performance criteria can also be defined,

$$I_{pc1} = \frac{c_1 E[V_1^2]}{4\pi S_0 k_1},\ I_{pc2} = \frac{c_2 E[V_2^2]}{4\pi S_0 k_2} \tag{6.17}$$

$$I_{p1} = I_{pc1} + I_{pc2} \tag{6.18}$$

$$I_{p2} = \frac{c_a E[(V_a - V_1)^2]}{4\pi S_0 k_a} \tag{6.19}$$

where V_1, V_2 and V_a are the relative velocity of the first floor, second floor and the absorber mass to the base motion, respectively, and S_0 is the spectral density of an ideally white input.

I_{pc1} represents the power dissipated by the damping of the first floor and I_{pc2} the second floor. The total dissipated power by the primary damping is defined to be I_{p1} which is summation of I_{pc1} and I_{pc2}. I_{p2} is the power dissipated by the absorber damping. When an electromagnetic damper is employed, I_{p2} can also be defined into,

$$I_{p3} = I_{p2} = \frac{c_e E[(V_a - V_1)^2]}{4\pi S_0 k_a} \tag{6.20}$$

if the mechanical damping of the absorber is neglected. Another performance criterion is defined as the harvested power by the absorber,

$$I_{p4} = \frac{R_{load}}{2R_{coil} + R_{load}} I_{p3} \tag{6.21}$$

Simulations are conducted on the system used in the previous section with the following parameters: $m_1 = m_2 = 0.5$ kg , $k_1 = k_2 = 980$ N/m , $c_1 = 0.01 \bullet 2\sqrt{m_1 k_1} = 0.44$ Ns/m and $c_2 = 0.01 \bullet 2\sqrt{m_2 k_2} = 0.44$ Ns/m. The absorber has a mass of $m_{a1} = 0.048$ kg. A band-limited white noise signal is used as the base excitation with a frequency range of 1 to 15 Hz. The spectral density is found out to be approximately 1.85×10^{-4}. The above performance criteria are calculated within the range of $0.8 \le \beta_1 \le 1.5$, $0.01 \le \zeta_{a1} \le 0.7$ and $0 \le R_{load} \le 100\ \Omega$.

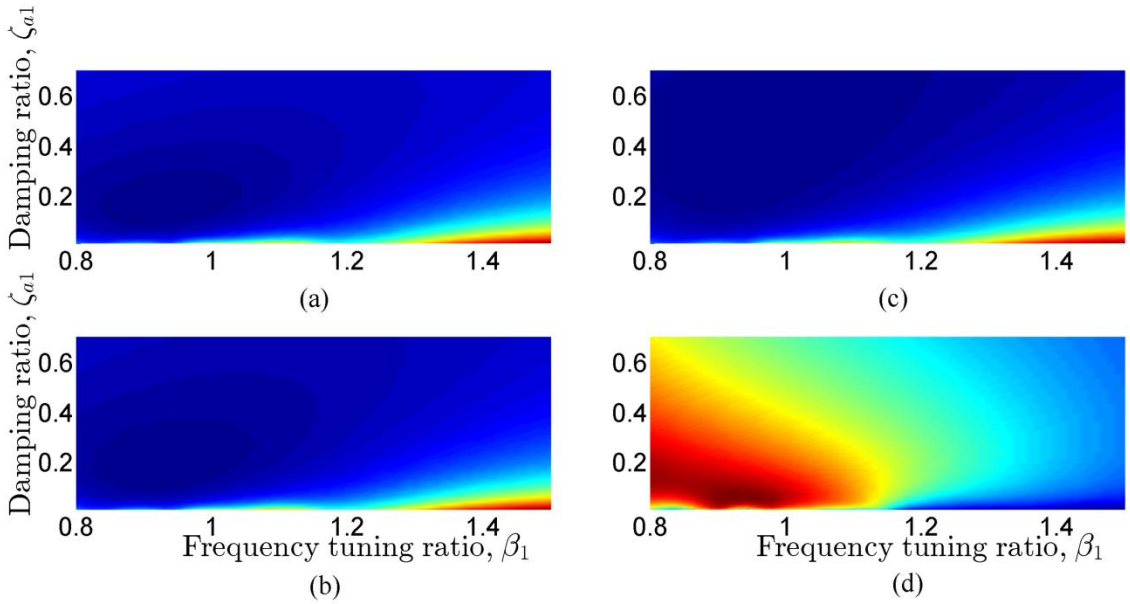

Figure 6.9. (a) I_{pc1}; (b) I_{pc2}; (c) I_{p1}; (d) I_{p2}.

Figure 6.9 shows the contour of the criteria of I_{pc1}, I_{pc2}, I_{p1} and I_{p2}. The minimum point of I_{pc1} corresponds to the tuning condition of $\beta_1 = 0.93$ and $\zeta_{a1} = 0.15$. When $\beta_1 = 0.94$ and $\zeta_{a1} = 0.32$, I_{pc2} reaches the lowest point. With the two criteria summed, in order for the primary damping to dissipate the minimum amount of power, β_1 needs to be set to 0.93 and ζ_{a1} 0.18. When $\beta_1 = 0.92$ and $\zeta_{a1} = 0.06$, I_{p2} has the largest value and the absorber dissipate the amount of power, achieving an optimum state of vibration suppression. Unlike in a SDOF primary system where the maximization of the dissipated power by the absorber is equivalent to the minimization of the dissipated power by the primary damping, it can be seen from Figure 6.9 (c) and (d) that this does not apply to the MDOF system.

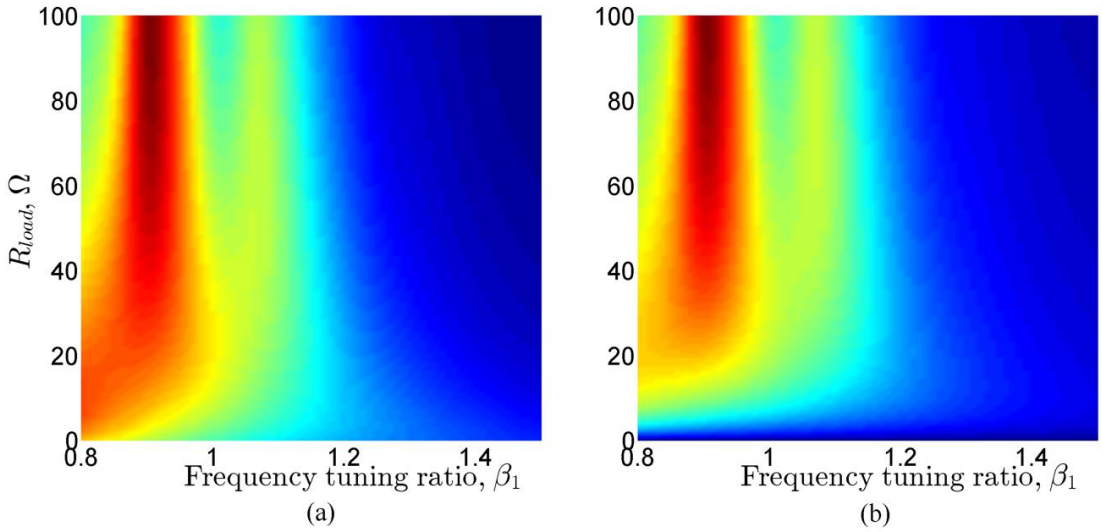

Figure 6.10. (a) I_{p3}; (b) I_{p4}.

Figure 6.10 shows the contour of I_{p3} and I_{p4} with regard to the frequency tuning ratio and load resistance. It reveals a trade-off situation between vibration suppression and energy harvesting which is far less severe than that in an SDOF system.

Chapter 7 Condition Assessment of Dynamic Vibration Absorber

This chapter presents a study conducted during the course of Master's thesis research. The majority contents of this thesis are dedicated to the investigation of an optimum model B TMD. While an optimally designed TMD can significantly suppress the structural vibration, de-tuning often occurs due to various reasons like change in operating conditions or variation in primary structure properties, resulting in degradation of TMD's performance. In order to restore its performance, it is necessary to estimate the modal properties of the primary structure and perform the re-tuning process. Such an exercise requires powerful signal processing methods to successfully extract the structural modes in presence of closely-spaced modes. In view of the advantages and limitations of existing modal identification methods, a new technique that combines the second-order blind identification (SOBI) method with the empirical wavelet transform (EWT) to delineate closely-spaced frequencies is proposed. While the SOBI method does not guarantee the separation of closely-spaced modes and suffers from the limitation of generating mixed modes, the EWT operates on the modal responses estimated by the SOBI and yields the closely-spaced natural frequencies.

The proposed method is illustrated using a six-storey simulation model with a wide range of de-tuning cases. An experiment on a three-storey bench-scale model equipped with a TMD is also conducted to validate the applicability of the proposed method. Before the simulation and experiment results are presented, a brief introduction on each involved identification method is provided followed by the explanation of the proposed method. In order to avoid an overlapping use of the frequency symbol *f*, the symbol ω is used in this chapter to represent frequency.

7.1 Background

7.1.1 Second-order blind identification (SOBI)

A brief explanation of the SOBI is presented in this subsection. Consider a linear, classically damped and lumped-parameter *n*DOF system subjected to an external force $\boldsymbol{F}$(t) with the equation of motion defined as,

$$\boldsymbol{M}\ddot{\boldsymbol{X}}(t)+\boldsymbol{C}\dot{\boldsymbol{X}}(t)+\boldsymbol{K}\boldsymbol{X}(t)=\boldsymbol{F}(t) \tag{7.1}$$

where $\boldsymbol{X}$(t) is the displacement vector, $\boldsymbol{M}$, $\boldsymbol{C}$, $\boldsymbol{K}$ are the mass, damping and stiffness matrix, respectively. When $\boldsymbol{F}$(t) is assumed to be Gaussian and broadband, the response of the system can be expressed in terms of vibration modes superposition with the following form,

$$\boldsymbol{X}_{n\times N}=\boldsymbol{\Psi}_{n\times n}\times\boldsymbol{q}_{n\times N} \tag{7.2}$$

where $\boldsymbol{\Psi}$ is the mode shape matrix and $\boldsymbol{q}$ is the matrix of modal coordinated which gives the information about natural frequencies of the structure. Comparing to the problem statement of the BBS, which is given by,

$$\begin{aligned}\boldsymbol{x}(k)&=\boldsymbol{A}\boldsymbol{s}(k)\\ \boldsymbol{y}(k)&=\boldsymbol{W}\boldsymbol{x}(k)\end{aligned} \tag{7.3}$$

Where $\boldsymbol{A}_{n\times N}$ is the instantaneous mixing matrix, $\boldsymbol{W}_{n\times n}$ is the un-mixing matrix to be determined and $\boldsymbol{y}$ is the estimate of the source $\boldsymbol{s}$(k), it is easy to recognize the similarity: the modes of the system represent the independent sources and the modal coordinates are contained in the mixing matrix.

The basic framework of SOBI is the simultaneous diagonalization of two covariance matrices $\boldsymbol{T}_X(0)$ and $\boldsymbol{T}_X(p)$ evaluated at the time-lag zero and *p*, respectively. This can be written as (Belouchrani, Abed-Meraim, Cardoso, & Moulines, 1997),

$$\begin{aligned}\boldsymbol{T}_X(0) &= E\{\boldsymbol{X}(n)\boldsymbol{X}^T(n)\} = \boldsymbol{A}\boldsymbol{T}_s(0)\boldsymbol{A}^T \\ \boldsymbol{T}_X(p) &= E\{\boldsymbol{X}(n)\boldsymbol{X}^T(n-p)\} = \boldsymbol{A}\boldsymbol{T}_s(p)\boldsymbol{A}^T\end{aligned} \tag{7.4}$$

where,

$$\boldsymbol{T}_s(p) = E\{\boldsymbol{s}(n)\boldsymbol{s}^T(n-p)\} \tag{7.5}$$

The signal ***X***(t) is first whitened with a whitening matrix $\boldsymbol{Q}_{n\times N}$ expressed as,

$$\bar{\boldsymbol{X}}(t) = \boldsymbol{Q}\boldsymbol{X}(n) = \boldsymbol{\Lambda}_X^{-\frac{1}{2}}\boldsymbol{V}_X^T\boldsymbol{X}(n) \tag{7.6}$$

where $\boldsymbol{\Lambda}_X$ and $\boldsymbol{V}_X$ are the eigenvalues and eigenvectors of the covariance matrix $\boldsymbol{T}_X(0)$, respectively. The whitened covariance matrix $\boldsymbol{T}_{\bar{X}}(p)$ is defined as,

$$\boldsymbol{T}_{\bar{X}}(p) = \boldsymbol{Q}\boldsymbol{A}\boldsymbol{T}_{\boldsymbol{S}}(p)\boldsymbol{A}^T\boldsymbol{Q}^T \tag{7.7}$$

This equation states that by diagonalizing the whitened covariance matrix at a particular time lag, the unitary matrix product ***QA*** can be determined, resulting in the mixing matrix, ***A***. The second step involves diagonalizing the matrix $\boldsymbol{T}_{\bar{X}}(p)$ whose eigenvalue decomposition satisfies,

$$\boldsymbol{V}_{\bar{X}}^T\boldsymbol{T}_{\bar{X}}(p)\boldsymbol{V}_{\bar{X}} = \boldsymbol{\Lambda}_{\bar{X}} \tag{7.8}$$

Hence the mixing matrix can be estimated by,

$$\hat{\boldsymbol{A}} = \boldsymbol{Q}^{-1}\boldsymbol{V}_{\bar{X}} = \boldsymbol{V}_X\boldsymbol{\Lambda}_X^{\frac{1}{2}}\boldsymbol{V}_X \tag{7.9}$$

where $\hat{\boldsymbol{A}}$ is the estimated matrix of $\boldsymbol{A}$. The problem now becomes one of unitary diagonalization of the correlation matrix $\boldsymbol{T}_{\bar{\boldsymbol{X}}}(p)$ at one or several non-zero time lag. This step is commonly known as the joint approximate diagonalization, implemented numerically. Denoting $\boldsymbol{D} = \boldsymbol{U}^T \tilde{\boldsymbol{T}}_{\bar{\boldsymbol{X}}}(p)\boldsymbol{U}$, the problem is now to find the minimum performance index J given by (A. Belouchrani et al. 1997; F. Musafere et al. 2016),

$$J(\boldsymbol{U}, p) = \sum_{p} \sum_{1 \le i \ne j \le n} \left| D_{ij}^{p} \right|^2 \tag{7.10}$$

Then, the unitary matrix $\boldsymbol{U}$ corresponding to the minimum J over fixed iterations is considered to be an approximate joint diagonalizer. Once the unitary matrix is computed, $\hat{\boldsymbol{A}}$ can be estimated and the source $\boldsymbol{s}$ is obtained using the following pseudo-inverse,

$$\hat{\boldsymbol{s}} = \hat{\boldsymbol{A}}^{-1}\boldsymbol{X} \tag{7.11}$$

which for the nDOF system under consideration is essentially,

$$\hat{\boldsymbol{q}} = \hat{\boldsymbol{\Psi}}^{-1}\boldsymbol{X} \tag{7.12}$$

7.1.2 Empirical Wavelet Transform (EWT)

Wavelet transform is one of the most popular and useful tools in signal analysis. In the temporal domain, a mother wavelet function $\psi(t)$ is defined as zero-mean and normalized as (Mallat, 1999),

$$\begin{aligned} &\int_{-\infty}^{\infty} \psi(t)dt = 0 \\ &\left\| \psi(t) \right\|_2 = \int_{-\infty}^{\infty} \psi(t)\psi^*(t)dt = 1 \end{aligned} \tag{7.13}$$

With a scaling parameter c greater than zero and a translating parameter u, an orthonormal basis can be obtained using multi-resolution property of discrete wavelet, and is defined by,

$$\{\psi_{c,u}(t) = \frac{1}{\sqrt{c}}\psi(\frac{t-u}{c})\}\,|_{u\in R, c\in R^+} \tag{7.14}$$

Via wavelet transform, a one-dimensional signal *f*(t) can be mapped to a two-dimensional coefficient $W_{f(c,u)}$ which is computed through the inner product $W_{f(c,u0} =< f(t), \psi_{c,u} >$. If c is a continuous variable then $W_{f(c,u)}$ is called the continuous wavelet transform while if $c = 2^j$ then it is called the discrete wavelet transform with a common dyadic choice of $c = 2^j$. For the details of classical wavelet theory, readers are referred to the literature (Mallat, 1999).

The Empirical Wavelet Transform (EWT) is recently proposed with the intention to build a family of wavelets adapted to the processed signal (Gilles, 2013). One of the key steps is to segment the Fourier spectrum, separating the spectrum into portions corresponding to different modes i.e. centered around a specific frequency and of compact support. The segment boundary detection can be achieved through different techniques, one of which is the "LocalMaxMin" detection (Gilles, 2013) employed in this paper. The first step is to detect the local maxima of the Fourier spectrum and sort them in decreasing order. This method then seeks the lowest local minima between two consecutive maxima and defines the boundary as in the position of the minima. With *N* number of detected maxima, there will be (*N*-1) boundaries defined and the spectrum is then divided into N supports. The empirical wavelets are then defined as bandpass filters on each segment where the empirical scaling and wavelets function are defined respectively as (n = 1, 2, ...) (Gilles, 2013).

$$\hat{\phi}_n(\omega) = \begin{cases} 1 & \text{if } |\omega| \le \omega_n - \tau_n \\ \cos[\frac{\pi}{2}\beta(\frac{1}{2\tau_n}(|\omega| - \omega_n + \tau_n))] & \text{if } \omega_n - \tau_n \le |\omega| \le \omega_n + \tau_n \\ 0 & \text{otherwise} \end{cases} \tag{7.15}$$

$$\hat{\psi}_n(\omega)=\begin{cases}1 & \text{if } \omega_n+\tau_n\le|\omega|\le\omega_{n+1}+\tau_{n+1}\\ \cos[\frac{\pi}{2}\beta(\frac{1}{2\tau_{n+1}}(|\omega|-\omega_{n+1}+\tau_{n+1}))] & \text{if } \omega_{n+1}-\tau_{n+1}\le|\omega|\le\omega_{n+1}+\tau_{n+1}\\ \sin[\frac{\pi}{2}\beta(\frac{1}{2\tau_n}(|\omega|-\omega_n+\tau_n))] & \text{if } \omega_n-\tau_n\le|\omega|\le\omega_n+\tau_n\\ 0 & \text{otherwise}\end{cases} \tag{7.16}$$

with the notation $\hat{f}$ representing the Fourier transform and $\breve{f}$ representing the inverse Fourier transform which will appear later. The function $\beta(x)$ is chosen to be,

$$\beta(x)=x^4(35-84x+70x^2-20x^3) \tag{7.17}$$

The choice of τ_n is simplified to $\lambda\omega_n$ and by properly choosing the parameter λ $(0<\lambda<1)$, a tight frame can be obtained.

The EWT of function f ($W_f^{\varepsilon}(n,t)$), can now be defined in the same way as for the classic wavelet transform with the detail coefficients being,

$$\begin{aligned}W_f^{\varepsilon}(n,t)&=<f,\psi_n>=\int f(\tau)\overline{\psi_n(\tau-t)}d\tau\\&=(\hat{f}(\omega)\overline{\hat{\psi}_n(\omega)})^{\vee}\end{aligned} \tag{7.18}$$

And the approximation coefficient being,

$$\begin{aligned}W_f^{\varepsilon}(0,t)&=<f,\psi_n>=\int f(\tau)\overline{\phi_1(\tau-t)}d\tau\\&=(\hat{f}(\omega)\overline{\hat{\phi}_1(\omega)})^{\vee}\end{aligned} \tag{7.19}$$

where $\hat{\psi}_n(\omega)$ and $\hat{\phi}_1(\omega)$ are defined in Eqs. (7.15) and (7.16), respectively. The signal *f*(t) is then reconstructed as,

$$\begin{aligned}f(t)&=W_f^{\varepsilon}(0,t)\bullet\phi_1(t)+\sum_{n=1}^{N}W_f^{\varepsilon}(n,t)\bullet\psi_n(t)\\&=(W_f^{\varepsilon}(0,\omega)\hat{\phi}_1(\omega)+\sum_{n=1}^{N}W_f^{\varepsilon}(n,\omega)\hat{\psi}_n(\omega))^{\vee}\end{aligned} \tag{7.20}$$

where the symbol "$\bullet$" presents the inner product. The empirical mode f_k is defined as,

$$\begin{aligned} f_0(t) &= W_f^{\varepsilon}(0,t) \bullet \phi_1(t) \\ f_k(t) &= W_f^{\varepsilon}(k,t) \bullet \psi_k(t) \end{aligned} \tag{7.21}$$

The following is an example of using EWT to decompose signal with multiple frequency component. The testing signal is comprised of two harmonic component with frequencies of 4 and 7.5 Hz,

$$\begin{aligned} f_{t1}(t) = \cos(8\pi t), f_{t2}(t) = 0.5\cos(15\pi t) \\ f_{sig}(t) = f_{t1}(t) + f_{t2}(t) \end{aligned} \tag{7.22}$$

The time history of f_{sig} is shown in Figure 7.1 (a) and Figure 7.1 (b) shows the detected boundary on the Fourier spectrum of f_{sig} as obtained using the EWT. The EWT decomposes the original signal into two modes which are shown in Figure 7.1 (c). The Fourier spectrum of each identified mode can be found in Figure 7.1 (d) revealing the signal decomposition capability of the EWT. It is worth noting that the number of modes of the signal is fixed apriori to ensure the best performance of the EWT. This is not the case in general when there is no such available information. A simple way to estimate the appropriate number of modes can be found in literature (Gilles, 2013) and further investigation is required for robust performance of the EWT.

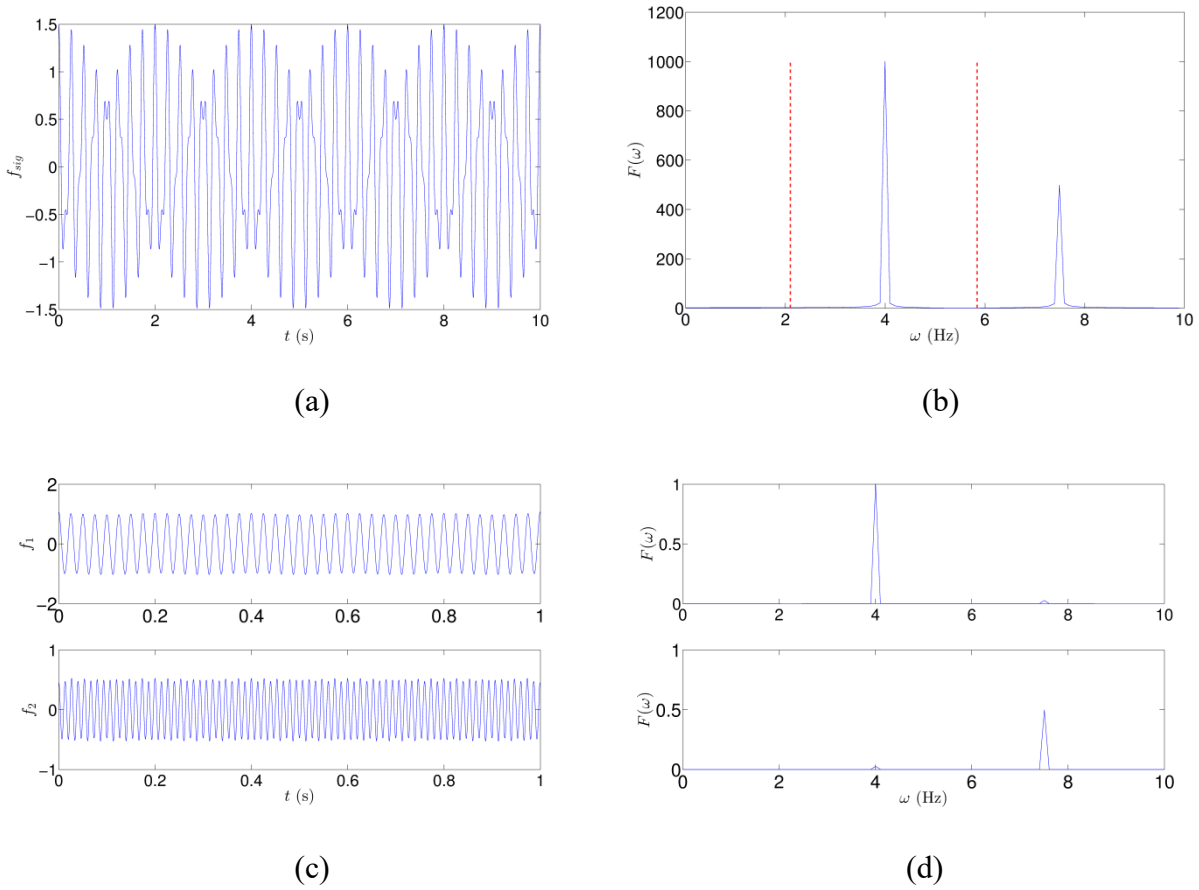

Figure 7.1. Example of using EWT for signal decomposition

7.2 Proposed method

The performance of the SOBI is not guaranteed for all cases to be satisfactory. In spite of its good separation of the higher modes of the structure, mode-mixed responses in lower modes with closely-spaced frequencies are often observed (Musafere, Sadhu, & Liu, 2016). In view of both the advantages and limitations of the SOBI and EWT, a combined method, i.e., SOBI-EWT method, is introduced.

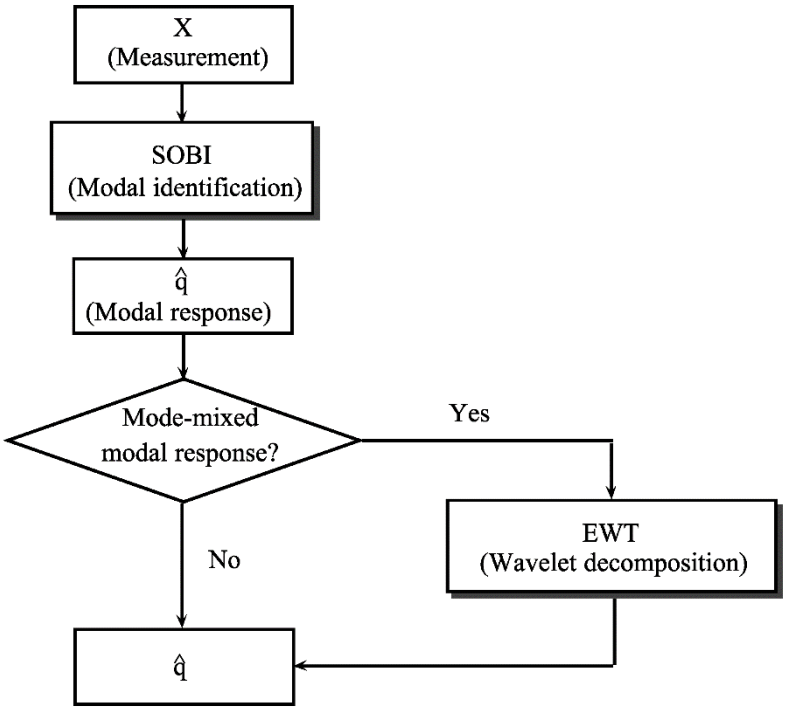

Figure 7.2. Flowchart of the proposed method

The main idea is to use the EWT to further decompose the separated sources from the SOBI which contain mode-mixing signals in case of closely-spaced frequencies. A flowchart of the proposed method is given in Figure 7.2. The measurement $\boldsymbol{X}_{n\times m}$ (n is the number of sensors and m is the number of data points) is first used as the input to the SOBI algorithm. After performing the SOBI, the estimated sources are given as,

$$\hat{\boldsymbol{q}} = \hat{\boldsymbol{\Psi}}^{-1}\boldsymbol{X} \tag{7.23}$$

which represent the modal coordinates.

Applying the Fast Fourier Transform (FFT) to the extracted modal coordinates, the spectra give information on the modal frequencies and reveal whether there is any mode-mixed signal. If the modes are well-separated, $\hat{\boldsymbol{q}}_{n\times m}$ is accepted as the final result. Otherwise, the estimated modal responses with mixed modes are processed by the EWT algorithm. Adaptive bandpass filters are

built based on the information contained in the spectrum of the mode-mixing signal, which has certain dominant frequencies after the SOBI operation.

For the case studied in this chapter, only one TMD is used to suppress a single-mode vibration. The SOBI is more capable of separating the higher order of frequencies, leaving the first two modal responses both mixed with the first two natural frequencies. The EWT yields those two frequencies using either of the first two columns of the estimated source matrix $\hat{\boldsymbol{q}}$ from the results of the SOBI. The coefficients are given as,

$$\begin{aligned} W_{\hat{\boldsymbol{q}}_i}^{\varepsilon}(0,t) &= <\hat{\boldsymbol{q}}_i, \phi_1> \\ W_{\hat{\boldsymbol{q}}_i}^{\varepsilon}(n,t) &= <\hat{\boldsymbol{q}}_i, \psi_n> \end{aligned} \tag{7.24}$$

Where $\hat{\boldsymbol{q}}_i$ represents the *i*th column of $\hat{\boldsymbol{q}}$. Empirical modes are then obtained as,

$$\begin{aligned} \boldsymbol{q}_0(t) &= W_{\hat{\boldsymbol{q}}_i}^{\varepsilon}(0,t) \bullet \phi_1(t) \\ \boldsymbol{q}_k(t) &= W_{\hat{\boldsymbol{q}}_i}^{\varepsilon}(k,t) \bullet \psi_k(t) \end{aligned} \tag{7.25}$$

Combining the higher modes identified by the SOBI, the complete structural modes are acquired.

In summary, the proposed method is an integration of the SOBI and EWT method. On one hand, the separation result of the SOBI method is improved by the employment of the EWT as the EWT can better handle the remaining mixed modal response of closely-spaced modes. On the other hand, the extracted modal responses by the SOBI provide a decent source for the EWT to separate the mode-mixing signals.

7.3 Simulation results

7.3.1 Numerical model

A 6-storey model is utilized in simulation to demonstrate the effectiveness of the proposed methodology. Each floor mass of the primary 6DOF structure is given as (Pioldi, Ferrari, & Rizzi,

2016): $m_i = 1.44\times10^5$ kg, i=1,2,⋯,6 . The stiffness coefficients are given as: $k_1 = 3.045\times10^9$ N/m , $k_2 = 2.842\times10^9$ N/m , $k_3 = 2.639\times10^9$ N/m , $k_4 = 2.436\times10^9$ N/m , $k_5 = 2.233\times10^9$ N/m and $k_6 = 2.03\times10^9$ N/m. The natural frequencies are listed in Table 2. Rayleigh damping approximation is used to form the damping matrix $\boldsymbol{C}_p = \alpha\boldsymbol{M}_p + \beta\boldsymbol{K}_p$ where $\boldsymbol{M}_p$ is the mass matrix and $\boldsymbol{K}_p$ is the stiffness matrix of the primary system. $\alpha = 0.7716$ and $\beta = 0.0025$ assuming that the first two damping ratios are 5%. Using white Gaussian noises as the floor excitations in the primary structure, the modal responses are extracted using the SOBI method and the natural frequencies are indented from the FFT spectra of the modal responses as shown in Figure 7.3. Table 7.1 compares the true natural frequencies ω_i with the identified ones $\hat{\omega}_i$.

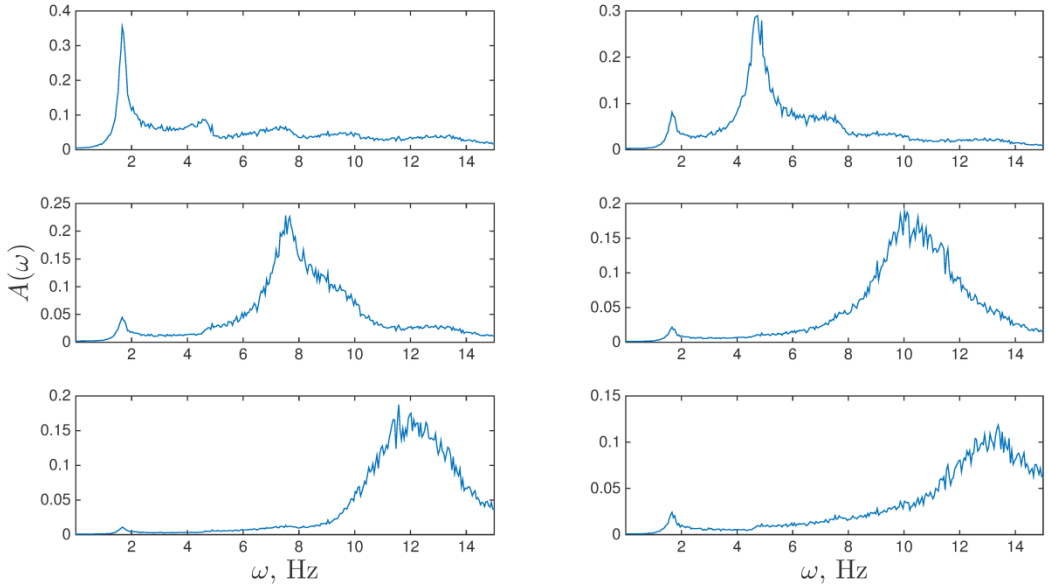

Figure 7.3. FFT spectra of the identified modal response of the primary structure

Table 7.1. Identified natural frequencies of the primary structure by the SOBI

Mode No.	1	2	3	4	5	6
ω_i (Hz)	1.67	4.67	7.45	9.79	11.57	13.08
$\hat{\omega}_i$ (Hz)	1.66	4.69	7.23	9.73	11.26	12.22

A model A TMD is installed on the top floor to suppress the vibration of the first mode. According to Den Hartog's "fixed-points" theory, the optimum tuning parameters for the single-degree-of-freedom (SDOF) system are given as,

$$\begin{aligned} \beta_{opt} &= \frac{1}{1+\mu} \\ \zeta_{opt} &= \sqrt{\frac{3\mu}{8(1+\mu)^3}} \end{aligned} \tag{7.26}$$

with the following notation,

$$\beta = \frac{\omega_a}{\omega_p}, \mu = \frac{m_a}{m}, \zeta = \frac{c_a}{2m_a\omega_p}, \omega_p = \sqrt{\frac{k}{m}}, \omega_a = \sqrt{\frac{k_a}{m_a}} \tag{7.27}$$

where m and m_a are the primary mass and absorber mass respectively, k and k_a are the primary spring stiffness and absorber spring stiffness, respectively, c_a is the damping value of the absorber damper. This method to design an optimum TMD for a SDOF system can be extended to suppress a single mode of the 6DOF structure under consideration, provided that the modal mass is obtained using a mode shape vector normalized with respect to the element corresponding to the location of the TMD (Rana & Song, 1998). Assuming that the TMD is attached to the last mass, the mode shape vector of the first mode for the 6DOF structure is normalized with respect to the last element in the array.

$$\boldsymbol{\Phi}_{1n} = [\frac{\Phi_{11}}{\Phi_{16}} \ \frac{\Phi_{12}}{\Phi_{16}} \ \frac{\Phi_{13}}{\Phi_{16}} \ \frac{\Phi_{14}}{\Phi_{16}} \ \frac{\Phi_{15}}{\Phi_{16}} \ 1] \tag{7.28}$$

Hence the modal mass is obtained using $M_1 = \boldsymbol{\Phi}_{1n}^T \boldsymbol{M} \boldsymbol{\Phi}_{1n}$. Assuming a mass ratio μ of 5%, the mass of the TMD is taken as $m_a = 2.20 \times 10^4$ kg. According to Eq. (7.26), the absorber damping coefficient would be $c_a = 6.5 \times 10^4$ Ns/m.

The state-space model of the combined system is given as,

$$\begin{aligned} \dot{\boldsymbol{X}} &= \boldsymbol{A}_{ss}\boldsymbol{X} + \boldsymbol{B}_{ss}\boldsymbol{U}_{ss} \\ \boldsymbol{Y} &= \boldsymbol{C}_{ss}\boldsymbol{X} + \boldsymbol{D}_{ss}\boldsymbol{U}_{ss} \end{aligned} \tag{7.29}$$

Where $\boldsymbol{X}$ is the state vector and $\boldsymbol{Y}$ is the output governed by the $\boldsymbol{C}_{ss}$ matrix. Matrix $\boldsymbol{B}_{ss}$ determines the location of the excitation and matrix $\boldsymbol{U}_{ss}$ is the input matrix. System matrix $\boldsymbol{A}_{ss}$ is constructed using the mass, stiffness and the damping properties of the structure:

$$\boldsymbol{M}=\begin{bmatrix}[\boldsymbol{M}_p]_{6\times6} & [0]_{6\times1}\\ [0]_{1\times6} & m_a\end{bmatrix},\boldsymbol{K}=\begin{bmatrix}[\boldsymbol{K}_p]_{6\times6} & [0]_{6\times1}\\ [0]_{1\times6} & [0]_{1\times1}\end{bmatrix}+\begin{bmatrix}[0]_{5\times5} & [0]_{5\times2}\\ [0]_{1\times6} & k_a\begin{bmatrix}1 & -1\\ -1 & 1\end{bmatrix}\end{bmatrix}$$
$$\boldsymbol{C}=\begin{bmatrix}[\boldsymbol{C}_p]_{6\times6} & [0]_{6\times1}\\ [0]_{1\times6} & [0]_{1\times1}\end{bmatrix}+\begin{bmatrix}[0]_{5\times5} & [0]_{5\times2}\\ [0]_{1\times6} & c_a\begin{bmatrix}1 & -1\\ -1 & 1\end{bmatrix}\end{bmatrix},\boldsymbol{A}=\begin{bmatrix}[0]_{7\times7} & [\boldsymbol{I}]_{7\times7}\\ -\boldsymbol{M}^{-1}\boldsymbol{K} & -\boldsymbol{M}^{-1}\boldsymbol{C}\end{bmatrix} \tag{7.30}$$

where $\boldsymbol{I}$ represents identity matrix.

7.3.2 Identification results

The responses of the above described system under base excitation are calculated in MATLAB with a Gaussian white noise as the input signal. The proposed method is then implemented to conduct modal identification and the results are presented below.

7.3.2.1 Optimally tuned TMD

Figure 7.4 compares the Fourier spectrum of the each floor response of the primary structure with that of the structure equipped with the optimally-tuned TMD. It is clear that the vibration of the first mode is significantly suppressed. FFT spectra of the modal responses extracted by the SOBI method are shown in Figure 7.5, revealing that the first two modes are mixed.

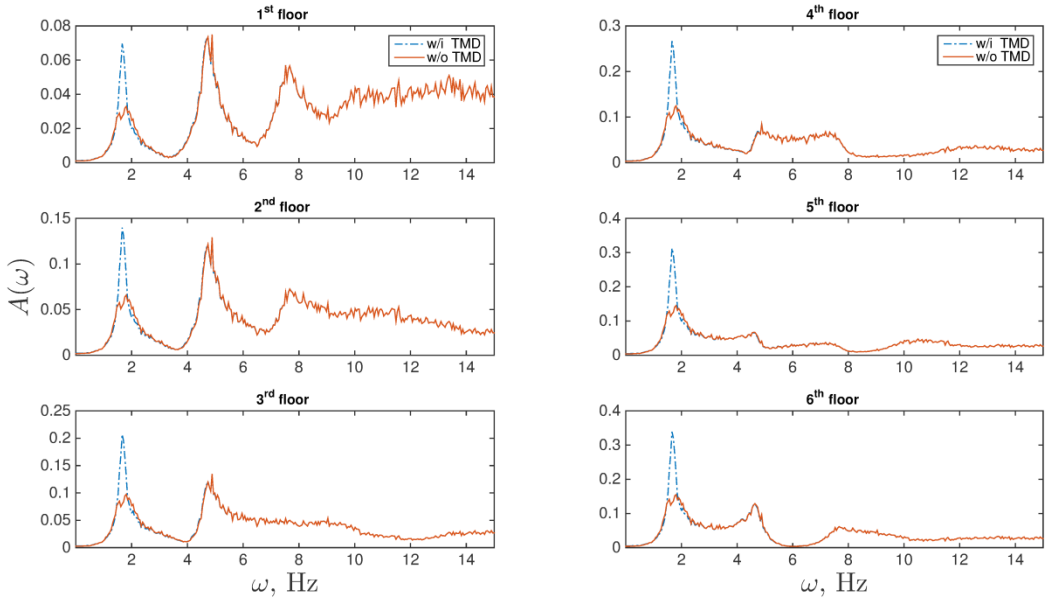

Figure 7.4. FFT spectra of the floor response of the structure equipped with an optimally-tuned TMD

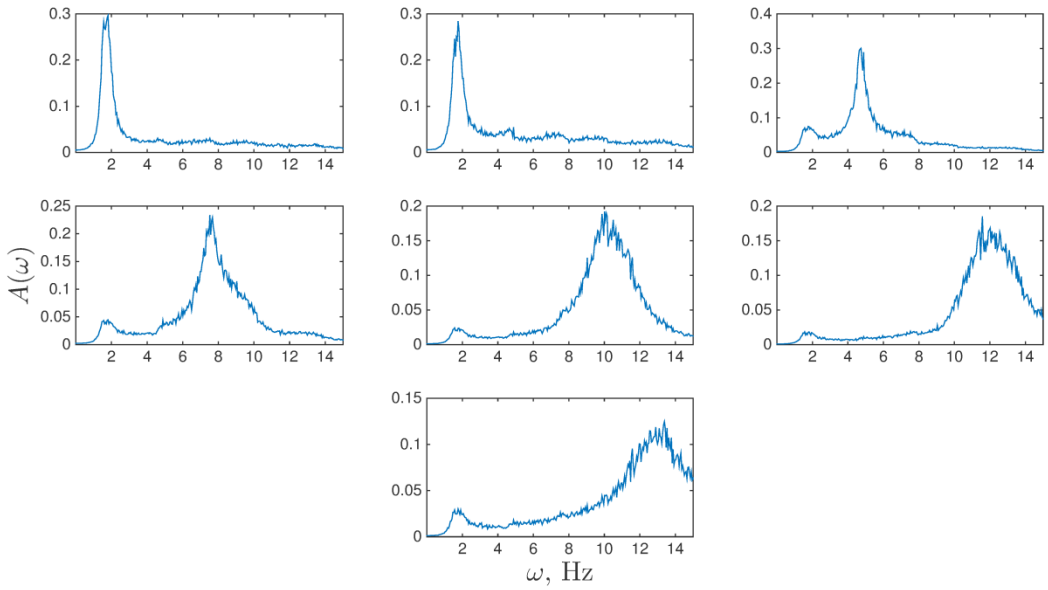

Figure 7.5. Identified results using the SOBI method

A close-up image of the Fourier spectrum of the first modal response is shown in Figure 7.6. The identified frequency values are listed in Table 7.2 with the computed ones listed for comparison.

For the first two sub-figures, the frequencies corresponding to the two peaks are $\omega_{s1} = 1.56$ Hz and $\omega_{s2} = 1.81$ Hz with the second peak over-passing the first one. This renders the identification of the first natural frequency a manual job when the algorithm is programmed to pick the frequency corresponding to the highest peak, in which the first two natural frequencies are identified to be the same as 1.81 Hz. Therefore, in presence of closely-spaced modes, the SOBI is inaccurate. Hence the EWT is used with the input being the mode-mixed responses from the SOBI. The FFT spectra of the decomposed EWT components are shown in Figure 7.7. The frequencies corresponding to the peaks in both figures are $\omega_{e1} = 1.56$ Hz and $\omega_{e2} = 1.81$ Hz respectively that fairly match with the correct values.

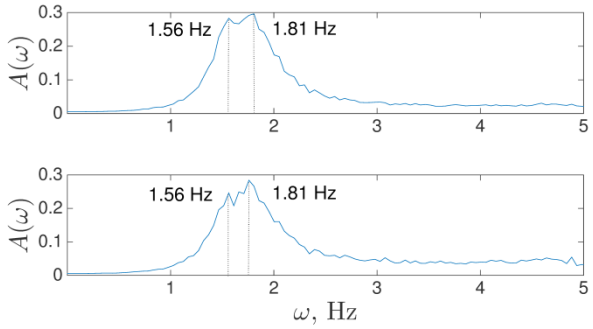

Figure 7.6. FFT spectra of the first two modal responses extracted by the SOBI

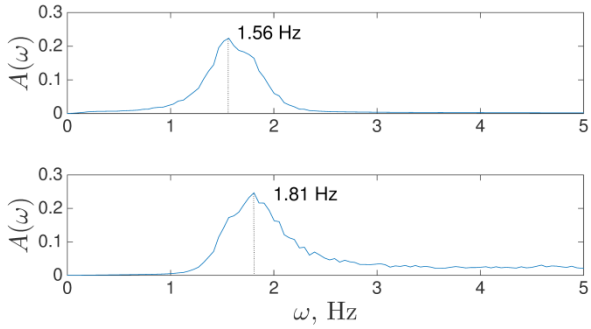

Figure 7.7. FFT spectra of the first two modal responses extracted by the EWT

Table 7.2. Identified natural frequencies of the structure with the TMD by the proposed method

	Optimally tuned		Detuned			
Mode No.	$\beta = 1.026$		$\beta = 0.9$		$\beta = 1.2$	
	ω_i	$\hat{\omega}_i$	ω_i	$\hat{\omega}_i$	ω_i	$\hat{\omega}_i$
1	1.50	1.56	1.40	1.42	1.57	1.56
2	1.81	1.81	1.78	1.76	2.11	2.05
3	4.69	4.69	4.68	4.64	4.70	4.64

4	7.45	7.57	7.45	7.67	7.46	7.62
5	9.79	9.62	9.79	9.97	9.79	9.89
6	11.5	11.19	11.59	11.53	11.59	11.53
7	13.08	12.07	13.08	12.12	13.08	12.21

7.3.2.2 Detuned TMD

The performance of the TMD can be severely affected by the de-tuning. In order to restore the TMD's optimum performance, it is important to estimate the modal properties of the system and conduct re-tuning process. The performance of the proposed method in de-tuning cases is investigated and presented in this section. The de-tuning is simulated with the variation of the parameter β ($\beta = 1.026$ as optimum), and two values of ($\beta = 0.9$ and 1.2) are chosen.

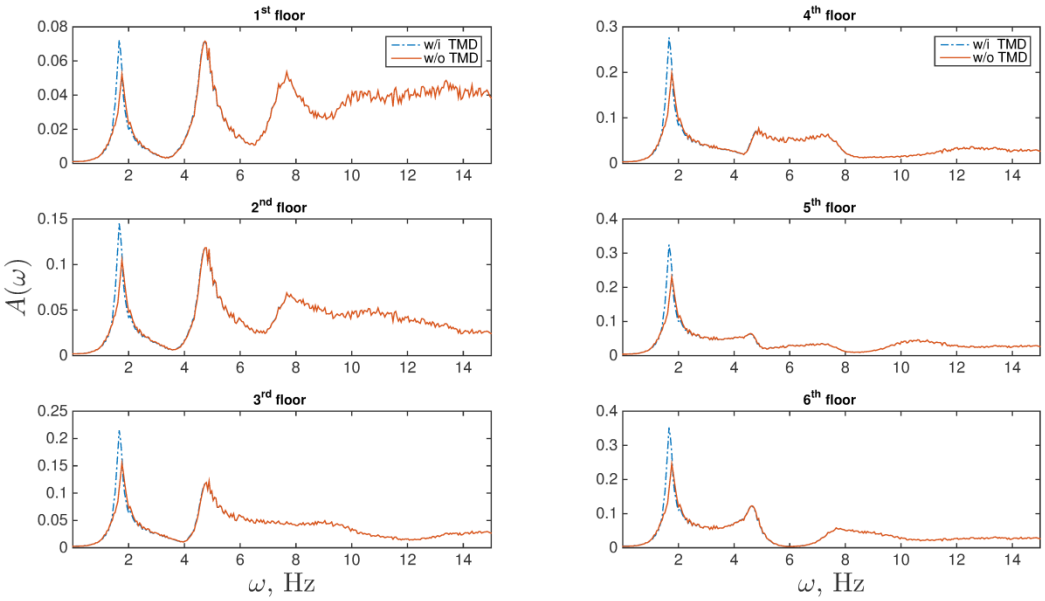

Figure 7.8. FFT spectra of the floor responses of the structure with a de-tuned TMD (β=0.9).

When $\beta = 0.9$, Figure 7.8 shows that the de-tuning has significantly affected the performance of the TMD with little suppression on the first mode. The identification results of the SOBI method are shown in Figure 7.9 and Figure 7.10, revealing significant mode mixing and inconsistent

estimation in the first two modes. The EWT method is then employed to separate the mode-mixed as shown in Figure 7.11. The identified frequency values ($\hat{\omega}_i$) are listed in Table 7.2 with the computed ones (ω_i). The frequencies corresponding to the two peaks are $\hat{\omega}_1 = 1.42\text{Hz}$ and $\hat{\omega}_2 = 1.76\ \text{Hz}$, respectively.

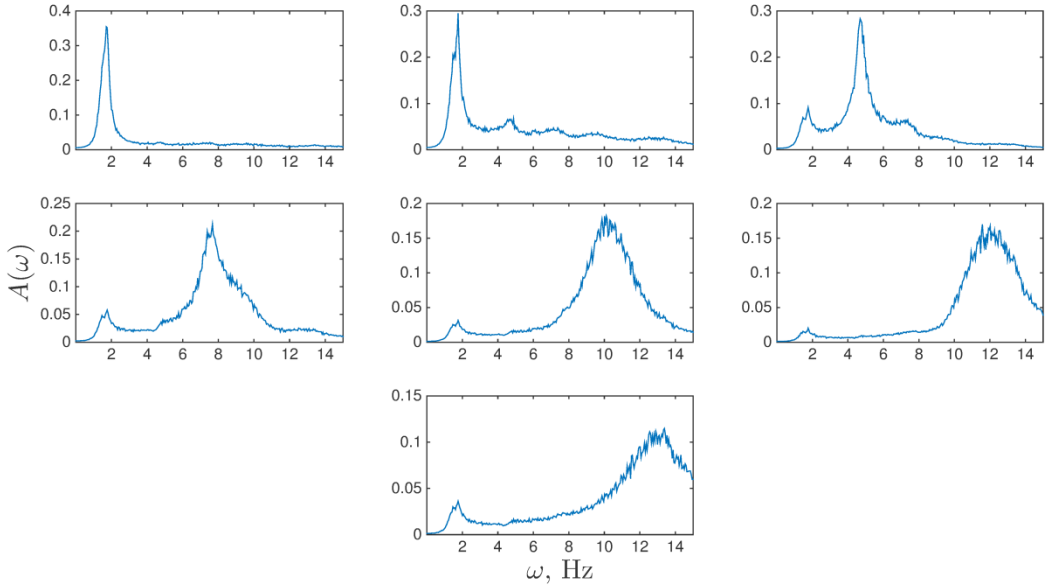

Figure 7.9. FFT spectra of the modal responses extracted by the SOBI (β=0.9).

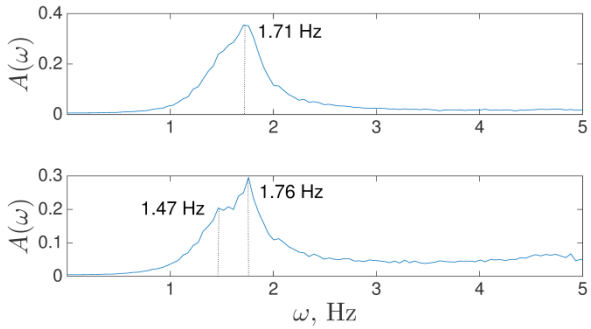

Figure 7.10. FFT spectra of the first two modal responses extracted by the SOBI (β=0.9).

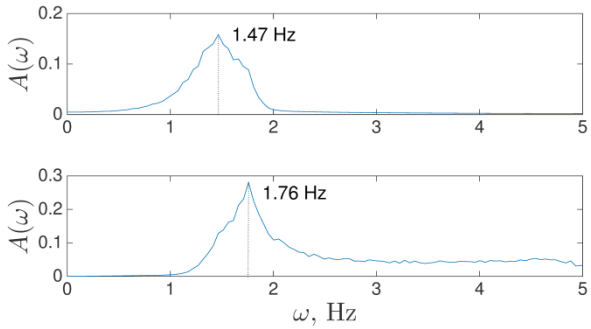

Figure 7.11. FFT spectra of the first two modal responses extracted by the EWT (β=0.9).

When $\beta = 1.2$, the suppression of the first mode of vibration also deteriorates due to the de-tuning. The FFT spectra of the first two modal response are given in Figure 7.12. The identification result from the EWT is shown in Figure 7.13 with the two natural frequencies identified as $\hat{\omega}_1 = 1.56\text{Hz}$ and $\hat{\omega}_2 = 2.05$ Hz, respectively. The identification results are listed in Table 7.2 that corroborate with the accuracy of the proposed method.

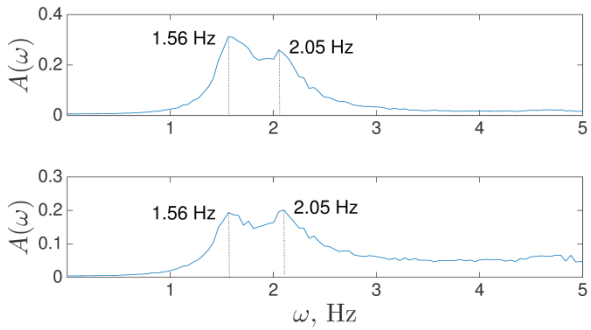

Figure 7.12. FFT spectra of the first two modal responses extracted by the SOBI (β=1.2).

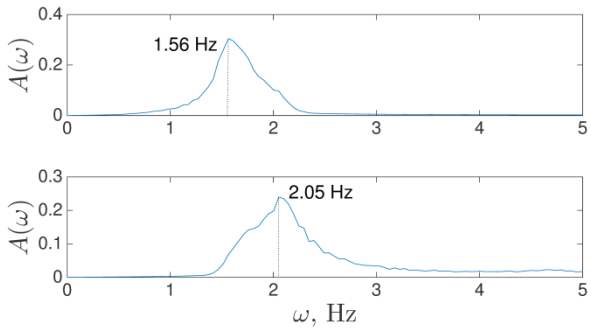

Figure 7.13. FFT spectra of the first two modal responses extracted by the EWT (β=1.2).

In terms of the measurement noise in the data which is the general case for practical applications, the performance of the proposed method is also investigated. The results are shown in Table 4 with the signal-to-noise ratio (SNR) of 5 and 20 respectively. It may be observed that the proposed method is insensitive to the presence of noise and can be used as a powerful tool to separate closely-spaced frequencies using the responses contaminated with measurement noise.

Table 7.3. Identification results of the 6-DOF model using the proposed method.

	Optimally tuned TMD			Detuned					
Mode	$\beta=1.026$			$\beta=0.9$			$\beta=1.2$		
SNR		20	5		20	5		20	5
	ω_i	$\hat{\omega}_i$	$\hat{\omega}_i$	ω_i	$\hat{\omega}_i$	$\hat{\omega}_i$	ω_i	$\hat{\omega}_i$	$\hat{\omega}_i$
1	1.50	1.56	1.56	1.40	1.47	1.47	1.57	1.56	1.61
2	1.81	1.81	1.81	1.78	1.76	1.76	2.11	2.05	2.05
3	4.69	4.69	4.69	4.68	4.64	4.64	4.70	4.64	4.64
4	7.45	7.57	7.57	7.45	7.67	7.67	7.46	7.62	7.62
5	9.79	9.67	9.62	9.79	9.97	9.97	9.79	9.87	9.87
6	11.59	11.19	11.19	11.59	11.53	10.99	11.59	11.19	11.19
7	13.08	12.07	12.07	13.08	12.26	12.26	13.08	12.21	12.21

7.4 Experiment results

The proposed method is now applied to identify detuning of a TMD attached to a 3- storey model. Figure 7.14 shows the experimental setup and measurement system. The TMD consists of a cantilever beam with an aluminum block attached to its free end. The mass of the aluminum block is found to be 0.156 kg. The cantilever beam has a total length of 259 mm and can be adjusted to achieve both optimum tuning and detuning cases.

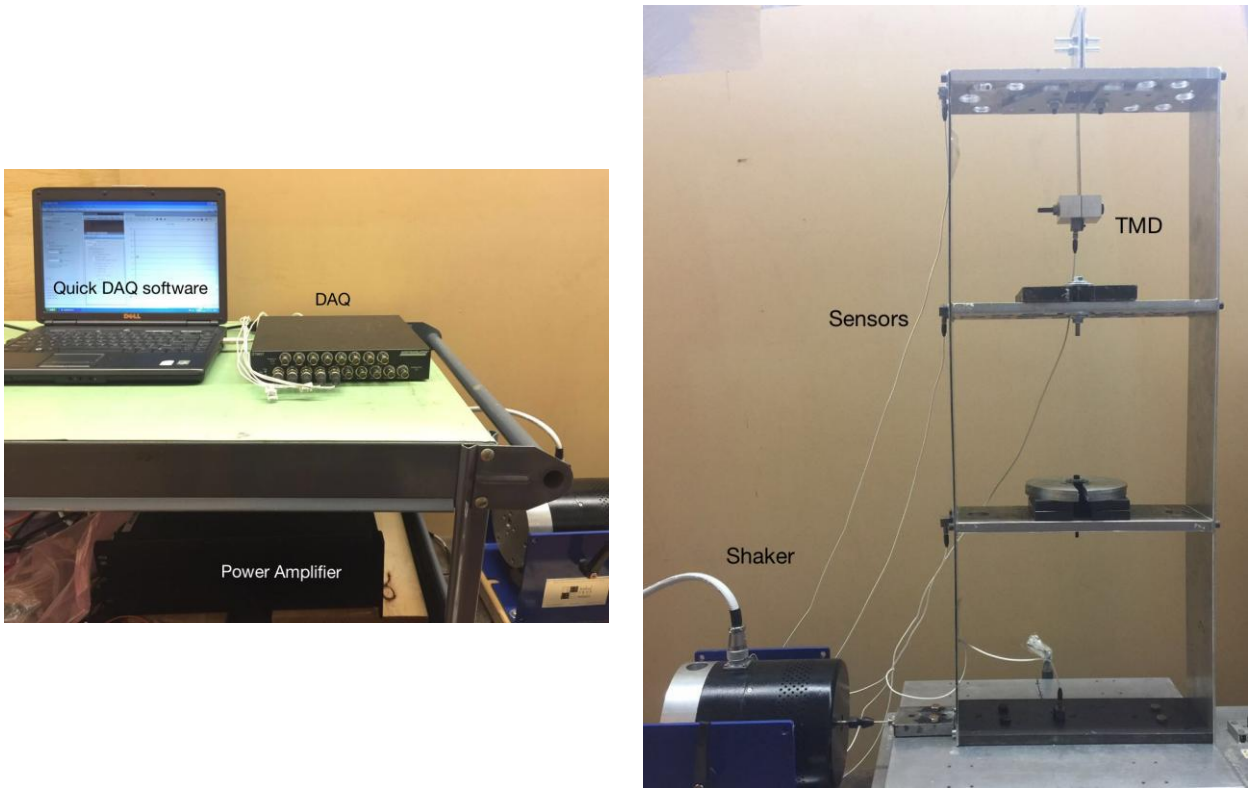

Figure 7.14. Experimental model.

System identification is first conducted on the primary system. The identified system parameters are listed in Table 7.4. The mass of each floor are obtained from measurement. Free vibration tests are conducted, resulting in the natural frequencies of the primary system. With the modal responses of the primary structure by the SOBI, autocorrelation functions are calculated and yields the modal damping ratios (Figure 7.15). With the mass of the floor and the natural

frequencies, the stiffness of each DOF is found out by a numerical optimization with the Nelder-Mead sequential complex method.

Table 7.4. Identified primary system parameters.

Floor mass	$m_{1(top)} = 0.99$ kg $m_{2(middle)} = 2.63$ kg $m_{3(bottom)} = 4.27$ kg
Frequency	$\omega_1 = 6.25$ Hz $\omega_2 = 17.55$ Hz $\omega_3 = 29.45$ Hz
Stiffness	$k_1 = 13900$ N/m $k_2 = 22300$ N/m $k_3 = 20700$ N/m
Damping ratio	$\zeta_1 = 0.5\%$ $\zeta_2 = 0.3\%$ $\zeta_3 = 0.2\%$

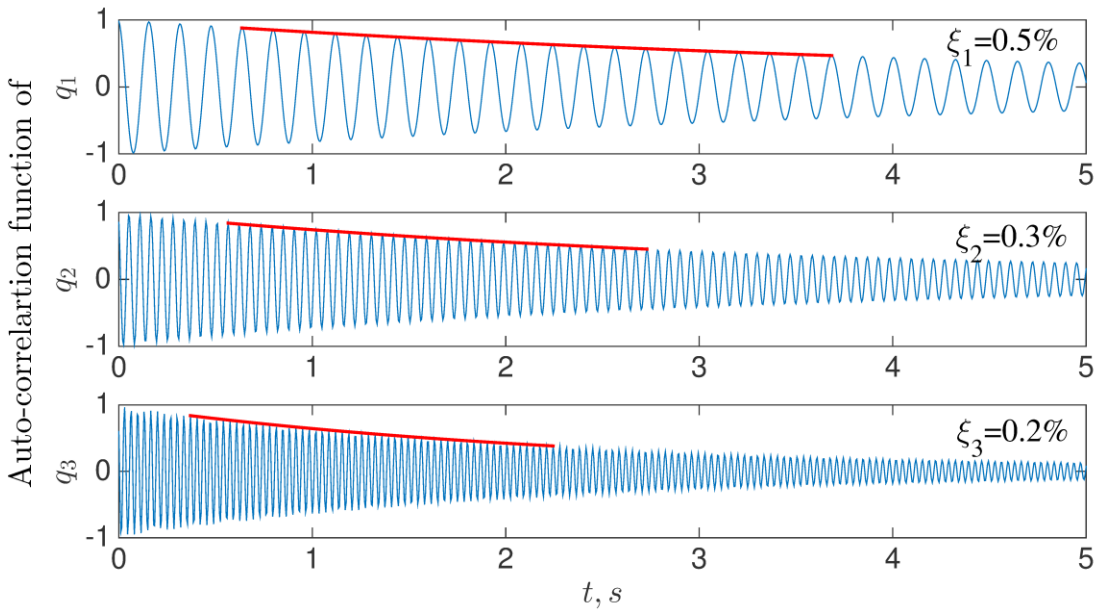

Figure 7.15. Damping estimation of the primary structure.

Based on the obtained parameters, the mass and stiffness matrices are formed and a mathematical model of the test apparatus is established. By solving the eigenvalue problem, the mode shape of the structure is obtained. Following the design procedure stated in the previous section, the first modal mass is found to be,

$$M_1 = \boldsymbol{\Phi}_{1n}^T \boldsymbol{M} \boldsymbol{\Phi}_{1n} = \begin{bmatrix} 0.69 \\ 0.93 \\ 1.00 \end{bmatrix}^T \begin{bmatrix} 4.732 & & \\ & 2.632 & \\ & & 0.990 \end{bmatrix} \begin{bmatrix} 0.69 \\ 0.93 \\ 1.00 \end{bmatrix} = 5.3 \text{ kg} \tag{7.31}$$

The mass of the TMD aluminum block is found to be 3% of the first modal mass. For an optimum TMD, the criterion is to set the frequency ratio $\beta = 1.015$, i.e., $\omega_a = 6.35$ Hz. The stiffness of the cantilever beam is thus found to be 248 N/m which corresponds to a beam length of 159 mm. With a minor adjustment, the length of the beam is first set to be 165 mm. Free vibration test is conducted on the standalone TMD and the damping ratio of the TMD is found to be approximately 0.6% through logarithmic decrement method. After the installation of TMD, free vibration test is conducted and the resulting FFT spectra of the data (as shown in Figure 7.16)

yield natural frequencies of the structure. These results also serve as the baseline for the comparison with the identified frequencies as shown in Table 7.4.

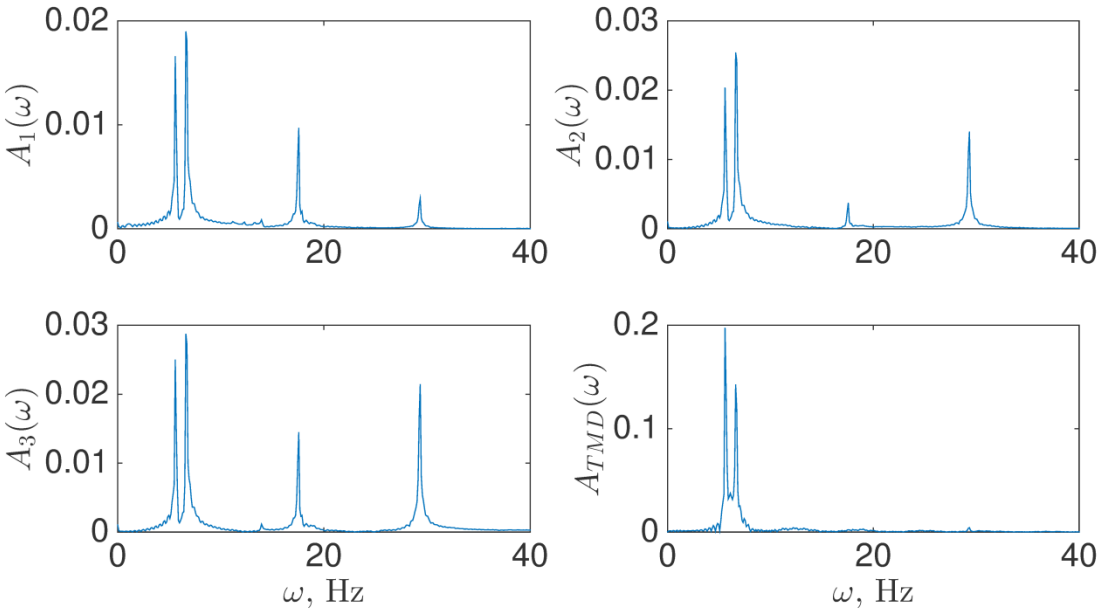

Figure 7.16. FFT spectra of free vibration of the experimental model with the optimum TMD.

A modal shaker (model number: 2100E11) manufactured by Modal Shop is employed in the experiment to simulate the excitation. The shaker is capable of applying sine, shock, sine sweep and random excitation. The system is first subjected to a harmonic excitation with an exciting frequency of 7 Hz which is close to the first natural frequency of the primary system. Segments of acceleration time-histories of the top floor of the structure, with and without the optimal TMD, are shown in Figure 7.17. It can be noticed that the presence of TMD has successfully reduced the structure vibration, justifying the effectiveness of TMD. During the modal identification, in order to excite all the structural modes, the model is now subjected to a base excitation with band limited random signal having a center frequency of 25 Hz and the frequency range of 50 Hz. Figure 7.18 shows the measured base excitation within 15 seconds and its FFT spectra. The proposed method is then implemented to conduct the modal identification.

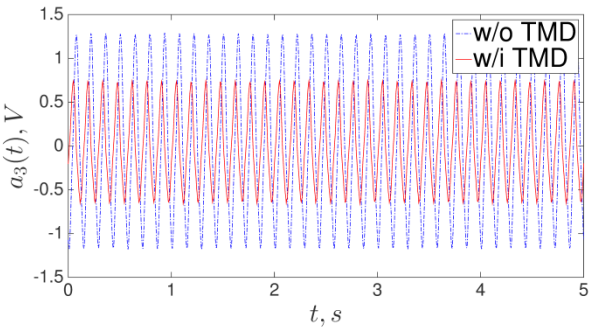

Figure 7.17. Comparison of the top floor response under harmonic excitation

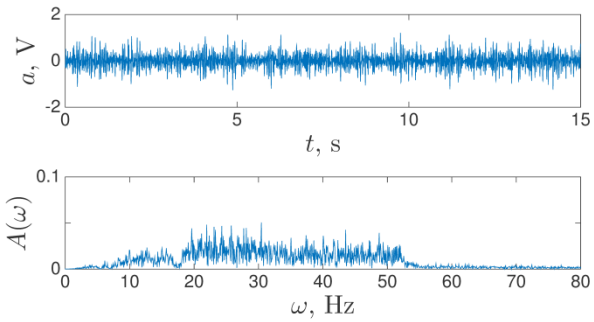

Figure 7.18. Ground excitation and its FFT spectra.

The FFT spectra of the modal responses extracted by the SOBI are shown in Figure 7.19. As can be seen, the higher two modes are well separated. Yet mode-mixed responses are witnessed in the figures of the first row and a close-up view is presented in Figure 7.20. It can be seen that SOBI yields partially inaccurate modal identification where both the peak frequencies are 6.21 Hz. The EWT is further employed and the FFT spectra of the separated modal responses are shown in Figure 7.21. A detailed comparison of actual and estimated values of frequencies are listed in Table 7.5.

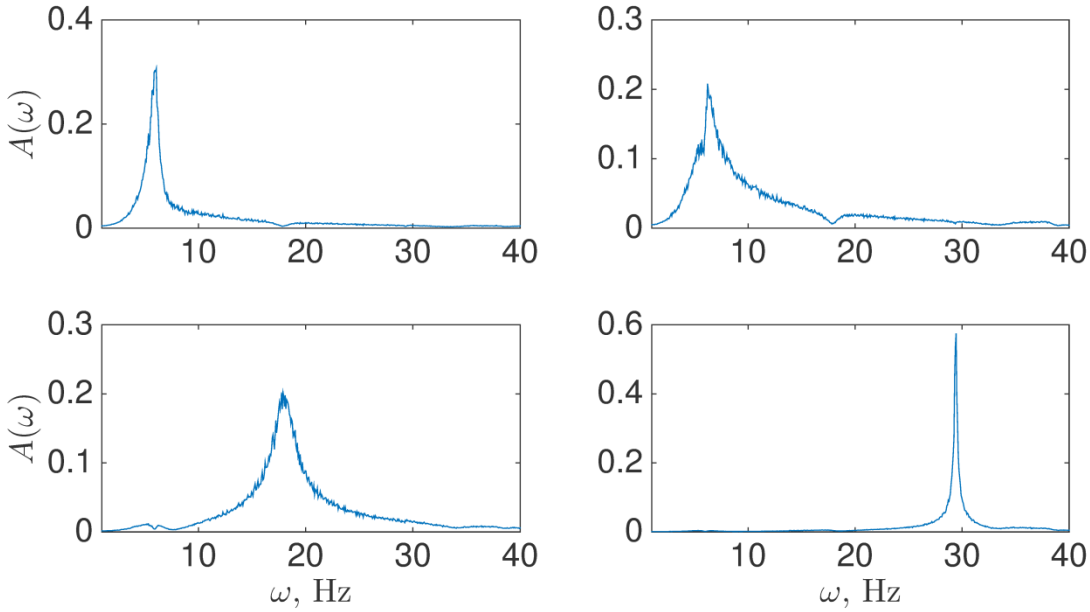

Figure 7.19. FFT spectra of the modal response extracted by SOBI (μ=0.03, optimally tuned)

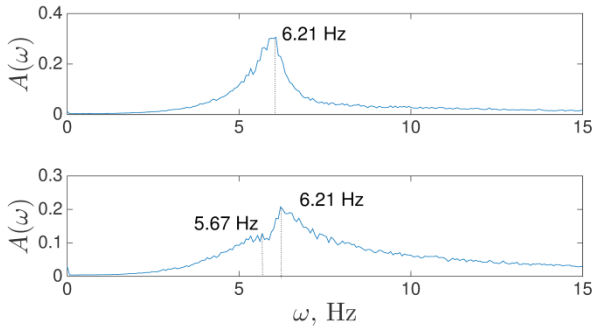

Figure 7.20. FFT spectra of the first two modal responses identified by the SOBI (μ=0.03, optimally tuned)

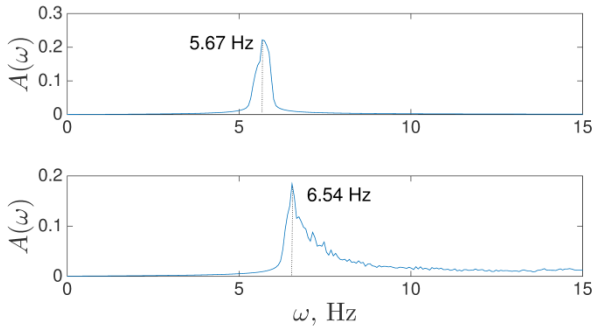

Figure 7.21. FFT spectra of the first two modal responses identified by the EWT (μ=0.03, optimally tuned)

The de-tuning case is also investigated by changing the length of the TMD pendulum to 125 mm. The results identified by the SOBI is presented in Figure 7.22 and Figure 7.23. Figure 7.24 shows the FFT spectra of the modal responses further separated from Figure 7.23 by the EWT. The identified frequency values, as well as those from free-response test, are listed in Table 7.5, revealing the accuracy of the proposed method.

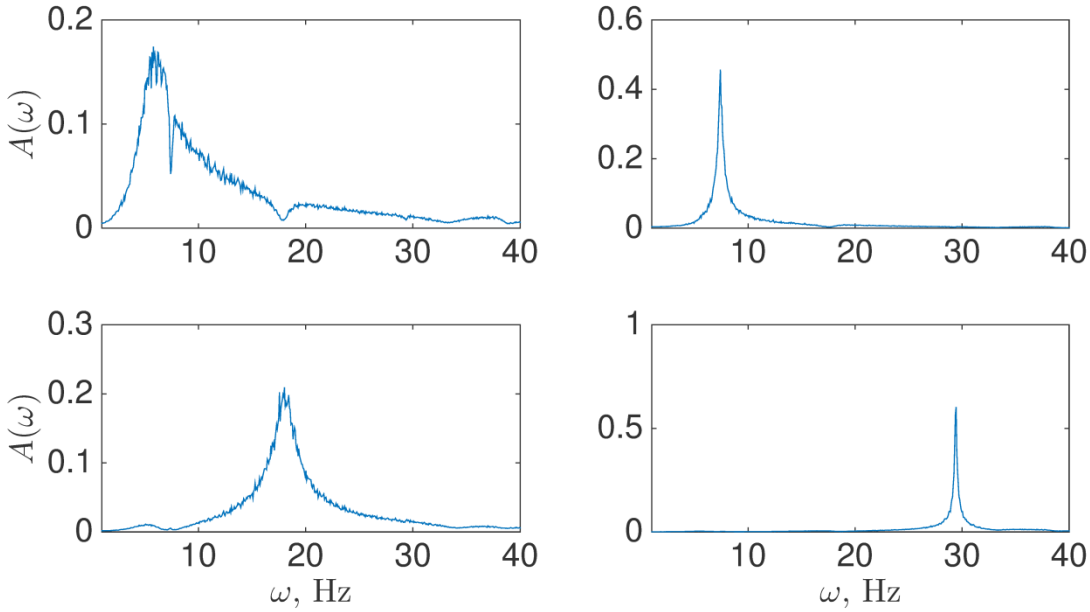

Figure 7.22. FFT spectra of the modal response extracted by SOBI (μ=0.03, detuned)

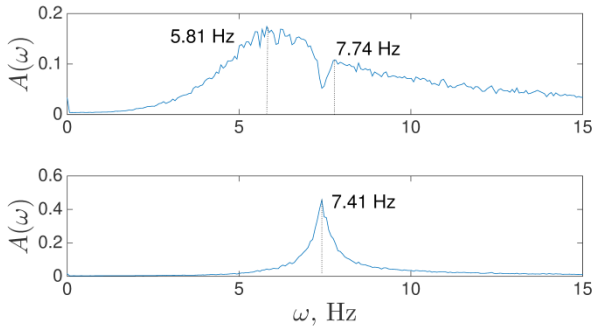

Figure 7.23. FFT spectra of the first two modal responses identified by the SOBI (μ=0.03, detuned)

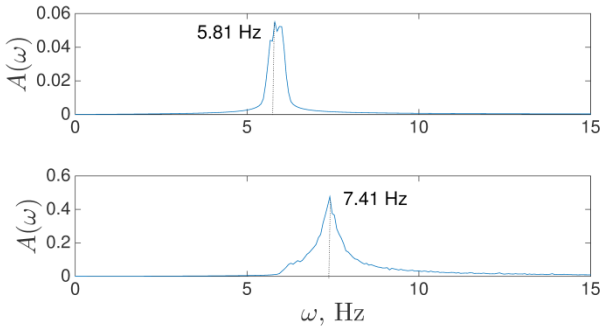

Figure 7.24. FFT spectra of the first two modal responses identified by the EWT (μ=0.03, detuned)

Another type of optimum tuning case is emulated by attaching an additional mass to the TMD. The mass ratio is changed to 5%. In Figure 7.25 and Figure 7.26, mode-mixed is observed in the identification results by the SOBI. The proposed method is then undertaken and the results are shown in Figure 7.27. The identified frequency values, as well as that of a detuning case, are reported in Table 7.5. The results further reveal that the proposed method is effective in identifying the closely-spaced frequencies under both optimally tuned and de-tuned cases.

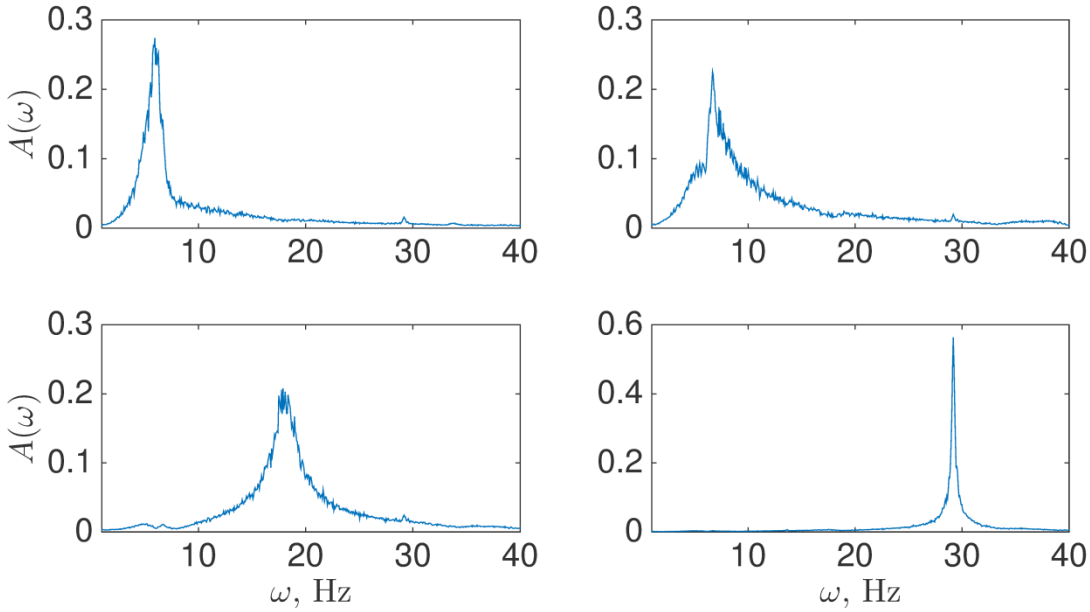

Figure 7.25. FFT spectra of the modal response extracted by SOBI (μ=0.05, optimally tuned)

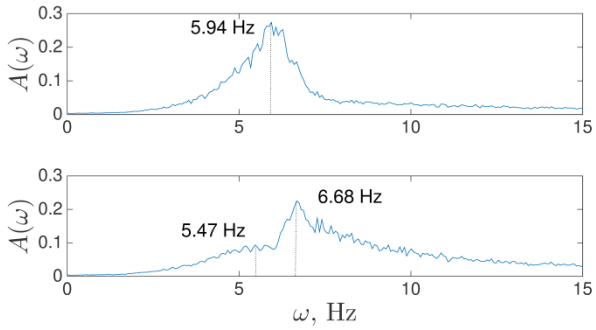

Figure 7.26. FFT spectra of the first two modal responses identified by the SOBI (μ=0.05, optimally tuned)

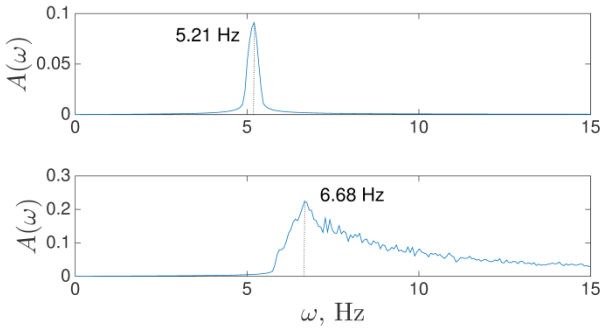

Figure 7.27. FFT spectra of the first two modal responses identified by the EWT (μ=0.05, optimally tuned)

Table 7.5. Identification results of the experimental model using the proposed method

	Optimally tuned				Detuned			
Mode No.	$\mu=0.03$		$\mu=0.05$		$\mu=0.03$		$\mu=0.05$	
	ω_i	$\hat{\omega}_i$	ω_i	$\hat{\omega}_i$	ω_i	$\hat{\omega}_i$	ω_i	$\hat{\omega}_i$
1	5.64	5.67	5.45	5.21	5.98	5.81	5.72	5.81
2	6.68	6.54	6.86	6.68	7.45	7.41	7.41	7.21

3	17.54	17.89	1.54	17.89	17.56	18.02	17.56	17.89
4	29.46	29.44	29.19	29.17	29.39	29.44	29.39	29.17

Chapter 8 Conclusion

The intended goal of this research is to use a non-traditional vibration absorber to achieve simultaneous vibration suppression and energy harvesting. For this purpose, an apparatus is designed in which a model B TMD is installed to an SDOF primary system with the absorber damper connected directly between the absorber mass and the base. The absorber system consists of two magnets as the absorber mass, an aluminum beam with adjustable length, and a pair of coils which, in interaction with two magnets, comprise an electromagnetic damper. By using such an electromagnetic device, vibration control can be achieved while energy is harvested by the load circuit. Chapter 2 has provided a detailed description of the proposed apparatus and the principle of the electromagnetic damper is discussed mathematically. It has been shown out that the higher the transduction factor and the lower the coil resistance, the higher the electrical damping of the damper. However, the damping coefficient of the damper is inversely proportional to the load resistance.

The dynamic model of the system has been defined using displacements of the primary mass and absorber mass relative to the base. The system's response under harmonic base excitation has been studied in Chapter 3. The displacement transmissibility ratio of the primary mass is used as the performance criterion. The optimum parameters, including the frequency tuning ratio β and the damping ratio ζ, have been derived using the classical "fixed-points" theory. To measure the performance of the electro-magnetic damper two indexes have been defined, namely the dissipated power ratio and the harvested power ratio. A computer simulation has been conducted. It has been found out that the dissipated power ratio reaches higher value at the resonance frequencies and anti-resonance frequency of the combined system with lower load resistance. When the inherent mechanical damping is taken into consideration, the ratio decreases quickly as the electrical damping decrease to the level close to the mechanical damping. The amount of the harvested power is proportional to the load resistance. This brings

up a trade-off situation as when the load resistance is increased, the electrical damping drops as well as the amount of the power dissipated by the damper. An experimental study has also been carried out. The effectiveness of the developed damper is tested. The identified damping ratios agree well with the analytical ones. Four sets of sweeping excitation tests have been conducted on the combined system. By tuning the absorber stiffness, the displacement transmissibility ratios at the fixed points can be made equal. By tuning the load resistance, the displacement transmissibility ratio curve can be made almost flat between the fixed points. The absorber's robust performance in vibration suppression is validated with the maximum achievable damping ratio of 17%. With regards to the energy harvesting, the experimental results also agree well with the simulation results. Among the four load resistances used in the experiment ($R_{load} = 20,\ 8,\ 2,\ 0.2\ \Omega$), the resistance of $8\ \Omega$ appears to offer a good trade-off between vibration suppression robustness and energy harvesting efficiency.

The transient responses of the system have been investigated in Chapter 4. The degree of stability of the system is defined as the first performance criterion and the optimum parameters are derived according to the Stability Maximization Criterion (SMC). This criterion describes the absorber's ability to suppress the transient response of the primary system. Another performance criterion is defined as the percentage of the harvested energy which evaluates the energy harvesting efficiency. It has been found that given a lower load resistance, higher absorber damping can be achieved which maximizes the degree of stability of the system but reduces the percentage of the harvested energy. By employing the genetic algorithm for a multi-objective optimization, the trade-off situation is addressed. The findings are validated by an experimental study. It is feasible to develop a model B TMD to achieve a balanced objective of vibration suppression and energy harvesting.

Chapter 5 has been dedicated to investigate the system subjected to random base excitation. The study is focused on the optimum parameters of the system to minimize the power dissipated by

the primary damping and maximize the power dissipated by the absorber damper as well as the power harvested by the load circuit. For the undamped primary system subjected to a white noise base excitation, the power dissipated by the absorber damping has a constant value which only varies with the mass ratio of the system. Local minimum point for the mean squared value to the relative velocity of the primary mass only exists when the mass ratio of the system is smaller than 0.15. When the primary system is damped, the minimization of the power dissipated by the primary damping is equivalent to the maximization of the power dissipated by the absorber damping. Local minimum/maximum point exists only when $\mu < 0.15$. For the damped primary system attached by the model B TMD, the trade-off between the dissipated power and harvested power is not significant with a low mass ratio, e.g. $\mu = 0.05$. An increase of the primary damping ratio does not affect the trade-off situation and only lowers the optimum tuning ratio value. An increase of the mass ratio, on the other hand, causes a more significant trade-off situation.

Chapter 6 has been dedicated to application of a model B TMD to a MDOF primary system. Using a 2DOF primary system as an example a similar investigation procedure for the SDOF primary system can be applied to study the combined MDOF system. Several results such as using the "fixed-points" theory to derive the optimum parameters, studying the energy dissipated by the absorber and harvesting efficiency under harmonic or random base excitation have been presented. The study in Chapter 6 is a preliminary one that reveals some interesting aspects that deserve more rigorous and thorough study for future.

Chapter 7 presents a course project conducted by the author. In this study, an integrated method called the SOBI-EWT method has been proposed for identification of closely-spaced modes commonly encountered in structures such as a multi-storey building attached with a TMD. The method first utilizes the second-order-blind-identification (SOBI) to extract the modal responses using the ambient vibration measurements. Since the SOBI alone does not guarantee the

separation of closely-spaced modes, the estimated mode-mixed response is further decomposed using the Empirical Wavelet Transform (EWT). The method demonstrates satisfactory performance based on the fact that the SOBI can achieve better separation with regards to higher order well-separated modes and provide valuable frequency-domain information for the EWT to build bandpass filter for the detection of the closely-spaced modes. Simulation results on a 6-storey model show that the proposed method is robust to a relatively higher level of noise, up to the order of 20%. The investigation is also extended to experimental results which indicate that the proposed method is capable of separating closely-spaced frequencies under a wide range of de-tuning situations.

References

Anh, N. D., & Nguyen, N. X. (2014). Design of non-traditional dynamic vibration absorber for damped linear structures. *Proceeding of the Institute of the Mechanical Engineering, 34*(1), 119-135.

Beeby, S. P., Torah, R. N., & Tudor, M. J. (2007). A micro electromagnetic generator for vibration energy harvesting. *Journal of Micromechanics and Microengineering, 17*, 1257-1265.

Beeby, S. P., Tudor, M. J., & White, N. M. (2006). Energy harvesting vibration sources for microsystems applications. *Measurement Science and Technology, 17*, R175-R195.

Belegundu, A., & Chandrupatla, T. (1999). *Optimization Concepts and Applications in Engineering*: Prentice-Hall, Inc.

Belouchrani, A., Abed-Meraim, K., Cardoso, J., & Moulines, E. (1997). A blind source separation technique using second-order statistics. *IEEE Transactions on Signal Processing, 45*(2), 434-443.

Brock, J. E. (1946). A note on the damped vibration absorber. *Journal of Applied Mechanics, 68*, A-284.

Cepnik, C., Radler, O., Rosenbaum, S., Strohla, T., & Wallrabe, U. (2011). Effective optimization of electromagnetic energy harvesters through direct computation of the electromagnetic coupling. *Sensors and Actuators A, 167*, 416-421.

Chtiba, M. O., Choura, S., Nayfeh, A. H., & El-Borigu, S. (2010). Vibration confinement and energy harvesting in flexible structuresusing collocated absorbers and piezoelectric devices. *Journal of Sound and Vibration, 329*, 261-276.

Chueng, Y. L., & Wong, W. O. (2009). Design of a non-traditional dynamic vibration absorber. *The Journal of the Acoustical Society of America, 126*(2), 564-567.

Chueng, Y. L., & Wong, W. O. (2011a). H-infinity optimization of a variant design of the dynamic vibration absorber: Revisited and new results. *Journal of Sound and Vibration, 330*, 3901-3912.

Chueng, Y. L., & Wong, W. O. (2011b). H_2 Optimization of a non-traditional dynamic vibration absorber for vibration control of structures under random force excitation. *Journal of Sound and Vibration, 330*(6), 1039-1044.

Chueng, Y. L., Wong, W. O., & Cheng, L. (2015). A subsystem approach for analysis of dynamic vibration absorbers suppressing broadband vibration. *Journal of Sound and Vibration, 342*, 75-89.

Deng, W., & Wang, Y. (2010). Non-contact magnetically coupled rectilinear-rotary oscillations to exploit low-frequency broadband energy harvesting with frequency up-conversion. *Applied Physics Letters, 109*, 133903.

Elvina, N. G., & Elvinb, A. A. (2011). An experimentally validated electromagnetic energy harvester. *Journal of Sound and Vibration, 30*(10), 2314-2324.

Feenstra, J., Granstrom, J., & Sodano, H. (2008). Energy harvesting through a backpack employing a mechanically amplified piezoelectric stack. *Mechanical Systems and Signal Processing, 22*, 721-734.

Gilles, J. (2013). Empirical Wavelet Transform. *IEEE Transactions on Signal Processing, 61*(16), 3999-4010.

Gonzalez-Buelga, A., Clare, L. R., Cammarano, A., Neild, S. A., Burrow, S. G., & Inman, D. J. (2014). An optimised tuned mass damper/harvester device', Structural Control Health Monitoring. *The Journal of the International Association for Structural Control and Monitoring, 21*(1), 1154-1169.

Gonzalez-Buelga, A., Clare, L. R., Neild, S. A., Burrow, S. G., & Inman, D. J. (2015b). An electromagnetic vibration absorber with harvesting and tuning abilities. *Structural Control and Health Monitoring, 22*(11), 1359-1372.

Gonzalez-Buelga, A., Clare, L. R., Neild, S. A., Jiang, J. Z., & Inman, D. J. (2015a). An electromagnetic inerter-based vibration suppression device. *Smart Materials and Structures, 24*, 055015.

Greco, R., Lucchini, A., & Marano, G. C. (2015). Robust design of tuned mass dampers installed on multi-degree-of-freedom structures subjected to seismic action. *Engineering Optimization, 47*(8), 1009-1030.

Harne, R. L. (2012). Theoretical investigations of energy harvesting efficiency from structural vibrations using piezoelectric and electromagnetic oscillators. *The Journal of the Acoustical Society of America, 132*(1), 162-172.

Harris, C. M., & Crede, C. E. (1976) *Handbook of Shock and Vibration (2nd Edition)*. New York: McGraw Hill Book Company.

Hartog, J. P. (1940). *Mechanical Vibration (2nd Edition)*. New York: McGraw-Hall.

Kremer, D., & Liu, K. (2014). A nonlinear energy sink with an energy harvester: Transient responses. *Journal of Sound and Vibration, 333*(4859-4880).

Liu, K., & Coppola, G. (2010). Optimum design of damped dynamic vibration absorber for damped primary systems. *Transaction of the Canadian Society for Mechiancal Engineering, 34*(1), 119-135.

Liu, K., & Liu, J. (2005). The damped dynamic vibration absorber: revisited and new results. *Journal of Sound and Vibration, 284*, 1181-1189.

Liu, Y., Chi-Chang, L., Jason, P., & Zuo, L. (2016). Exact H_2 optimal tuning and experimental verification of energy-harvesting series electromagnetic tuned-mass dampers. *Journal of Vibration and Acoustics, 138*(6), 1181-1189.

Lynch, J. P., & Loh, K. J. (2006). A summary review of wireless sensors and sensor networks for structural health monitoring. *The Shock and Vibration Digest, 38*(2), 91-128.

Mallat, S. (1999). *A wavelet tour of signal processing*: Academic press.

Mann, B. P., & Sims, N. D. (2010). On the performance and resonant frequency of electromagnetic induction energy harvesters. *Journal of Sound and Vibration, 329*, 1348-1361.

Masoumi, M., & Wang, Y. (2016). Repulsive magnetic levitation-based ocean wave energy harvester with variable resonance: Modelling, simulation and experiment. *Journal of Sound and Vibration, 381*, 192-205.

Musafere, F., Sadhu, A., & Liu, K. (2016). Towards damage detection using blind source separation integrated with time-varying auto-regressive modeling. *Smart Materials and Structures,, 25*(1), 15013-15031(15019).

Newland, D. E. (2012). *An introduction to random vibrations, spectral & wavelet analysis*: Courier Corporation.

Ng, T. H., & Liao, W. H. (2005). Sensitivity analysis and energy harvesting for a self-powered piezoelectric sensor. *Journal of Intelligent Material Systems and Structures, 16*, 785-797.

Nishimura, H., Yoshida, K., & Shimogo, T. (1989). Optimal dynamic vibration absorber for multi-degree-of-freedom systems (Theoretical consideration in the case of random input). *JSME international journal. Ser. 3, Vibration, control engineering, engineering for industry, 32*(3), 373-379.

Nishitani, O., & Matsihisa, H. (1997). Design optimization of passive gyroscopic damper (stability degree maximization). *International Journal of the Japan Society of Mechanical Engineers, Series C, Mechanical System, machine elements and manufacturing, 40*(4), 643-651.

Ozer, M. B., & Royston, T. J. (2004). Application of Sherman-Morrison matrix inversion formula to damped vibration absorbers attached to multi-degree of freedom systems. *Journal of Sound and Vibration, 283*, 1235-1249.

Ozer, M. B., & Royston, T. J. (2005). Extending Den Hartog's vibration absorber technique to multi-degree-of-freedom systems. *Journal of Vibration and Acoustics, 127*, 341-350.

Paradiso, J., & Starner, T. (2005). Energy scavenging for mobile and wireless electronics. *IEEE Pervasive Computing, 4*(1), 18-26.

Pennestri, E. (1998). An application of Chebyshev's min-max criterion to the optimum design of a damped dynamic vibration absorber. *Journal of Sound and Vibration, 217*, 757-765.

Pioldi, F., Ferrari, R., & Rizzi, E. (2016). Output-only modal dynamic identification of frames by a refined FDD algorithm at seismic input and high damping. *Mechanical Systems and Signal Processing, 68-69*, 265-291.

Rana, R., & Song, T. T. (1998). Parametric study and simplified design of tuned mass dampers. *Engineering Structures, 20*(3), 193-204.

Ren, M. Z. (2001). A variant design of the dynamic vibration absorber. *Journal of Sound and Vibration, 254*(4), 762-770.

Salvi, J., & Giaralis, A. (2016). Concept study of a novel energy harvesting-enabled tuned mass-damper-inerter (EH-TMDI) device for vibration control of harmonically-excited structures. *Journal of Physics: Conference Series, 744*(1), 012083.

Shahruz, S. M. (2008). Design of mechanical band-pass filters for energy scavenging: multi-degree-of-freedom models. *Journal of Vibration and Control, 14*(5), 753-768.

Shen, W., Zhu, S., & Xu, Y. (2012). An experimental study on self-powered vibration control and monitoring system using electromagnetic TMD and wireless sensors. *Sensors and Actuators A, 180*, 166-176.

Sneller, A. J., & Mann, B. P. (2010). On the nonlinear electromagnetic coupling between a coil and an oscillating magnet. *Journal of Physics D: Applied Physics, 43*(29), 295-305.

Sodano, H. A., Inman, D. J., & Park, G. (2005). Comparison of piezoelectric energy harvesting devices for recharging batteries. *Journal of Intelligent Material Systems and Structures, 16*(10), 799-807.

Sodano, H. A., Park, G., & Inman, D. J. (2004). Estimation of electric charge output for piezoelectric energy harvesting. *Strain, 40*(2), 49-58.

Stephen, N. G. (2006). On energy harvesting from ambient vibration. *Journal of Sound and Vibration, 293*, 409-425.

Tang, X., & Zuo, L. (2012a). Vibration energy harvesting from random force and motion excitations. *Smart Materials and Structures, 21*, 075025.

Tang, X., & Zuo, L. (2012b). Simultaneous energy harvesting and vibration control of structures with tuned mass dampers. *Journal of Intelligent Material Systems and Structures, 23*(18), 2117-2127.

Vakakis, A. F., & Paipetis, S. A. (1986). The effect of a viscously damped dynamic absorber on a linear multi-degree-of-freedom system. *Journal of Sound and Vibration, 105*(1), 49-60.

Wang, Y., & Inman, D. J. (2012). A survey of control strategies for simultaneous vibration suppression and energy harvesting via piezoceramics. *Journal of Intelligent Material Systems and Structures, 21*(18), 2021.

Wang, Y., & Inman, D. J. (2013). Simultaneous energy harvesting and gust alleviation for a multifunctional wing spar using reduced energy control via piezoceramics. *Journal of Composite Materials, 47*(1), 125-146.

Warburton, G. B. (1982). Optimum absorber parameters for various combination of response and excitation parameters. *Earthquake Engineering and Structural Dynamics, 10*, 381-401.

Wong, W. O., & Chueng, Y. L. (2008). Optimal design of a damped dynamic vibration absorber for vibration control of structure excited by ground motion. *Engineering Structures, 30*(1), 282-286.

Xiang, P., & Nishitani, A. (2014). Optimum design for more effectiveness tuned mass damper system and its application to base-isolated buildings. *Structural Control and Health Monitoring, 21*(1), 98-114.

Xiang, P., & Nishitani, A. (2015). Optimum design and application of non-traditional tuned mass damper toward seismic response control with experimental test varification. *Earthquake Engineering and Structural Dynamics, 44*, 2199-2220.

Yamaguchi, H. (1988). Damping of transient vibration by a dynamic absorber. *Transaction of the Japan Society of Mechiancal Engineer, Ser. C, 54*, 561-568.

Yoon, H. S. (2008). Active vibration confinement of flexible structures using piezoceramic patch actuators. *Journal of Intelligent Material Systems and Structures, 19*(2), 145-155.

Zilletti, M., Elliott, S. J., & Rustighi, E. (2012). Optimisation of dynamic vibration absorbers to minimise kinetic energy and maximise internal power dissipation. *Journal of Sound and Vibration, 331*, 4093-4100.

Zuo, L., & Cui, W. (2013). Dual-Functional Energy-Harvesting and vibration control: electromagnetic resonant shunt series tuned mass dampers. *Journal of Vibration and Acoustics, 135*, 051018-051011.

Zuo, L., & Nayfeh, S. A. (2002). *Design of passive mechanical systems via decentralized control techniques*. Paper presented at the 43rd AIAA/ASME/ASCE/AHS/ASC Structures, Structural Dynamics, and Materials Conference.

Zuo, L., & Nayfeh, S. A. (2004). Minimax optimization of multi-degree-of-freedom tuned mass damper. *Journal of Sound and Vibration, 272*, 893-908.

Appendix A Displacement Response Functions of a 2-DOF Structure Attached with a Non-traditional TMD

For a 2-DOF structure attached with a non-traditional absorber shown in Figure 6.1, the displacements of floors, each relative to the base, are found to be:

$$
\begin{aligned}
X_1 &= \sqrt{\frac{A_{X1}^2 + B_{X1}^2}{C_{X1}^2 + D_{X1}^2}} \\
A_{X1} &= \omega^2 Y[m_1 m_2 m_a \omega^4 - m_2 m_a k_2 \omega^2 - m_1 m_2 k_a \omega^2 - m_1 m_a k_a \omega^2 - m_1 m_a k_2 \omega^2 \\
&\quad + m_2 k_2 k_a + m_1 k_2 k_a + m_a k_2 k_a - m_1 c_2 c_a \omega^2 - m_2 c_2 c_a \omega^2 - m_a c_2 c_a \omega^2]; \\
B_{X1} &= \omega^2 Y[m_2 k_a c_a \omega + m_1 k_a c_2 \omega + m_1 k_a c_a \omega + m_1 k_2 c_a \omega + m_2 k_a c_2 \omega + m_a k_a c_2 \omega \\
&\quad + m_2 k_2 c_a \omega + m_a k_2 c_a \omega + m_a k_a c_a \omega - m_1 m_a c_2 \omega^3 - m_1 m_2 c_a \omega^3 - m_2 m_a c_2 \omega^3 - m_2 m_a c_a \omega^3]; \\
C_{X1} &= k_1 k_2 k_a - m_1 m_2 m_a \omega^6 + m_1 m_2 k_a \omega^4 + m_1 m_a k_2 \omega^4 + m_1 m_a k_a \omega^4 + m_2 m_a k_1 \omega^4 \\
&\quad + m_2 m_a k_2 \omega^4 + m_2 c_1 c_a \omega^4 + m_a c_2 c_a \omega^4 + m_a c_1 c_2 \omega^4 + m_2 c_2 c_a \omega^4 + m_1 c_2 c_a \omega^4 \\
&\quad - m_1 k_2 k_a \omega^2 - m_a k_1 k_2 \omega^2 - m_a k_1 k_a \omega^2 - m_2 k_1 k_a \omega^2 - m_a k_2 k_a \omega^2 - m_2 k_2 k_a \omega^2 \\
&\quad - k_a c_1 c_a \omega^2 - k_a c_1 c_2 \omega^2 - k_1 c_2 c_a \omega^2 - k_1 c_1 c_a \omega^2; \\
D_{X1} &= m_2 m_a c_1 \omega^5 + m_2 m_a c_2 \omega^5 + m_1 c_2 c_a \omega^5 + m_2 m_a c_a \omega^5 + m_1 m_2 c_a \omega^5 - m_1 k_a c_a \omega^3 \\
&\quad - m_a k_a c_1 \omega^3 - m_2 k_a c_2 \omega^3 - m_a k_a c_2 \omega^3 - m_2 k_a c_1 \omega^3 - m_2 k_a c_a \omega^3 - m_a k_1 c_2 \omega^3 \\
&\quad - m_a k_2 c_a \omega^3 - m_2 k_2 c_1 \omega^3 - m_2 k_1 c_a \omega^3 - m_1 k_2 c_a \omega^3 - m_1 k_a c_2 \omega^3 - m_2 k_2 c_a \omega^3 \\
&\quad - m_a k_a c_a \omega^3 - c_1 c_2 c_a \omega^3 + k_2 k_a c_1 \omega + k_1 k_a c_2 \omega + k_1 k_a c_a \omega + k_1 k_2 c_a \omega;
\end{aligned}
\tag{A.1}
$$

$$
\begin{aligned}
X_2 &= \sqrt{\frac{A_{X2}^2 + B_{X2}^2}{C_{X2}^2 + D_{X2}^2}} \\
A_{X2} &= \omega^2 Y[m_1 m_2 m_a \omega^4 - m_1 m_2 k_a \omega^2 - m_1 m_a k_2 \omega^2 - m_1 m_a k_a \omega^2 - m_2 m_a k_2 \omega^2 - m_2 m_a k_1 \omega^2 \\
&\quad - m_2 c_2 c_a \omega^2 - m_2 c_1 c_a \omega^2 - m_a c_2 c_a \omega^2 - m_1 c_2 c_a \omega^2 + m_1 k_2 k_a + m_2 k_2 k_a + m_a k_2 k_a \\
&\quad + m_a k_1 k_a + m_2 k_1 k_a]; \\
B_{X2} &= \omega^2 Y[-m_1 m_2 c_a \omega^3 - m_1 m_a c_2 \omega^3 - m_2 m_a c_2 \omega^3 - m_2 m_a c_1 \omega^3 - m_2 m_a c_a \omega^3 \\
&\quad + m_a k_a c_a \omega + m_a k_a c_2 \omega + m_2 k_a c_2 \omega + m_2 k_2 c_a \omega + m_2 k_a c_a \omega + m_1 k_2 c_a \omega \\
&\quad + m_a k_2 c_a \omega + m_a k_a c_1 \omega + m_1 k_a c_2 \omega + m_2 k_a c_1 \omega + m_1 k_a c_a \omega + m_2 k_1 c_a \omega]; \\
C_{X2} &= C_{X1}; \\
D_{X2} &= D_{X1};
\end{aligned}
\tag{A.2}
$$

Appendix B Parametric Study of the Electromagnetic Damper

This appendix briefly explains how to calculate the transduction factor of an electromagnetic damper based on the coil dimensions and a parametric study is conducted to reveal some interesting results and provide references for designing a more effective electromagnetic damper.

Recalling Chapter 2, in order to calculate the transduction factor (Θ) of the electromagnetic damper, a Finite Element Analysis software called FEMM is used to first analyze the magnetic field generated by the oscillating magnets. An axisymmetric model is built and Figure B.1 shows the results of the calculated magnetic flux density of the oscillating magnets with the same dimensions as in Table 2.1 but a higher grade at N52. The horizontal axis represents the radial direction *r* and the vertical axis the axial direction *z*. A detailed tutorial of how to perform FE analysis in FEMM is available online at http://www.femm.info/wiki/MagneticsTutorial.

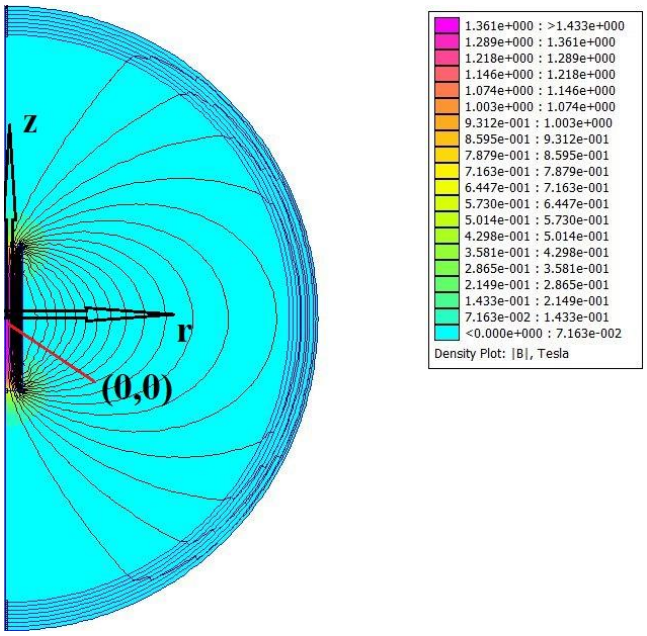

Figure B.1. Magnetic flux density of the oscillating magnets.

FEMM does not offer a direct access to the calculation results. To obtain the axial and radial magnetic flux density of the magnets, a ".lua" script is needed and an example is shown below in

Figure B.2. This script accesses the calculated radial magnetic flux density within the area of $6 \le r \le 60$ and $-70 \le z \le 70$ (mm) with an increment of 0.1 mm and save the data into the file named "Br.dat".

output.lua - Notepad

File Edit Format View Help

```
--bf_output.lua--
x1=6
x2=60
dx=0.1

y1=-70
y2=70
dy=0.1

ni = (x2-x1)/dx+2
nj = (y2-y1)/dy+2

handle=openfile("Br.dat","w")
write(handle,"VARIABLES = x y Bx \n")
write(handle,format("ZONE I=%d J=%d \n",ni,nj))

for j=0,nj-1,1 do
  for i=0,ni-1,1 do
  x=x1+i*dx
  y=y1+j*dy
  A,B1,B2=mo_getpointvalues(x,y)
  write(handle,x," ",y," ",B1,"\n")
 end
end

closefile(handle)
```

Figure B.2. An example of ".lua" script

For an electromagnetic damper, recall Eq. (2.5), the transduction factor of the coil depends on the coil dimensions,

$$\Theta(S) = -2\frac{l_{wire}}{A_{coil}}\int_{r_1}^{r_2}\int_{S-\frac{h_{coil}}{2}}^{S+\frac{h_{coil}}{2}} B_r(z,r)dzdr \tag{B.1}$$

To build a parametric model of the electromagnetic damper, three parameters are specified regarding the coil dimensions:

$$\Theta = \Theta(N_1, N_2, \Delta r) \tag{B.2}$$

N_1 is the number of layers of wire on the coil, N_2 is the number of turns of wire per layer and Δr is the radial gap between the magnet and the inner wall of the coil. Given a wire gauge, the diameter of the wire can be found and is defined as d_w. The parameters in Eq. (B.1) can be expressed as,

$$r_1 = r_{mag} + \Delta r \tag{B.3}$$

$$r_2 = r_1 + N_1 d_w \tag{B.4}$$

$$l_{wire} = N_2 \sum_{n=1}^{N_1} 2\pi (r_{mag} + \Delta r + \frac{2n-1}{2} d_w) \tag{B.5}$$

$$A_{coil} = N_1 N_2 d_w^2 \tag{B.6}$$

assuming that the wire is ideally wound as shown in Figure B.3.

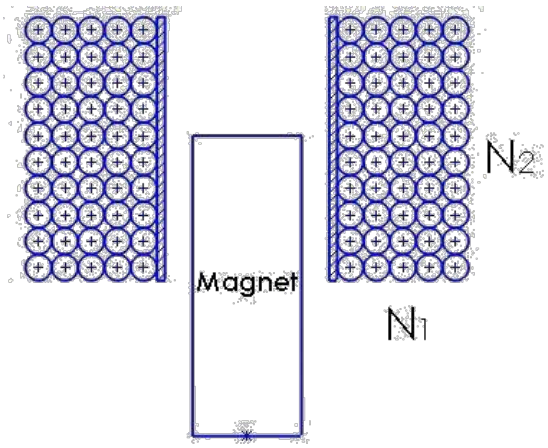

Figure B.3. Wire on the coil.

From the previous investigations it has been found out that there exists an optimum position of the coils which results in the maximum value of transduction factor Θ_{max}. This is usually achieved by aligning the center of the coils to the ends of the magnets. Recalling Eq. (2.10), the

coil resistance can be found after identifying the resistance per length value R_l for the coil wire from the table of American wire gauge sizes,

$$R_{coil} = R_l l_{wire} \tag{B.7}$$

and the highest electrical damping coefficient is achieved when the load resistance is zero,

$$(c_e)_{\max} = \frac{\Theta_{\max}^2}{2R_{coil}} \tag{B.8}$$

Numerical investigations are conducted to examine how the maximum transduction factor $\Theta_{\max}$ and maximum electrical damping coefficient of the damper $(c_e)_{\max}$ are affected by the aforementioned parameters: the number of layers of wire on the coil N_1, the number of turns of wire per layer N_2 and the radial gap between the magnet and the inner wall of the coil Δr. The parameters of the magnets are shown in Table 2.1 and the magnets have the grade of N52. The coil is wound from the gauge #16 wire with the properties of $d_w = 1.291\,\text{mm}$ and $R_l = 13.17\ \text{m}\Omega/\text{m}$.

The radial gap is first set to be 1.25 mm, i. e. $\Delta r = 1.25\,\text{mm}$. Figure B.4 shows how the maximum transduction factor $\Theta_{\max}$ changes when N_1 varies from 1 to 20 and N_2 varies from 10 to 50. To better distinguish the curves, the color of the curves are adjusted such that as the layers of the wire increases, the color changes from dark blue to light green. From Figure B.4 it can be seen that $\Theta_{\max}$ increases with the increase of N_1 and N_2. This is easy to understand as it is indicated in Eq. (B.1) that the bigger the cross sectional area of the coil, the higher transduction factor after the double integration on the cross sectional area.

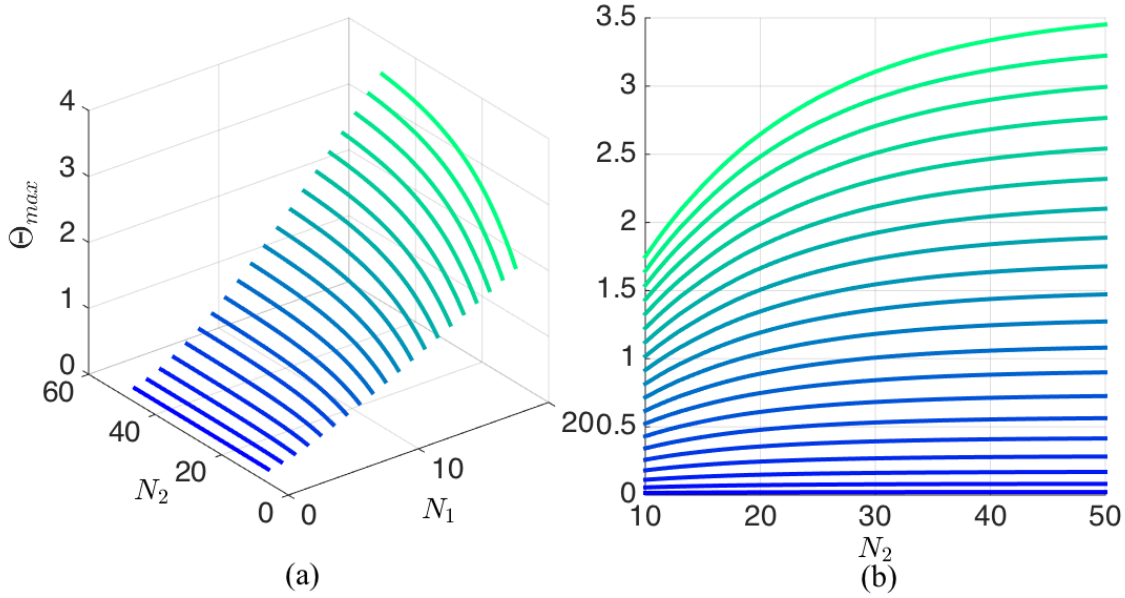

Figure B.4. Maximum transduction factor when Δr=1.25 mm: (a) 3D view; (b) 2D view.

However, a bigger cross sectional area of the coil also means longer wire length and higher coil resistance. From Eq. (B.8) it can be seen that the electrical damping coefficient does not simply increase with the increase of the transduction factor. It also decreases with the increase of coil resistance. Figure B.5 shows how the maximum electrical damping coefficient changes with N_1 and N_2. $(c_e)_{max}$ increases with more layer of wire (N_1). However, an increasing number of turns of wire per layer (N_2) does not necessarily brings up $(c_e)_{max}$. The optimum N_2 value is within 15 to 20 when $1 \le N_1 \le 20$ and is increasing with a higher N_1 value.

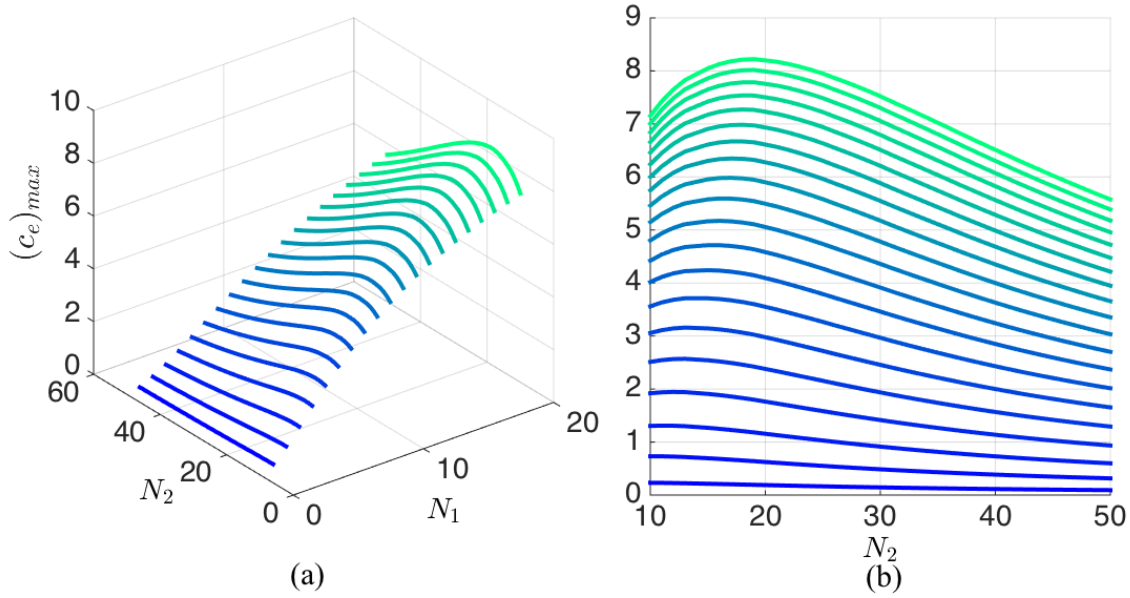

Figure B.5. Maximum electrical damping coefficient when Δr=1.25 mm: (a) 3D view; (b) 2D view.

To investigate the effect of the radial gap Δr has on the maximum transduction factor and electrical damping coefficient, another set of simulation is conducted with four different Δr value, 0.75, 1.00, 1.25, 1.50 mm. For each Δr value, Θ_{max} and $(c_e)_{max}$ are calculated for $1 \le N_1 \le 20$ and $10 \le N_2 \le 50$ and the results are plotted as a surface shown in Figure B.6 (a) and Figure B.7 (a). For better clarification, three sets of curves are extracted from Figure B.6 (a) which corresponds to N_1 =4, 12 and 20, respectively. As shown in Figure B.6 (b), the curves have the same color when they are extracted from the same surface which presents a specific Δr value. The curve color changes from blue to green as Δr increases. The maximum transduction factor decreases when one expands the radial gap between the magnets and the coil. This is as expected because the farther the coil is to the magnets, the lower the radial magnetic flux density among the coil region and according to Eq. (B.1), the lower the transduction factor.

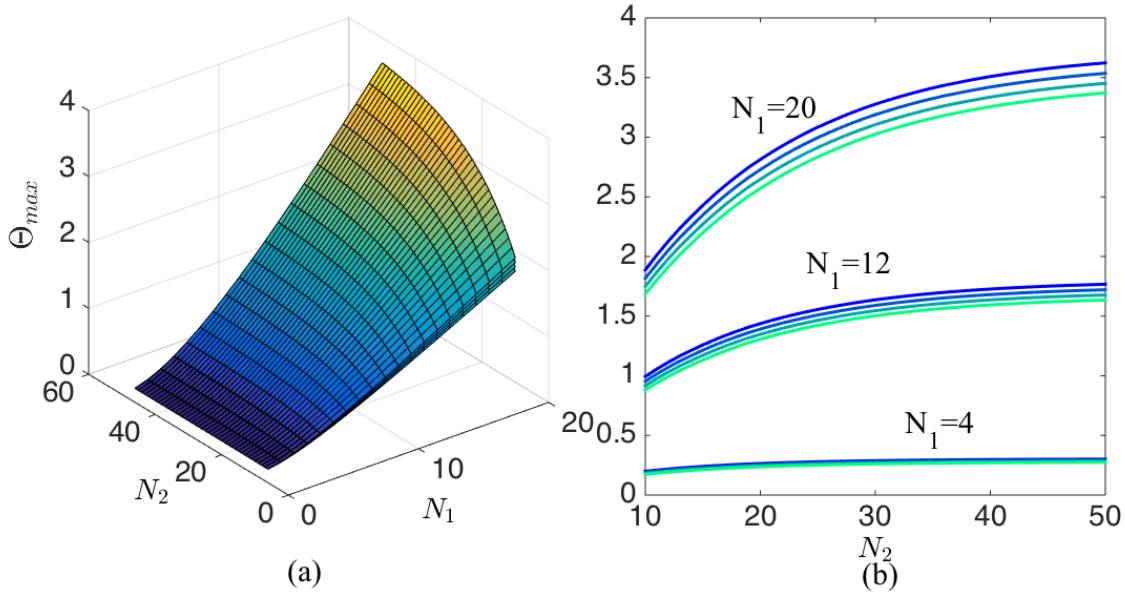

Figure B.6. Maximum transduction factor under different radial gaps.

A similar feature is observed in Figure B.7 (b) for the maximum electrical damping coefficient. The optimum number of turns of wire per layer exists regardless of the radial gap and the bigger the gap, the smaller the electrical damping the damper can achieve.

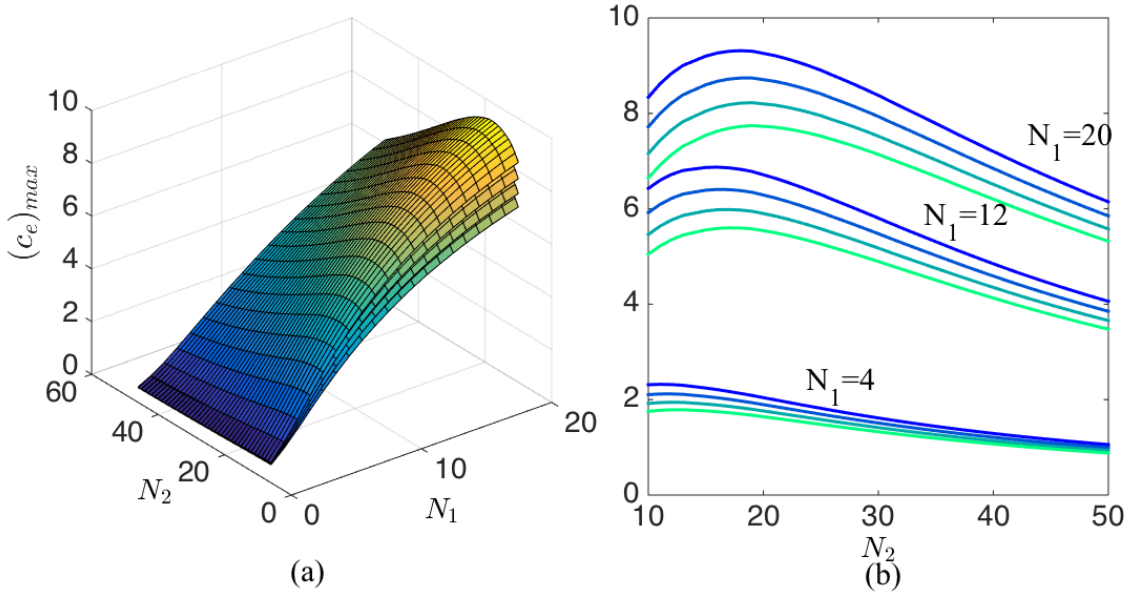

Figure B.7. Maximum electrical damping coefficient under different radial gaps.

In conclusion, after performing a parametric study, the effects of the three specified parameters on the performance of the damper are found. The maximum transduction factor the coil can achieve increases with the increase of N_1 and N_2, and decreases with the increase of Δr. Increasing N_1 and decreasing Δr also help in raising the maximum electrical damping coefficient of the damper. However, there exists an optimum N_2 to optimize c_e and it is within 15 to 20 when there is less than 20 layers of wire on the coil.